THE ELECTROCHEMISTY OF SURFACE MODIFIED <10 NM METAL OXIDE NANOPARTICLES

Joseph J.P. Roberts

A dissertation submitted to the faculty of the University of North Carolina at Chapel Hill in partial fulfillment of the requirements for the degree of Doctor of Philosophy in the Department of Chemistry (Analytical Chemistry)

Chapel Hill
2014

Approved by:

Royce W. Murray

James W. Jorgenson

Robert M. Wightman

Wei You

Alexander J. M. Miller

ABSTRACT

Joseph J.P. Roberts: The Electrochemisty of Surface Modified <10 nm Metal Oxide Nanoparticles
(Under the direction of Royce W. Murray)

Chapter One provides a general introduction of the research on metal oxide nanoparticles (MO_x), highlighting their synthesis, surface modification, and functionalization. Emphasis is given to the different synthetic route for producing small (<10 nm) MO_x nanoparticles with narrow size distributions. Different methods for modifying their surface with small organic molecules are discussed with focus given to silanes and phosphates. Furthermore, functionalizing surface modified nanoparticles for specific functions is addressed, with markers for analytically relevant nanoscale quantification being the primary focus.

Chapter Two describes in detail the thermal degradation synthesis used for the generation of small MO_x nanoparticles. It demonstrates the versatile of the synthesis by successfully synthesizing ZrO_2 and IrO_2 nanoparticles. Preliminary work involving the formation of Bi_2S_3, Bi_2O_3, and RuO_2 nanomaterials is also addressed. The solvothermal synthesis of indium tin oxide (ITO) is also shown for comparison to ITO produced by thermal degradation.

Chapter Three details the surface modification of ITO nanoparticles and subsequent electrochemical tagging with a ferrocene moiety. ITO nanoparticles were synthesized via thermal degradation. These nanoparticles underwent a ligand exchange with a covalently binding mondentate silane terminated with a primary amine. Acyl chloride coupling between the amine and chlorocarbonylferrocene provided an electrochemical tag to quantify the level of surface

modification. Electrochemisty of the quasi-diffusing nanoparticles was evaluated via cyclic voltammetry (CV), chronoamperometry (CA), and mircodisk electrode (μE) experiments.

Chapter Four investigates spectroscopic tagging of ITO and ZrO_2 nanoparticles as well as electrochemical tagging of ZrO_2 and IrO_2 nanoparticles. An unbound azo-dye was synthesized and attempts were made to attach the dye to the surface of ITO nanoparticles. Imine couple between a spectroscopic tag and ZrO_2 nanoparticles was also explored, but resulted in very low surface coverages. ZrO_2 nanoparticles were also ferrocene tagged using previously discussed siloxane chemistry as well as a new route using click chemistry with an azo-phosphate ligand. A similar approach was taken with hydrolytically synthesized IrO_2 and is included for comparison.

Chapter Five studies the multivalent electrochemistry of 4 nm magnetite nanoparticles. These nanoparticles are synthesized via thermal degradation and capped with citric acid to make them water soluble. pH dependent electrochemistry was discovered and characterized using cyclic voltammetry, chronoamperometry, and rotating disk electrode experiments. Two separate electrochemical species are present and undergo two irreversible, but separate electrochemical reactions; Fe(II) → Fe (III) and Fe(III) → Fe(II).

To my family for always loving, supporting, and believing in me. And to Megan, for continuing to love me even while I was 500 miles away. This work is for us.

ACKNOWLEDGEMENTS

What a ride it has been! This dissertation would not be possible without the support and contributions of many people in my life. First, I would like to thank Dr. Royce W. Murray for all of his support during my graduate experience. He's been an excellent mentor and I am very thankful for all the opportunities he has given me to share my research, mentor undergraduates, and grow as an individual. He will likely forget more about chemistry than I will ever know. Thank you for putting up with my nonsense for 5 years. I hope to do you proud as teacher.

I would also like to extend my thanks to the members of the Murray Lab who shared my time here at UNC. The 5th years who helped acclimate me to the lab, Joe Parker, Christina Zinna-Fields, Chris Beasley, and Josh Weaver, you have my everlasting thanks for your continued support over the years. Our Post-Docs, Rajesh Sardar, Kwok Fan Chow, and Lloyd Horne, thank you for the wealth of information you provided to a young scientist and for the conversations about science that helped motivate me to do some of my best work. Natalie Bjorge, thanks for being you and for helping me have some much needed fun during the Boston ACS conference. Alessa Gambardella, thank you for my inability to pronounce Alyssa correctly now. Truthfully, there are too many things to thank you for, even if we did butt heads from time to time. To be succinct, thanks for helping me become a better scientist and lab mate. Tessa Carducci, thank you for our silly conversations regarding certain muscle-bound graduate student's abs. Kidding aside, thanks for being a good lab mate and teaching us about gold nanoparticles. And finally, thank you Katie Michaux for being my friend. This lab could be a crazy place, and you've stuck

with me through it all. I really appreciate our coffee walks, our cupcake dates, and our morning talks. May your stubbornness always refute my results and may your Excel never crash.

I also want to thank all of the undergraduates and interns who have given me the pleasure of working with them during this last 5 years. Kimmy Vuong, Ahnthu Vuong, John Westgard, Chris Wilhelmson, and Laura Cooper, you guys proved that teaching is really what I want to do. You've been the most rewarding part of my graduate experience. Good luck in everything you do.

Much of the work presented here couldn't have been done without the wonderful support staff here at UNC. Debbie Norton, thank you for being such a great asset to the lab and helping out with all the ridiculous things we needed. Also, thank you for not throwing me out a window for all the times I messed up the PCard. Amar Kumbhar, thank you for all your sage advice about grad school, all time we spent looking at tiny organic covered nanoparticles, and for taking me to the Spice & Curry buffet where I was convinced I was going to die. Thank you Carrie Donely for great conversation in the XPS room and for running all of the questionable samples I brought you. And finally, Reggie down at Fisher for just shooting the breeze with me when I needed a little break from science.

Next, I need to thank my friends and family for all their support. To my family, you've done so much for me over the years even a 170 page document of thank yous wouldn't be enough. I love you all. To my graduate friends, well, there are too many of you to individually name. You guys have made UNC a great place to work and even convinced me to go out the bars once or twice. However, I have to give a special thanks to Drew and Ellen Perkowski for being such great friends and always taking such good care of me. May our paths forever cross. And finally, a great many thanks to Derek DeMarco for every well placed League of Legends

distraction, every silly conversation about knowing what it's like to be the Batman, and for being the best pseudo-sibling I could ever have.

And finally, I have to thank Megan Kathleen Showell for being my stability during the emotional rollercoaster called grad school. You were the most important discovery I made at UNC and wouldn't trade you for an infinite number of PhDs. I thank the fates every night that you chose me, and continue to choose me despite the distance that separated us. I love you more than words could ever describe.

TABLE OF CONTENTS

TABLE OF CONTENTS ix

LIST OF TABLES xiv

LIST OF FIGURES xv

LIST OF SCHEMES xviii

LIST OF ABBERVIATIONS AND SYMBOLS xix

CHAPTER 1 - AN INTRODUCTION TO METAL OXIDE NANOPARTICLES AND METHODS TO MODIFY THEIR SURFACE 1

1.1 Methods of Metal Oxide Nanoparticle Synthesis 4

1.2 Surface Modification of Metal Oxide Nanoparticles 5

1.3 Functionalization of Metal Oxide Nanoparticles 8

CHAPTER 2 – SYNTHESIS OF METAL OXIDE NANOPARTICLES BY THERMAL DEGRADATION AND SOLVOTHERMAL ROUTES 16

2.1 Introduction 16

2.1.1 Metal Oxide Nanoparticles via Thermal Degradation Synthesis 17

2.1.2 Metal Oxide Nanoparticles via Solvothermal Synthesis 19

2.2 Experimental 20

2.2.1 Chemicals and Materials 20

2.2.2 Instrumentation 21

2.2.3 Standard Thermal Degradation Synthesis of Metal Oxide Nanoparticles 21

2.2.4 Hot Injection Thermal Degradation Synthesis of Metal Oxide Nanoparticles 22

2.2.5 Solvothermal Synthesis of ITO Nanoparticles 23

2.2.6 Citrate Capped Nanoparticles. 23

2.2.7 Estimations of Nanoparticle Mass and Composition 24

2.3 Results and Discussion 24

2.3.1 Characterization of ZrO_2 Nanoparticles Prepared by Thermal Degradation Synthesis 24

2.3.2 Characterization of IrO_2 Nanoparticles Prepared by Thermal Degradation Synthesis 29

2.3.3 Characterization of Bi_2S_3 and Bi_2O_3 Nanomaterials Prepared by Thermal Degradation Synthesis 29

2.3.4 Characterization of RuO_2 Nanoparticles Prepared by Thermal Degradation Synthesis 40

2.3.5 Characterization of ITO Nanoparticles Prepared by Solvothermal Synthesis 40

2.4 Conclusions 44

2.5 Acknowledgments 44

2.6 References 47

CHAPTER 3 – SYNTHESIS AND ELECTROCHEMISTRY OF 6 NM FERROCENATED INDIUM TIN OXIDE NANOPARTICLES 49

3.1 Introduction 49

3.2 Experimental 50

3.2.1 Chemicals and Materials 50

3.2.2 Instrumentation and Electrochemical Details 52

3.2.3 Synthesis of 6 nm Indium Tin Oxide Nanoparticles 53

3.2.4 Silane-Capped ITO Nanoparticles. 53

3.2.5 Synthesis of Ferrocenoyl Chloride and of Ferrocene-Functionalized ITO Nanoparticles. 54

3.3 Results and Discussion 54

3.3.1 ITO Synthesis. 54

3.3.2 Replacement of Surfactants with Silane Ligands and Ferrocenation. 56

3.3.3 Voltammetry of Ferrocenated ITO Nanoparticles. 62

3.4 Acknowledgment. 69

3.5 References 71

CHAPTER 4 – SPECTROSCOPIC AND ELECTROCHEMICAL MODIFICATION OF SMALL (<10 NM) METAL OXIDE NANOPARTICLES 73

4.1 Introduction 73

4.1.1 Surface Modification by Siloxane Chemisty 74

4.1.2 Surface Modification by Phosphate Chemistry 75

4.1.3 Analytical Methods for Quantification of Surface Modification 76

4.2 Experimental 77

4.2.1 Chemicals and Materials 77

4.2.2 Instrumentation and Electrochemical Details 78

4.2.3 Silane-Capped ITO and ZrO Nanoparticles. 79

4.2.4 Synthesis of N,N-Dimethylaniline Dye 79

4.2.5 Amine Quantification via Imine Coupling with ZrO_2 Nanoparticles 80

4.2.6 Synthesis of Ferrocenoyl Chloride and of Ferrocene-Functionalized ZrO Nanoparticles. 80

4.2.7 Synthesis of Ferrocene Functionalized ZrO_2 and IrO_2 via Click Chemisty 83

4.3 Results and Discussion 85

4.3.1 Spectroscopic Surface Quantification by Dye-Modified ITO Nanoparticles 85

4.3.2 Spectroscopic Surface Quantification by Imine Coupled ZrO_2 Nanoparticles 87

4.3.3 Surface Modification of ZrO_2 with Silane Bound Ferrocene. 88

4.3.4 Voltammetry of Ferrocenated Silane-Capped ZrO_2 Nanoparticles (FcZrO) 91

4.3.5 Click Ferrocenation of ZrO_2 and IrO_2 Nanoparticles..... 101

4.4 Acknowledgments 110

4.5 References..... 115

CHAPTER 5 – ELECTROCHEMICAL EVALUATION OF <10 NM CITRATE CAPPED MAGNETITE NANOPARTICLES 118

5.1 Introduction..... 118

5.2 Experimental..... 120

5.2.1 Chemicals and Materials..... 120

5.2.2 Instrumentation and Electrochemical Details 121

5.2.3 Synthesis of 4 nm Magnetite Nanoparticles. 122

5.2.4 Citrate Capped Magnetite Nanoparticles. 123

5.3 Results and Discussion 123

5.3.1 Fe_3O_4 Nanoparticle Synthesis and Characterization. 123

5.3.2 Surfactant Replacement. 124

5.3.3 Electrochemistry of Solutions of Citrate-Capped Magnetite Nanoparticles. 131

5.3.4 Effects of Magnetic Field on Magnetite Electrochemisty. 146

5.4 Acknowledgments 146

5.5 References 151

LIST OF TABLES

Table 2.1 – Atomic values for ZrO_2 28

Table 2.2 – Atomic values for IrO_2 34

Table 2.3 – Atomic Values of Bi_2O_3 43

Table 4.1 – Spectroscopic Quantification of silane ZrO_2 90

Table 5.1 – Molar absorptivities of magnetite and citrate-magnetite 128

Table 5.2 – Electrochemically determined diffusion coefficients of cit-Fe_3O_4 145

Table 5.3 – Exchange currents and rate constants for cit-Fe_3O_4 148

LIST OF FIGURES

Figure 2.1 – TEM of citrate-ZrO_2 nanoparticles 26

Figure 2.2 – XPS of ZrO_2 and citrate-ZrO_2 nanoparticles 27

Figure 2.3 – UV/Vis of ZrO_2 nanoparticles 30

Figure 2.4 – TEM of IrO_2 nanoparticles 31

Figure 2.5 – XPS of IrO_2 nanoparticles 32

Figure 2.6 – EDX of IrO_2 nanoparticles 33

Figure 2.7 – TEM of Bi_2S_3 nanomaterials 36

Figure 2.8 – EDX of Bi_2S_3 nanoparticles 37

Figure 2.9 – UV/Vis of Bi_2S_3 nanoparticles 38

Figure 2.10 – TEM of Bi_2O_3 nanoparticles 39

Figure 2.11 – XPS of Bi_2O_3 and citrate-Bi_2O_3 nanoparticles 41

Figure 2.12 – EDX of Bi_2O_3 nanoparticles 42

Figure 2.13 – TEM of solvothermal ITO nanoparticles 46

Figure 3.1 – TEM of ITO nanoparticles 55

Figure 3.2 – XPS of ITO nanoparticles 57

Figure 3.3 – Cu^{2+} titration of ferrocenated ITO nanoparticles in CH_3CN 59

Figure 3.4 – XPS of ferrocenated ITO nanoparticles 60

Figure 3.5 – EDX of ferrocenated ITO nanoparticles 61

Figure 3.6 – Cyclic voltammetry of ferrocenated ITO nanoparticles in CH_3CN 64

Figure 3.7 – Randles-Sevcik plot for ferrocenated ITO nanoparticles in CH_3CN 65

Figure 3.8 – Microdisk electrode voltammetry of ferrocenated ITO nanoparticles in CH_3CN ... 66

Figure 3.9 – Cottrell plot of ferrocenated ITO in CH_3CN 67

Figure 3.10 – CVs of ferrocenated ITO nanoparticles after FcCOOH additions 70

Figure 4.1 – UV/Vis of N,N-dimethylaniline dye 86

Figure 4.2 – UV/Vis of 4-NBA..... 89

Figure 4.3 – TEM of silanized and ferrocenated ZrO_2 nanoparticles 92

Figure 4.4 – XPS of silanized ZrO_2 nanoparticles..... 93

Figure 4.5 – XPS of ferrocenated ZrO_2 nanoparticles 94

Figure 4.6 – EDX of ferrocenated ZrO_2 nanoparticles 95

Figure 4.7 – Cyclic voltammetry of ferrocenated ZrO_2 nanoparticles in DCM 98

Figure 4.8 – Randles-Sevcik plot of ferrocenated ZrO_2 nanoparticles in DCM..... 99

Figure 4.9 – i_{PEAK} scan rate dependence of ferrocenated ZrO_2 nanoparticles in DCM 100

Figure 4.10 – Microdisk electrode voltammetry of ZrO_2 nanoparticles in DCM..... 103

Figure 4.11 – Cottrell plot of ferrocenated ZrO_2 nanoparticles in DCM 104

Figure 4.12 – TEM of click-ZrO_2 nanoparticles..... 106

Figure 4. 13 – XPS of click-ZrO_2 nanoparticles..... 107

Figure 4.14 – XPS of azo-IrO_2 nanoparticles..... 108

Figure 4.15 – XPS of click-IrO_2 nanoparticles 109

Figure 4.16 – Cyclic voltammetry of click-ZrO_2 nanoparticles in CH_3CN..... 111

Figure 4.17 – Cyclic voltammetry of click-IrO_2 nanoparticles in DMSO..... 112

Figure 4.18 – Randles-Sevcik of click-ZrO_2 nanoparticles in CH_3CN..... 113

Figure 4.19 – Cottrell plot of click-ZrO_2 nanoparticles in CH_3CN 114

Figure 5.1 – TEM of magnetite nanoparticles 125

Figure 5.2 – XRD of magnetite nanoparticles 126

Figure 5.3 – UV/Vis of magnetite and cit-Fe_3O_4 nanoparticles..... 127

Figure 5.4 – Emission spectra of magnetite nanoparticles 129

Figure 5.5 – XPS of magnetite nanoparticles 130

Figure 5.6 – TEM of cit-Fe_3O_4 nanoparticles 132

Figure 5.7 – XPS of cit-Fe_3O_4 nanoparticles 133

Figure 5.8 – Cyclic Voltammetry of cit-Fe_3O_4 in citrate buffer 134

Figure 5.9 – Comparison between Pt background and cit-Fe_3O_4 in citrate buffer 135

Figure 5.10 – Comparison between Au background and cit-Fe_3O_4 in citrate buffer 136

Figure 5.11 – pH depedence of cit-Fe_3O_4 electrochemistry in citrate buffer 138

Figure 5.12 – Cyclic voltammetry of Fe(III) citrate in citrate buffer 139

Figure 5.13 – Randles-Sevcik plot of cit-Fe_3O_4 in citrate buffer 140

Figure 5.14 – RDE of cit-Fe_3O_4 in citrate buffer 142

Figure 5.15 – Levich plot of cit-Fe_3O_4 in citrate buffer 143

Figure 5.16 – Cottrell plot of cit-Fe_3O_4 in citrate buffer 144

Figure 5.17 – Tafel plot of cit-Fe_3O_4 in citrate buffer 147

Figure 5.18 – Magnetic electrochemisty experimental setup 149

Figure 5.19 – Magnetic cyclic voltammetry of cit-Fe_3O_4 in citrate buffer 150

LIST OF SCHEMES

Scheme 1.1 – Cartoon of presented nanoparticle modifications..... 2

Scheme 3.1 – Cartoon of presented ITO nanoparticles ferrocenation..... 51

Scheme 4.1 – Synthetic route for azo-dye modified ITO..... 81

Scheme 4.2 – Synthetic route for click modified MO_x nanoparticles..... 82

LIST OF ABBERVIATIONS AND SYMBOLS

4NBA	4-nitrobenzaldehyde
A	ampere
ac	acetate
acac	acetylacetonate
Ag	silver
Ag/AgCl	silver-silver chloride
Ar	argon
Au	gold
aux	auxiliary electrode
BE	bulk electrolysis
Bi	Bismuth
Bi_2O_3	bismuth oxide
Bi_2S_3	bismuth sulfide
Bu_4NClO_4	tetrabutylammonium perchlorate
C	coulombs
°C	degree Celsius
CA	chronoamperometry
ca	circa
CF	chloroform
cm	centimeter
CV	cyclic voltammetry

D	diffusion constant
DCM	dichloromethane
dia	diameter
DMSO	dimethyl sulfoxide
E	potential
EDX	energy dispersive x-ray spectroscopy
ε	molar absorptivity
E_{PEAK}	peak potential
ΔE_{PEAK}	peak potential separation
EtOH	ethanol
F	Faraday's constant
Fc	ferrocene
g	gram
h	hour
i	current
i_{LIM}	limiting current
In	indium
Ir	iridium
IrO_2	iridium oxide
ITO	indium tin oxide
m	minute
M	molar
µE	microdisk electrode

MeCN	acetonitrile
MeOH	methanol
mg	milligram
mL	milliliter
µL	microliter
mm	millimeter
µm	micrometer
mM	millimolar
mol	moles
mV	millivolt
MO_x	metal oxide
n	number of electrons
N	number of moles
NaOH	sodium hydroxide
nm	nanometer
NP	nanoparticle
Pt	platinum
RDE	rotating disk electrode
ref	reference electrode
RuO_2	ruthenium oxide
s	second
S	sulfur
Sn	tin

T	temperature
TCOs	transparent conducting oxides
TD	thermal degradation synthesis
TEM	transmission electron microscope
UV-Vis	ultraviolet-visible
V	volt
vs	versus
WE	working electrode
XPS	x-ray photoelectric spectroscopy
XRD	x-ray diffraction
Zr	zirconium
ZrO_2	zirconium oxide
+	positive
-	negative

CHAPTER 1 - AN INTRODUCTION TO METAL OXIDE NANOPARTICLES AND METHODS TO MODIFY THEIR SURFACE

The field of nanotechnology has experienced an explosion of growth in recent years. This is largely due to the number of interesting properties that nanomaterials have over their bulk counterparts. As you shrink a material down to the nanoscale, you typically see changes based on quantum confinement. CdSe nanoparticles, often referred to as quantum dots, can emit different wavelengths of light based on the diameter of the nanoparticle[1]. Changing the diameter between 2 to 10 nm covers the entire visible range. Nanomaterials also exhibit increased reactivity as they provide large surface-to-volume ratios. The number of potential applications is large, especially since careful synthetic control opens an avenue to "tune" a nanomaterial for a wide range of applications. Polymeric nanomaterials, for instance, might be able to prevent biofouling of implantable sensors by gradually releasing NO during the lifetime of the device[2]. Gold nanoparticles, a favored topic in the nanocommunity, can be synthesized in specific "magic" structures, such as Au_{25}. Not only do these small nanoparticles (~1.2 nm) show quantized energy levels during electrochemical analysis, but they also allow a gold's surface plasmon to be "tuned" based on nanoparticle size[3]. Many metal nanoparticles show increased catalytic efficiency due to their high surface-to-volume ratio. Small (~1 nm) Ru/Pd nanoparticles have been shown to perform hydrogenations with high yields and excellent enantioselectivity[4]. The list goes on, with the largest number of applications in medical[5-7], energy[8-9], and consumer uses. With so many materials available it would be impractical for one research facility to create and

Scheme 1.1 – Outline of MO_x suface modifications and functionalizations presented in this work

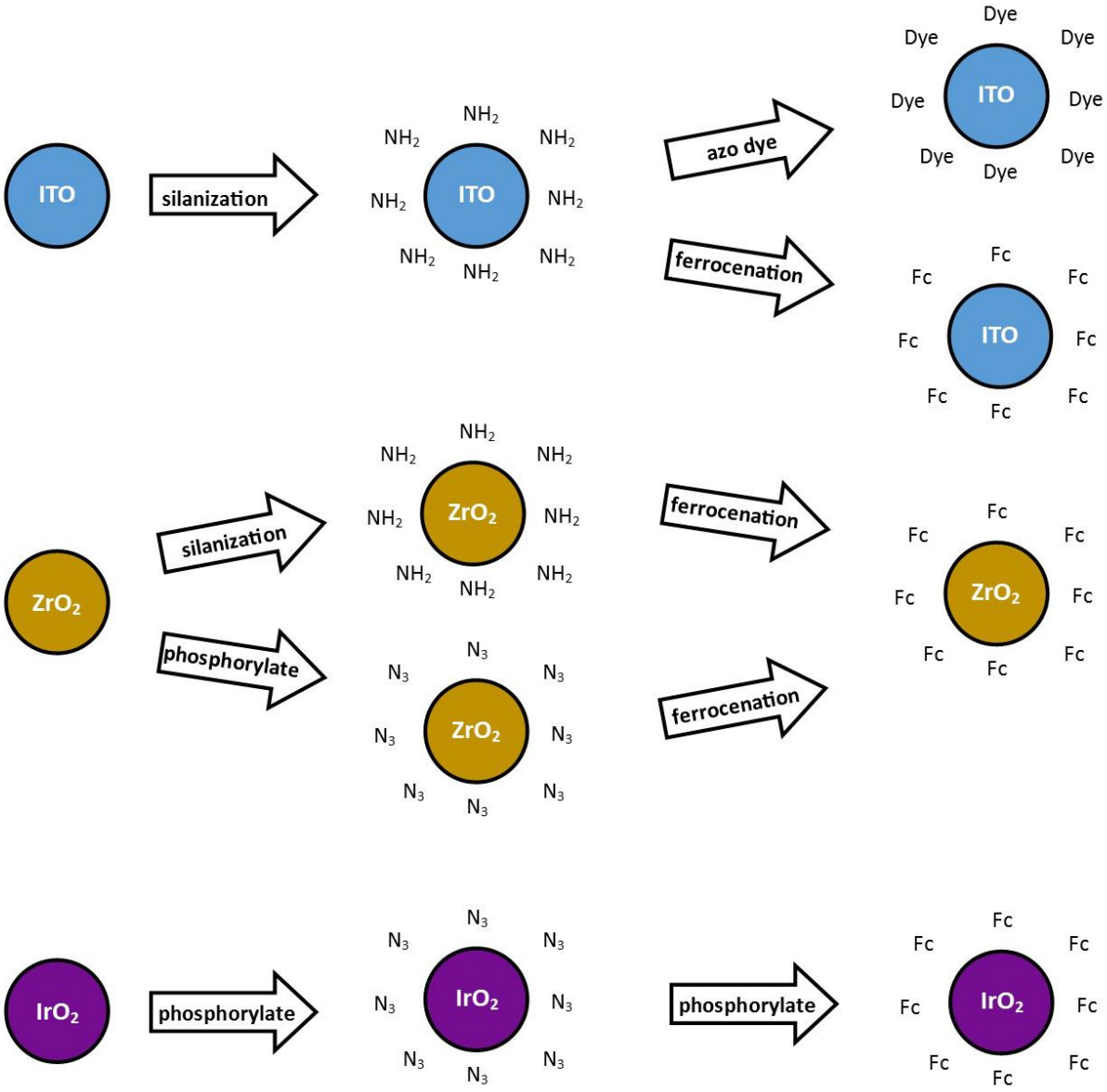

characterize them all. Instead, this work focuses on nanomaterials made from metal oxides and aims to control their formation during synthesis and change their properties by modifying their surfaces.

Metal oxide (MOx) nanoparticles are large portion of nanomaterial research. With an already staggering number of interesting MO_x bulk materials, investigating their nanoscale counterparts is a large undertaking. So many materials necessitates a need to evaluate and categorize them. This work chooses to organize them based on their most valued properties, and will focus on catalytic, magnetic, and transparent conducting MO_x nanoparticles. As discussed above, catalysis is a very important field in nanomaterial research. Several MO_x NPs have shown catalytic properties for a variety of organic reactions[10]. Other materials, like iridium oxide, show promise in energy applications by reducing the overpotential of water oxidation to allow its splitting by solar energy[11]. Magnetic nanoparticles, like iron oxide and its derivatives, are primarily examined for their biological applications[6]. These nanoparticles show relatively low cell toxicity[12-13] and can be manipulated *in vivo* by a powerful magnetic field providing routes for targeted drug delivery systems in cancer treatment[14], more robust MRI contrast reagents[15-16], and immunotherapy treatments by localizing hyperthermia[15]. Another category includes transparent conductive oxides (TCOs), like indium tin oxide and TiO_2. These materials have good conductivity and high optical transparency in the visible region. Traditionally TCOs have seen use in spectroelectrochemistry[17], but are now frequently used in commercial display devices like flat screen TVs and monitors. They also show great promise as modifiable conductive windows in solar cell designs[18]. Much of the work presented in this thesis deals with the characterization and modification of TCO and magnetic materials. A small section on catalytic nanoparticles is also included.

1.1 Methods of Metal Oxide Nanoparticle Synthesis

There are many synthetic routes for metal oxide nanomaterials, generally stemming from the desire to specifically tune their properties. A frequently used synthesis is a co-precipitation method which involves metal salts (often chloride salts) in the presence of strong acid or base[19]. The size, type, and properties of the nanomaterial generated are based on the acid/base used, pH, and the concentration of the metal salts[20-21]. Generally, the reaction yields water soluble materials but can suffer from poor monodispersity and crystallinity. Co-precipitation methods have been used since ancient times, though it was unknown then that the process created nanomaterials. Many routes have come into existence in recent years, more than one work could possibly discuss in detail. This work will focus on co-precipitation, thermal degradation, solvothermal, and electrochemical methods, but microwave-assisted[22], laser-induced fragmentation, and ionic liquid[23] methods are known in the literature.

Several routes for nonaqueous nanomaterial synthesis exist. Of them, thermal degradation and solvothermal methods have been specifically been utilized by this lab. The thermal degradation synthesis, often our primary route to generate new nanomaterials, has shown itself to be a very powerful and versatile tool[24-26]. A metal salt, often an acetate or acetylacetate, is placed into a high boiling point solvent in the presence of a surfactant. The reaction is heated to the boiling point of the solvent (> 200 °C) where the metal salt begins to decompose and starts to form nanoparticle nucleates that are limited in their growth by the surfactant. This route is known for producing small nanoparticles (less than 10 nm in diameter) capped in surfactant with very good monodispersity and crystallinity. A more detailed discussion of the thermal degradation synthesis will be presented in Chapter 2. A solvothermal synthesis was also briefly employed by this lab for the generation of nanomaterials. This method again involves metal salts, but this time

they are placed in a stabilizing organic solvent such as benzyl ether[27-29]. The whole reaction is then placed into a Teflon lined digestion bomb and heated to high temperatures (~ 200 °C) over the course of 1 or more days. The resulting nanomaterial is pseudo-capped with the stabilizing solvent which can easily be removed by additional washing. This method will also be discussed in more detail in Chapter 2.

Recently an electrochemical route was developed for synthesizing iron oxide nanoparticles[30-32]. The method involves a sacrificial iron anode, an iron cathode, and a reference electrode hooked to a standard potentiostat. The electrodes are placed into an electrolyte solution and separated by a specific distance. A voltage is applied, generating nanoparticles at the anode. Adjusting both the current density and the voltage yields control over the size and shape iron oxide nanoparticles formed. A surfactant is sometimes used to prevent flocculation, but methods exist where no surfactant is used.

1.2 Surface Modification of Metal Oxide Nanoparticles

As mentioned above, there is vast potential for MO_x nanoparticles in a wide range of applications. However, many of these applications require that the nanoparticles be durable and compatible with the environment of the application. This is especially important for biological applications as the nanoparticle need maintain their desired properties while limiting their toxicity to the body. Much of the solubility and durability of nanoparticles come from how their surface is passified. Having no surface protection often leads to flocculation or aggregation as time progresses. The need to control surface chemistry has led to many different methods for modifying the surface of nanoparticles to make them more suitable to their new environment. Nanoparticles synthesized via co-precipitation, solvothermal, or electrochemical methods are considered to have “bare” surfaces capable of easy modification. Those nanoparticles

synthesized by high temperature degradation are covered in surfactant, which leads to a competitive interaction during surface modification, making the process more challenging. However, many different molecules readily interact with a MO_x surface providing a wide range of molecules and surface chemistries to work with. The most common molecules involved are carboxylic acids, amines, phosphates and phosphonates, and silanes[33]. Each of these provides a unique type of binding to the MO_x surface, with carboxylic acids and amines chemisorbing while phosphates, phosphonates, and silanes are capable of multiple covalent bonds to the metal ion present at the surface.

Carboxylic acids and amines are commonly used to modify the solubility properties of a MO_x nanoparticle by changing its surface charge[30, 34-35]. For instance, citric acid is often used to replace the surfactant on nonaqueous iron oxide nanoparticles to make them soluble in water[36]. Many of the surfactants used in thermal degradation synthesis are also carboxylic acids or amines attached to very long carbon chains[37-38]. As such, it is the functional group that interacts with the MO_x surface via adsorption or chemisorption between the electronegative oxygens/nitrogen and the positively charged metal ions. Since the primary form of bonding is not covalent, the ligands are capable of detaching from the MO_x surface and forming an equilibrium with the solution around them, this is especially true in the case of adsorbed molecules. This means that carboxylate and amine capped nanoparticles can eventually lose their coating and begin to aggregate or flocculate in their environment. Coating a MO_x nanoparticle with a carboxylate or amine is usually very simple. The desired ligand is added to a solution of nanoparticles and stirred until the appropriate polarity change occurs which causes the nanoparticles to crash out of their original solution or transfer to another solvent. For instance, this lab has transferred IrO_2 nanoparticles from their as-synthesized water solution to DCM

containing valeric acid just by continued stirring overnight[39]. The purple color of the IrO_2 nanoparticles can be visually observed as it transfers over to the DCM layer.

In order to achieve long term surface control, a more powerful bonding option must be used, preferably something capable of covalent interaction. Silanes, which are well known for their bonding with bulk MO_x surfaces, make an attractive option for long term surface modification. Silanes are known to readily react with surface -OH groups to form covalent M-O-Si bonds[40-43]. They are capable of being mono, di, and tridentate ligands based on their design and can be synthesized with a wide variety of R groups. They are also inexpensive and commercially available. However, silanes do possess some limitations, namely homo-condensation and poor stability outside the pH range of 4-10. Homo-condensation, which occurs when Si-O-Si bonds are formed between different silane molecules, often causes the silane to "chain", creating large polymer networks which encapsulate nanoparticles. This polymerization makes it very difficult to try and quantify any surface modification that occurs and can be limited, but not completely prevented, by carefully controlling the reaction environment or by limiting the reagents to less reactive or monodentate silanes. Silanes are also susceptible to hydrolytic cleavage in strongly acidic or basic environments. Essentially, bonds are broken as H^+ (in the case of acid environments) or OH^- (in basic environments) react with Si to recreate Si-H or Si-OH bonds. Bulky side groups can help limit the effects of hydrolytic cleavage, but extended operation outside of pH 4-10 will eventually lead to removal of the silane layer. A series of silanes were used to modify ITO and ZrO_2 nanoparticles and will be discussed in more detail in Chapters 3 and 4.

Phosphates and phosphonates provide an additional option for long term surface modification due to their enhanced bond strength and multidentate nature[44]. They are known to

bind with most non-silicon MO_x surfaces and, like silanes, can be mono, di, or tridentate in their binding and can be customized during synthesis to satisfy any R group needs. Unlike silanes, the M-O-P bonds formed at the MO_x surface are much less susceptible to hydrolysis and are incapable of homo-condensation to polymerize. This makes them ideal for quantifying nanoparticle surface modification. Phosphate ligands have been used to anchor azide groups to nanoparticle surfaces to allow for further modification via click chemistry[45]. Chapter 4 will further explore nanoparticles with phosphate surfaces.

1.3 Functionalization of Metal Oxide Nanoparticles

The major focus behind modifying the surface of a nanoparticle is to provide groundwork for its functionalization to give it the properties needed to work with the application in mind. For instance, nanoparticles for biological applications must be soluble in water and stable at physiological pH[40, 46]. This is not the case for many as-synthesized nanoparticles, so they must be modified with a ligand that provides those qualities with a strong surface attachment. There are numerous ways routes to functionalize nanoparticles, however it is easiest to divide them into two separate orders of operation, single step and multistep functionalization. In a single step functionalization, the molecule that is attached to the surface already has the desired functionality. All synthetic steps for the ligand are completed before it is used. All that remains is to attach the ligand to the surface and remove any excess. This is the preferred method of functionalization. However, there are often problems with only using a single step, namely unexpected reaction sites and incompatibilities during the functionalization (i.e., trying to react a non-polar nanoparticle with an aqueous ligand). To mitigate this, functionalization can also be done through a multistep process. A multistep functionalization usually involves steps where an active site is anchored to the nanoparticle surface and then the desired functionality is reacted

with the active site. They are certainly not limited to two-steps, but each additional step adds more work-up and decreases yield. This work discusses both single step and multistep functionalization in Chapters 3, 4, and 5.

Several common organic reactions can be used to modify an attached ligand in a multistep functionalization of a nanoparticle. Often, the limiting factor is the terminal groups available to be reacted. Primary amines make a very attractive choice, assuming your original ligand is capable of supporting one[42]. Amines are polar enough to widen solvent choices and are the target of many powerful coupling techniques, specifically acyl chloride and carbodiimide[47] couplings. Previous work from the Murray Lab showed how carbodiimide coupling could be used to modify the terminal amine groups of a 3-aminopropyltrimethoxysilane ligand shell on SiO_2 nanoparticles with an electroactive ferrocene tag[48]. They were then able to electrochemicaly determine the number of ferrocenes and predict the surface coverage of the SiO_2 nanoparticles, estimating ~600 individual electron transfers per nanoparticle. Carbodiimide coupling is very effective but it is a relatively slow reaction with several biproducts that can be formed resulting in additional purification steps. Much this work uses acyl chloride coupling with the primary amine to provide adequate functionalization. Acyl chloride reagents are very reactive and have to be handled very carefully under inert atmosphere but also provide enhanced reactivity and ease of use. Acyl chlorides can easily be made from simple carboxylic acids and readily undergo nucleophilic attack from the primary amine to create a bond between the two reagents. If the carboxylic acid is attached to an electrochemical moiety, such as a ferrocene group, the coupling can easily be detected through electrochemical analysis. Chapters 2 and 3 discuss using terminal amine silanes and their modification with acyl chloride reagents.

Recently, another way of modifying surfaces has afforded a degree of fame, the so called "click" reactions[15, 45, 49]. Click reactions are simple ways of combining two types of small molecules and are typically required to be modular, high yielding, and stereoselective while producing very inoffensive by-products. Perhaps the most notable of the Click reactions is the azide-alkyne Huisgen cycloaddition where an azide group cyclizes after coming into contact with a terminal alkyne group. This reaction is typically very slow, but can be catalyzed by the presence of Cu(I) in solution, often made in solution by reducing $CuSO_4$ with sodium ascorbate. There are many examples in the literature showing how metal oxide surfaces can be modified by using phospho-azide materials to bind with the surface then reacting them with an alkyne terminated function group. In 2010 the Xian group of East China Normal University showed a way to modify iron oxide nanoparticles with ferrocene to create a magnetic electrochemical switch[50]. Using a previously reported synthesis for a phosphor-azide ligand[45] they were able to remove the original surfactant layer and replace it with this new phosphate ligand. They were then able to perform a click reaction using ethynylferrocene to graft an electroactive tag to the phosphate support and detect its presence with electrochemistry. Since phosphates do not polymerize this provides an attractive route to generate a monolayer of ferrocene on the surface of MO_x nanoparticles. Chapter 4 will discuss using this route to modify the surface of IrO_2 and ZrO_2 nanoparticles.

1.4 References

1. Nozik, A. J.; Beard, M. C.; Luther, J. M.; Law, M.; Ellingson, R. J.; Johnson, J. C., Semiconductor Quantum Dots and Quantum Dot Arrays and Applications of Multiple Exciton Generation to Third-Generation Photovoltaic Solar Cells. *Chem. Rev.* **2010,** *110* (11), 6873-6890.

2. Carpenter, A. W.; Johnson, J. A.; Schoenfisch, M. H., Nitric Oxide-Releasing Silica Nanoparticles with Varied Surface Hydrophobicity. *Colloids and Surfaces A: Physicochemical and Engineering Aspects* (0).

3. Parker, J. F.; Fields-Zinna, C. A.; Murray, R. W., The Story of a Monodisperse Gold Nanoparticle: Au25L18. *Acc. Chem. Res.* **2010,** *43* (9), 1289-1296.

4. Johnson, B. F. G., Nanoparticles in Catalysis. *Top. Catal.* **2003,** *24* (1-4), 147.

5. Jung, J. H., Functionalized magnetic nanoparticles as chemosensors and adsorbents for toxic metal ions in environmental and biological fields. *Chem. Soc. Rev.* **2011,** *40* (9), 4464.

6. Schladt, T. D.; Schneider, K.; Schild, H.; Tremel, W., Synthesis and bio-functionalization of magnetic nanoparticles for medical diagnosis and treatment. *Dalton Transactions* **2011,** *40* (24), 6315-6343.

7. Yiu, H. H. P., Engineering the multifunctional surface on magnetic nanoparticles for targeted biomedical applications: a chemical approach. *Nanomedicine* **2011,** *6* (8), 1429-1446.

8. Kamat, P. V., Graphene-Based Nanoarchitectures. Anchoring Semiconductor and Metal Nanoparticles on a Two-Dimensional Carbon Support. *The Journal of Physical Chemistry Letters* **2009,** *1* (2), 520-527.

9. Dahl, J. A.; Maddux, B. L. S.; Hutchison, J. E., Toward Greener Nanosynthesis. *Chem. Rev.* **2007,** *107* (6), 2228-2269.

10. Cuenya, B. R., Synthesis and catalytic properties of metal nanoparticles: Size, shape, support, composition, and oxidation state effects. *Thin Solid Films* **2010,** *518* (12), 3127-3150.

11. Gambardella, A. A.; Bjorge, N. S.; Alspaugh, V. K.; Murray, R. W., Voltammetry of Diffusing 2 nm Iridium Oxide Nanoparticles. *The Journal of Physical Chemistry C* **2011,** *115* (44), 21659-21665.

12. Joris, F.; Manshian, B. B.; Peynshaert, K.; De Smedt, S. C.; Braeckmans, K.; Soenen, S. J., Assessing nanoparticle toxicity in cell-based assays: influence of cell culture parameters and optimized models for bridging the in vitro-in vivo gap. *Chem. Soc. Rev.* **2013,** *42* (21), 8339-8359.

13. Mingwu, S.; Hongdong, C.; Xifu, W.; Xueyan, C.; Kangan, L.; Su He, W.; Rui, G.; Linfeng, Z.; Guixiang, Z.; Xiangyang, S., Facile one-pot preparation, surface functionalization, and toxicity assay of APTS-coated iron oxide nanoparticles. *Nanotechnology* **2012,** *23* (10), 105601.

14. Xie, J.; Chen, K.; Lee, H.-Y.; Xu, C.; Hsu, A. R.; Peng, S.; Chen, X.; Sun, S., Ultrasmall c(RGDyK)-Coated Fe3O4 Nanoparticles and Their Specific Targeting to Integrin αvβ3-Rich Tumor Cells. *J. Am. Chem. Soc.* **2008,** *130* (24), 7542-7543.

15. Hayashi, K.; Ono, K.; Suzuki, H.; Sawada, M.; Moriya, M.; Sakamoto, W.; Yogo, T., One-Pot Biofunctionalization of Magnetic Nanoparticles via Thiol−Ene Click Reaction for Magnetic Hyperthermia and Magnetic Resonance Imaging. *Chem. Mater.* **2010,** *22* (12), 3768-3772.

16. Zhang, C.; Wängler, B.; Morgenstern, B.; Zentgraf, H.; Eisenhut, M.; Untenecker, H.; Krüger, R.; Huss, R.; Seliger, C.; Semmler, W.; Kiessling, F., Silica- and Alkoxysilane-Coated Ultrasmall Superparamagnetic Iron Oxide Particles: A Promising Tool To Label Cells for Magnetic Resonance Imaging. *Langmuir* **2006,** *23* (3), 1427-1434.

17. Jeon, M.-K.; Kang, M., Synthesis and characterization of indium-tin-oxide particles prepared using sol–gel and solvothermal methods and their conductivities after fixation on polyethyleneterephthalate films. *Mater. Lett.* **2008,** *62* (4–5), 676-682.

18. Hoertz, P. G.; Chen, Z.; Kent, C. A.; Meyer, T. J., Application of High Surface Area Tin-Doped Indium Oxide Nanoparticle Films as Transparent Conducting Electrodes. *Inorg. Chem.* **2010,** *49* (18), 8179-8181.

19. Wöhler, L.; Witzmann, W., Die Oxyde des Iridiums. *Zeitschrift für anorganische Chemie* **1908,** *57* (1), 323-352.

20. Han, C.-H.; Han, S.-D.; Gwak, J.; Khatkar, S. P., Synthesis of indium tin oxide (ITO) and fluorine-doped tin oxide (FTO) nano-powder by sol–gel combustion hybrid method. *Mater. Lett.* **2007,** *61* (8–9), 1701-1703.

21. Liu, S.-m.; Ding, W.-y.; Chai, W.-p., Preparation and characterization of highly dispersed and crystallised ITO nanoparticles. *Mater. Lett.* **2011,** *65* (9), 1272-1275.

22. Kijima, N.; Yoshinaga, M.; Awaka, J.; Akimoto, J., Microwave synthesis, characterization, and electrochemical properties of α-Fe2O3 nanoparticles. *Solid State Ionics* **2011,** *192* (1), 293-297.

23. Bühler, G.; Thölmann, D.; Feldmann, C., One-Pot Synthesis of Highly Conductive Indium Tin Oxide Nanocrystals. *Adv. Mater.* **2007,** *19* (17), 2224-2227.

24. Sun, S.; Zeng, H.; Robinson, D. B.; Raoux, S.; Rice, P. M.; Wang, S. X.; Li, G., Monodisperse MFe2O4 (M = Fe, Co, Mn) Nanoparticles. *J. Am. Chem. Soc.* **2003,** *126* (1), 273-279.

25. Sun, Z.; He, J.; Kumbhar, A.; Fang, J., Nonaqueous Synthesis and Photoluminescence of ITO Nanoparticles. *Langmuir* **2010,** *26* (6), 4246-4250.

26. Zhang, Z.; Lu, M.; Xu, H.; Chin, W.-S., Shape-Controlled Synthesis of Zinc Oxide: A Simple Method for the Preparation of Metal Oxide Nanocrystals in Non-aqueous Medium. *Chemistry – A European Journal* **2007,** *13* (2), 632-638.

27. Ba, J.; Feldhoff, A.; Fattakhova Rohlfing, D.; Wark, M.; Antonietti, M.; Niederberger, M., Crystallization of Indium Tin Oxide Nanoparticles: From Cooperative Behavior to Individuality. *Small* **2007,** *3* (2), 310-317.

28. Ba, J.; Fattakhova Rohlfing, D.; Feldhoff, A.; Brezesinski, T.; Djerdj, I.; Wark, M.; Niederberger, M., Nonaqueous Synthesis of Uniform Indium Tin Oxide Nanocrystals and Their Electrical Conductivity in Dependence of the Tin Oxide Concentration. *Chem. Mater.* **2006,** *18* (12), 2848-2854.

29. Sasaki, T.; Endo, Y.; Nakaya, M.; Kanie, K.; Nagatomi, A.; Tanoue, K.; Nakamura, R.; Muramatsu, A., One-step solvothermal synthesis of cubic-shaped ITO nanoparticles precisely controlled in size and shape and their electrical resistivity. *J. Mater. Chem.* **2010,** *20* (37), 8153-8157.

30. Cabrera, L.; Gutierrez, S.; Menendez, N.; Morales, M. P.; Herrasti, P., Magnetite nanoparticles: Electrochemical synthesis and characterization. *Electrochim. Acta* **2008,** *53* (8), 3436-3441.

31. Pascal, C.; Pascal, J. L.; Favier, F.; Elidrissi Moubtassim, M. L.; Payen, C., Electrochemical Synthesis for the Control of γ-Fe2O3 Nanoparticle Size. Morphology, Microstructure, and Magnetic Behavior. *Chem. Mater.* **1998,** *11* (1), 141-147.

32. Fajaroh, F.; Setyawan, H.; Widiyastuti, W.; Winardi, S., Synthesis of magnetite nanoparticles by surfactant-free electrochemical method in an aqueous system. *Adv. Powder Technol.* **2012,** *23* (3), 328-333.

33. Neouze, M.-A.; Schubert, U., Surface Modification and Functionalization of Metal and Metal Oxide Nanoparticles by Organic Ligands. *Monatshefte für Chemie / Chemical Monthly* **2008,** *139* (3), 183-195.

34. Lattuada, M.; Hatton, T. A., Functionalization of Monodisperse Magnetic Nanoparticles. *Langmuir* **2006,** *23* (4), 2158-2168.

35. Harris, L. A.; Goff, J. D.; Carmichael, A. Y.; Riffle, J. S.; Harburn, J. J.; St. Pierre, T. G.; Saunders, M., Magnetite Nanoparticle Dispersions Stabilized with Triblock Copolymers. *Chem. Mater.* **2003,** *15* (6), 1367-1377.

36. Campelj, S.; Makovec, D.; Drofenik, M., Preparation and properties of water-based magnetic fluids. *J. Phys.: Condens. Matter* **2008,** *20* (20), 204101.

37. Gilstrap, R. A.; Capozzi, C. J.; Carson, C. G.; Gerhardt, R. A.; Summers, C. J., Synthesis of a Nonagglomerated Indium Tin Oxide Nanoparticle Dispersion. *Adv. Mater.* **2008,** *20* (21), 4163-4166.

38. Choi, S.-I.; Nam, K. M.; Park, B. K.; Seo, W. S.; Park, J. T., Preparation and Optical Properties of Colloidal, Monodisperse, and Highly Crystalline ITO Nanoparticles. *Chem. Mater.* **2008,** *20* (8), 2609-2611.

39. Gambardella, A. A. On the Characterization of Small Iridium Oxide Nanoparticles. University of North Carolina at Chapel Hill, 2013.

40. Bruce, I. J.; Sen, T., Surface Modification of Magnetic Nanoparticles with Alkoxysilanes and Their Application in Magnetic Bioseparations. *Langmuir* **2005,** *21* (15), 7029-7035.

41. Čampelj, S.; Makovec, D.; Drofenik, M., Functionalization of magnetic nanoparticles with 3-aminopropyl silane. *J. Magn. Magn. Mater.* **2009,** *321* (10), 1346-1350.

42. del Campo, A.; Sen, T.; Lellouche, J.-P.; Bruce, I. J., Multifunctional magnetite and silica–magnetite nanoparticles: Synthesis, surface activation and applications in life sciences. *J. Magn. Magn. Mater.* **2005,** *293* (1), 33-40.

43. Yamaura, M.; Camilo, R. L.; Sampaio, L. C.; Macêdo, M. A.; Nakamura, M.; Toma, H. E., Preparation and characterization of (3-aminopropyl)triethoxysilane-coated magnetite nanoparticles. *J. Magn. Magn. Mater.* **2004,** *279* (2–3), 210-217.

44. Polito, L.; Monti, D.; Caneva, E.; Delnevo, E.; Russo, G.; Prosperi, D., One-step bioengineering of magnetic nanoparticles via a surface diazo transfer/azide-alkyne click reaction sequence. *Chemical communications (Cambridge, England)* **2008,** (5), 621-623.

45. White, M. A.; Johnson, J. A.; Koberstein, J. T.; Turro, N. J., Toward the Syntheses of Universal Ligands for Metal Oxide Surfaces: Controlling Surface Functionality through Click Chemistry. *J. Am. Chem. Soc.* **2006,** *128* (35), 11356-11357.

46. Barrera, C.; Herrera, A. P.; Rinaldi, C., Colloidal dispersions of monodisperse magnetite nanoparticles modified with poly(ethylene glycol). *J. Colloid Interface Sci.* **2009,** *329* (1), 107-113.

47. Mikhaylova, M.; Kim, D. K.; Berry, C. C.; Zagorodni, A.; Toprak, M.; Curtis, A. S. G.; Muhammed, M., BSA Immobilization on Amine-Functionalized Superparamagnetic Iron Oxide Nanoparticles. *Chem. Mater.* **2004,** *16* (12), 2344-2354.

48. Beasley, C. A.; Murray, R. W., Voltammetry and Redox Charge Storage Capacity of Ferrocene-Functionalized Silica Nanoparticles. *Langmuir* **2009,** *25* (17), 10370-10375.

49. Hayashi, K.; Moriya, M.; Sakamoto, W.; Yogo, T., Chemoselective Synthesis of Folic Acid−Functionalized Magnetite Nanoparticles via Click Chemistry for Magnetic Hyperthermia. *Chem. Mater.* **2009,** *21* (7), 1318-1325.

50. Peng, R.; Zhang, W.; Ran, Q.; Liang, C.; Jing, L.; Ye, S.; Xian, Y., Magnetically Switchable Bioelectrocatalytic System Based on Ferrocene Grafted Iron Oxide Nanoparticles. *Langmuir* **2011,** *27* (6), 2910-2916.

CHAPTER 2 – SYNTHESIS OF METAL OXIDE NANOPARTICLES BY THERMAL DEGRADATION AND SOLVOTHERMAL ROUTES

2.1 Introduction

Synthesis of MO_x nanoparticles can be done in a multitude of different ways, but no method provides a universal way to create nanoparticles for all desired specifications[1]. Instead, each synthesis provides control over a small set of parameters, allowing for synthetic selection based on which properties are most important for the work at hand. For instance, our lab is interested in nanoparticles less than 10 nm in diameter. Once nanoparticles enter this size regime they begin to act less like clusters and more like individual molecules. $Au_{25}L_{18}$ is a remarkable example of this. Due to its small size (1.1 nm in diameter) electrochemical detection can reveal the energy levels of the HOMO and LUMO gap[2], something that would be nearly impossible to see in a large nanomaterial or a nanomaterial with a large size distribution. Therefore, in order study molecule like nanoparticles, a synthesis capable of generating small nanoparticles with great monodispersity is required.

There are several synthetic routes to producing small (<10 nm) nanoparticles, though most often co-precipitation, thermal degradation (TD), or solvothermal methods are chosen. Unfortunately, none of these methods are capable of producing the perfect nanoparticle for every possible application. Instead, each of them offers distinct advantages and disadvantages which must be weighed before a synthetic pathway can be selected. Typically, co-precipitation methods

are easy to perform and can produce very small "naked" nanoparticles but lack monodispersity and crystallinity. Thermal degradation makes reproducibly small nanoparticles with high monodispersity and crystallinity, but require difficult post-synthesis work to remove their protective surfactant shell. Solvothermal methods are also very easy to perform and produce small nanoparticles with an easy to remove protective layer, but have long reactions times (24-72 hrs). The majority of the work presented here uses a high temperature degradation synthesis; one experiment via a solvothermal synthesis will be briefly mentioned as well.

2.1.1 Metal Oxide Nanoparticles via Thermal Degradation Synthesis

Thermal degradation syntheses use very high temperatures (~ 250° C – 350° C) to cause the breakdown of an organometallic salt, often in the presence of a fatty surfactant to limit crystalline growth. Metal acetates and acetylacetonates are most frequently used as the metal precursor since the acetates and acetylacetonates are capable of condensation at high temperatures. Other metallic salts have been shown work as well, but acetates and acetylacetonates are favored. The literature also shows a wide range of surfactants in use; they often have a carboxylic acid or amine functional groups to interact with the metal oxide surface[3-6]. These moieties passify the growth of specific crystalline planes, controlling nanoparticle growth. Several works use oleylamine and/or oleic acid, both of which are C18 carbon chains with centrally situated double bond, though both are environmentally dangerous and air sensitive. Other groups have used ligands that are solids at room temperature, such as myristic acid and octadecylamine, knowing that the high temperatures will melt them prior to the reaction starting. Due to the high temperatures involved, high boiling point solvents (HBPS) such as 1-octadecene, dipenyl ether, benzyl ether, or dodecane are used to prevent solvent evaporation. The reaction temperature is often set to the boiling point of the solvent, so the solvent chosen has

the ability to limit the energy put into the reaction. Reactions are often vacuum or argon purged at a lower temperature to remove excess oxygen and allow the reagents to sufficiently dissolve in the HBPS. At the end of the reaction the surfactant-capped nanoparticles form a colloidal suspension with the HBPS and can be precipitated by adding a polar solvent like ethanol.

Thermal degradation has proven to be very versatile in regards to the number of materials it can be used for. The literature has shown successful synthesis of Fe_2O_3, Fe_3O_4, ITO, ZrO_2, CdSe, ZnO_2, and Bi_2S_3. As long as a stable acetate or acetylacetonate exists for a chosen metal, thermal degradation should be able to produce nanoparticles. Nearly all of these syntheses produce nanoparticles with diameters less than 10 nm, with some nanoparticles measuring only 2 nm in diameter. The size of the nanoparticles can also be tuned by manipulating the parameters of the reaction. For instance, changing the solvent from diphenyl ether (T_{bp} = 258° C) to benzyl ether (T_{bp} = 298° C) changes Fe_3O_4 nanoparticle products from 3 nm in diameter to 6 nm[4]. Changing the surfactants or surfactant concentration, essentially the ability to limit crystalline growth, can also cause a significant change in size and shape[7]. Replacing oleylamine and oleic acid with myristic acid and octadecylamine shows ITO nanoparticle diameter changing from 5.6 nm[5] to 6.5 nm[8]. With so many parameters to manipulate, a wide range of nanomaterials of varying sizes can be created with relative ease. The only major drawback of the thermal degradation synthesis is also its defining feature - the surfactant shell. The shell protects the MO_x cores from interacting with each other, preventing flocculation and agglomeration. It also makes the nanoparticles insulated and non-polar which prevents them from being used in many biological and electrical applications. In order to use them for such applications they must have their surfaces modified with a more manageable ligand. This additional step sometimes causes this synthesis to be viewed unfavorably, but high batch reproducibility coupled with good

monodispersity and crystallinity make it a very attractive synthesis for analytically examining small nanoparticles.

2.1.2 Metal Oxide Nanoparticles via Solvothermal Synthesis

Solvothermal methods heavily rely on the slower reaction kinetics that occur in organic solvents[9]. The slower reactions allow for a higher degree of synthetic control during the nanoparticle growth stage. Solvothermal nanoparticles are also "gently" capped, meaning their protective layer can easily be removed by repeated washing yielding a naked" nanoparticle[10]. Solvothermal reactions utilize the same organometallic salts as high temperature thermal degradations, but require a special reaction vessel commonly referred to as an autoclave. Though they share the same name, this is not the same device commonly used by biological scientists to sterilize equipment and waste. The autoclave used in these experiments is actually an acid digestion bomb, commonly associated with Parr Instruments. The metal precursors are suspended in benzyl alcohol, which acts as a weak capping ligand, (other HBPS may be used) and placed into the acid digestion bomb. The bomb is then placed into a furnace and heated just below the boiling point of the solvent for 1-3 days. The solution is then centrifuged and excess chloroform added to remove excess benzyl alcohol. The result is a "naked" nanoparticle film with moderate yield (~50%).

Solvothermal syntheses are less versatile, compared to TD syntheses, due to fewer tunable parameters. The synthesis is primarily controlled by timing the experiment, changing the solvent, or manipulating starting concentrations. Even though there are fewer parameters, synthetic control can still be achieved. ITO nanoparticles were found to vary from 6.2 nm to 12.7 nm based on a 12 hr to 48 hr reaction time[11]. The lack of numerous parameters does offer some advantages. Solvothermal syntheses are comparatively much simpler than TD, making them

ideal labs with minimal synthetic capability. Simply place the reagents in the bomb, heat, and wait. These reactions are also highly reproducible since the reaction is dependent on 1) an oven with accurate temperature control and 2) a good timer. Accurate temperature control is important since if the solvent boils too vigorously, the pressure can warp the acid digestion bomb's Teflon container, ruining the seal and requiring a costly replacement. Solvothermal syntheses are excellent for creating and characterizing nanoparticle films. The nanoparticle powder can easily be suspended and applied to glass or conductive slides. The "naked" nanoparticle surfaces also lends itself towards surface modification experiments, however they are nearly impossible to disperse in solution without prior modification. Their unpacified surface can also lead to flocculation which can make analytical surface measurements difficult. Ultimately, the time required to make solvothermal nanoparticles was judged too time consuming, and the TD method was chosen as the primary synthetic method.

2.2 Experimental

2.2.1 Chemicals and Materials

Indium(III) acetate ($In(ac)_3$; 99.99%), tin(II) (acetate) ($Sn(ac)_2$; 99.99%) were obtained from Alfa Aeser, indium(III) acetylacetonate ($In(acac)_3$; 99.99%), tin(IV) bis(acetylacetonate) dichloride ($Sn(acac)_2Cl_2$; 98%), ruthenium(III) acetylacetonate ($Ru(acac)_3$; 97%), iridium(III) acetylacetonate ($Ir(acac)_3$; 97%), zirconium(IV) acetate hydroxide ($Zr(ac)_xOH_y$), zirconium(IV) acetylacetonate ($Zr(acac)_4$; 98%), bismouth(III) acetate ($Bi(acac)_3$; 99.99%), oleylamine ($C_9H_{18}=C_9H_{17}NH_2$; 80-90%), oleic acid ($C_9H_{18}=C_8H_{15}COOH$; 97%), myristic acid ($CH_3(CH_2)_{12}COOH$; 99%), octadecylamine ($CH_3(CH_2)_{17}NH_2$; 90%), sulfur (S; 99.5), octadecene ($C_{16}H_{33}=CH_2$; 90%), benzyl alcohol ($C_6H_5CH_2OH$; >99%) from Sigma-Aldrich. Acetonitrile

(CH_3CN), absolute ethanol, hexanes, dichloromethane (DCM), petroleum ether, toluene, and chloroform obtained from Fisher Scientific were dried over 4 Angstrom molecular sieves.

2.2.2 Instrumentation

Programmable Temperature Control Unit. A lab constructed device controlled by a CAL 9500P programmable process controller with attached to a thermal couple was used to accurately control synthesis temperatures.

High Resolution Transmission Electron Microscopy (TEM). TEM images were obtained on a JEOL 2010F FasTEM on nanoparticle samples prepared on copper grids (200 carbon mesh, carbon-coated Formvar; Ted Pella, Redding, CA)

Energy-Dispersive X-Ray Spectroscopy (EDS). EDS analysis was performed using Oxford INCA EnergyTEM 250 TEM microanalysis system attached to the JEOL 2010F FasTEM.

Centrifuge. Centrifugation was done with an Eppendorf 5810 centrifuge with a fixed-angle rotator at 3000-4000 rpm for 10 minutes.

X-Ray Photoelectric Spectroscopy (XPS). XPS data were taken on a Kratos Axis Ultra DLD system with monochromatic Al Kα x-ray source. High resolution scans were taken at pass energy = 20 eV, and the spectral energy axis was aligned at the C 1s peak at 284.6 eV.

Ultraviolet-Visible Spectroscopy (UV-Vis). UV-Vis spectra were taken on a Thermo Evolution Array UV-Vis spectrophotometer (Thermo, Waltham, MA)

2.2.3 Standard Thermal Degradation Synthesis of Metal Oxide Nanoparticles

Metal Oxide nanoparticles were synthesized following the procedure reported by Sun *et al*[5]. A metal acetate (ac) or acetylacetonate (acac) (0.20 mmol), a dopant metal ac or acac (%

wt/wt desired), oleic acid/myristic acid (1.9 mmol), oleylamine/octadecylamine (2.4 mmol), and optionally sulfur (3 mmol) were added to octadecene (5 mL) in a 50 mL 3-neck round bottom flask equipped with a magnetic stir bar, thermocouple and condenser, closing the third port with a septum. Using a 100 mL heating mantle packed with sand to promote even heating, the vessel was evacuated and heated 1 hr at 120˚ C with vigorous stirring. The temperature was then rapidly increased to 320˚ C and the mixture refluxed for an hour, then allowed to cool to room temperature. The cloudy suspension was transferred to a 50 mL centrifugation tube and 40 mL of absolute ethanol was added, precipitating the nanoparticles, followed by centrifugation at 3000 RPM for 10 minutes. This process was repeated three times. The nanoparticles were then taken up into 3 mL of either hexanes or chloroform and stored at room temperature. Solution colors varied dramatically based on the metal used.

2.2.4 Hot Injection Thermal Degradation Synthesis of Metal Oxide Nanoparticles

The procedure was modified from Sun *et al.*[5] A metal acetate (ac) or acetylacetonates (acac) (0.20 mmol), a dopant metal ac or acac (% wt/wt desired), and oleic acid/myristic acid (1.9 mmol) were added to octadecene (5 mL) in a 50 mL 3-neck round bottom flask equipped with a magnetic stir bar, thermocouple and condenser, closing the third port with a septum. Using a 100 mL heating mantle packed with sand to promote even heating, the vessel was evacuated and heated 1 hr at 120 ˚C with vigorous stirring. The temperature was then rapidly increased to 295˚ C at which point oleylamine/octadecylamine (2.4 mmol) (and sulfur (3 mmol) for Bi_2S_3 nanomaterials) in 0.2 mL octadecene was injected via syringe. The solution color typically changed from a bright color (yellow, red) to black after this injection. The reaction was refluxed at 320˚ C for an hour, and the vessel allowed to cool to room temperature. The cloudy suspension was transferred to a 50 mL centrifugation tube and 40 mL of absolute ethanol added,

precipitating the nanoparticles, followed by centrifugation at 3000 RPM for 10 minutes. This process was repeated three times. The nanoparticles were then taken up into 3 mL of either hexanes or chloroform and stored at room temperature. Solution colors varied based on the MO_x material formed (ZrO_2 = orange; IrO_x = Dark Blue; Bi_2S_3/Bi_2O_3 = Black).

2.2.5 Solvothermal Synthesis of ITO Nanoparticles

The solvothermal synthesis used follows the procedure reported by Niederberger *et. al.*[12] Indium(III) acetylacetonate (1.55 mmol) and a wt% (2-30%) tin(IV) acetylacetonate dichloride were placed in an argon purged scintillation vial and stirred for 1 hr. The turbid solution was transferred to a Teflon lined Parr acid digestion bomb and heated at 200° C for 24-48 hr. The cloudy suspension was transferred to a 50 mL centrifugation tube and centrifuged at 3000 RPM for 10 minutes. Excess chloroform was added and the nanoparticles were centrifuged to remove any remaining benzyl alcohol. This process was repeated twice more. The resulting blue powder was dried at 60° C overnight then transferred to a scintillation vial for storage.

2.2.6 Citrate Capped Nanoparticles.

This procedure was modified from Drofenik *et. al.*[13] A 1 mL sample of the hexane dispersed nanoparticles was rotovapped to dryness, the nanoparticles weighed (~5-50 mg) and redissolved in 7.5 mL toluene in a scintillation vial. The toluene solution was added to a solution of citric acid (3 mmol, ~0.6 g) in 7.5 mL DMF which caused the solution to became turbid. The mixture was stirred vigorously at 100 ˚C for 24 hrs, then was transferred to 50 mL centrifuge tubes and the nanoparticles precipitated by adding diethyl ether. They were collected via centrifugation at 6000 RPM for 10 minutes. The red-brown nanoparticle precipitate was washed twice more with fresh diethyl ether and then suspended in 15 mL of pH 2.2 citrate buffer; after 24 hr this yields a homogeneous, yellow solution.

2.2.7 Estimations of Nanoparticle Mass and Composition

Nanoparticle mass and composition was estimated by using the average nanoparticle diameter. The average diameter was found by using TEM images to generate a histogram (n = 50). The nanoparticles were assumed to be completely spherical with a radius equal to ½ the average diameter. Volume was determined by

$$V = \frac{4}{3}\pi r^3$$

where V is volume (nm^3) and r is the radius (nm). The crystalline structure of the nanoparticles was assumed to be similar to that of the bulk material (ZrO_2 = monoclinic[14]; IrO_x = rutile[15]; Bi_2S_3 = orthorhombic[16]; Bi_2O_3 = monoclinic[16]). The volume of the unit cell was calculated from *a*, *b*, and *c* values collected from the literature for the above structures. The volume of the nanoparticle was then divided by the unit cell volume to estimate the number of unit cells present in a single nanoparticle. The number of unit cells could then be related to the number of metal ions and oxygen ions present in the nanoparticle. The number of metal ions was multiplied by its atomic mass and added to the mass of oxygens present yielding a molecular weight for a mole of nanoparticles. Sample masses could be divided by this molecular weight to determine moles of nanoparticles and subsequently the number of nanoparticles present in the sample.

2.3 Results and Discussion

2.3.1 Characterization of ZrO_2 Nanoparticles Prepared by Thermal Degradation Synthesis

ZrO_2 nanoparticles were synthesized predominately by the hot injection method detailed above, using oleic acid and oleylamine. Initially, Zr(ac)OH was used as the metal precursor. NP samples from Zr(ac)OH ranged from orange to brown in color; the nanoparticles, ca. 2 nm in diameter, were dispersible in non-polar solvents. A white precipitate forms at the bottom the

sample vials after about 24 hr., which is believed to be unreacted Zr(ac)OH. Zr(ac)OH has very poor solubility except in strongly acidic solutions, and unreacted material is visible in the final reaction mixture. $Zr(acac)_4$ was tested as a replacement and proved to be an ideal metal precursor. The acetylacetonate solubilizes nicely at high temperatures and produces the same orange-brown solution seen with the acetate with no visible precipitate.

The size of the nanoparticles is difficult to determine based on the TEM images. The ZrO_2 nanoparticles have little contrast against the TEM grid at high magnification. The organic surfactant that covers the nanoparticles also tends to evaporate under high beam intensity, decreasing resolution. As such, the size distribution of the as synthesized nanoparticles can only be estimated from low resolution images. To circumvent this problem, the nanoparticles were capped with citrate following a previously reported procedure[13]. This removes the surfactant layer, allowing higher quality images to be taken. The citrate-ZrO_2 nanoparticles are 1.54 ± 0.26 nm in diameter and are assumed to maintain the same size as the as-synthesized nanoparticles. XPS and EDX were both used to evaluate the elemental composition of the citrate-ZrO_2 nanoparticles. Before citrate capping, XPS peaks are all masked due to photoelectron scattering by the surface surfactant (Fig 2.2a). After citrate capping, the spectrum shows clearly defined Zr 3d peaks at 182.1 and 184.6 eV (Fig. 2.2b). The citrate-ZrO_2 sample shows significantly improved signal compared to that of the as synthesized material. Table 2.1 shows percent in the ZrO nanoparticle samples. The ideal Zr:O ratio would be 0.5 since two oxygens should be present for each zirconium. However, the surfactant shell prevents accurate measurements of the as-synthesized nanoparticles, and citrate-ZrO_2 also includes the contributions from citric acid.

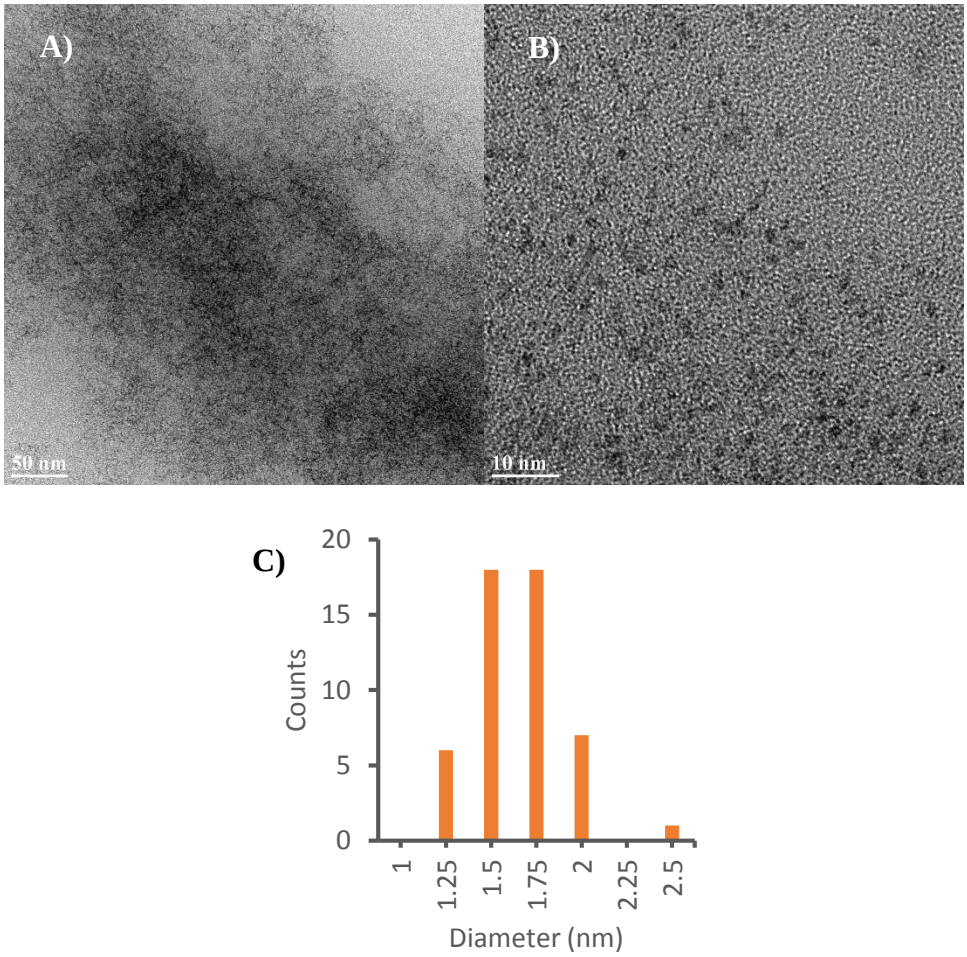

Figure 2.1 –TEM Images of citrate-ZrO_2 nanoparticles (1.5 ± 0.3 nm); panels A and B scale bars are 50 nm and 10 nm, respectively. C shows a histogram of the nanoparticle size dispersion.

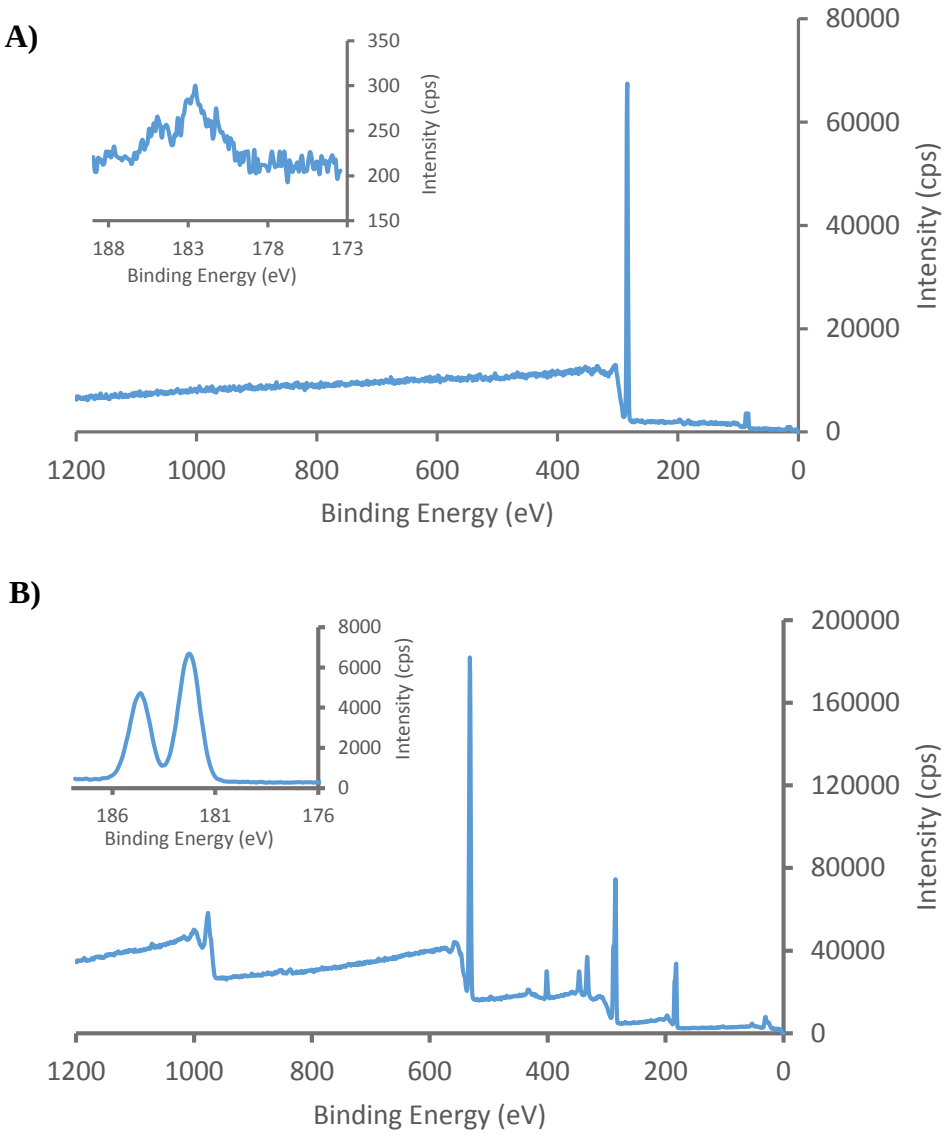

Figure 2.2 – XPS of A) ZrO_2 nanoparticles and B) citrate-ZrO_2 nanoparticles. Insets show the Zr 3d peaks.

Table 2.1 – XPS and EDX Atomic Values for ZrO_2

Sample Name	Method	Zr Atomic Percent (%)	Zr:O Ratio
ZrO	XPS	0.13	0.15
Cit-ZrO	XPS	2.51	0.068

UV/Vis spectra (Fig. 2.3) of as synthesized ZrO nanoparticles in hexanes agree with previously reported spectra for ZrO_2 nanoparticles of a similar size[17]. The nanoparticles have an absorbance maximum at ~236 nm and a shoulder at ~298 nm. These optical band gaps are much lower than the 5.0 eV expected of bulk ZrO.

2.3.2 Characterization of IrO_2 Nanoparticles Prepared by Thermal Degradation Synthesis

IrO_x nanoparticles were synthesized by thermal degradation in an effort to compare the resulting nanoparticles to those achieved by the literature prevalent hydrolytic method[18]. The hydrolytic IrO_2 nanoparticles have many properties of interest, chiefly their ability to lower the overpotential of water oxidation, but tend to have wider size distributions than those achievable by thermal degradation. Ir(III) acetylacetonate was used as the metal precursor in the presence of oleylamine and oleic acid. The resulting dark black solution becomes midnight blue upon sufficient dilution. TEM images (Fig 2.4) showed that the nanoparticles were similar in size to hydrolytic IrO_2, with average diameters of 1.78 ± 0.28. Both XPS (Fig 2.5) and EDX (Fig 2.6) confirm the presence of Ir in the as-synthesized IrO_2 nanoparticles. As expected, the surfactant shell causes the C 1s peaks to dominate the spectra, but high resolution scans show Ir 4f peaks at 61.2 and 64 eV. The EDX, which penetrates through the surfactant shell, shows a Ir:O ratio of 0.43; close to the expected 0.50.

2.3.3 Characterization of Bi_2S_3 and Bi_2O_3 Nanomaterials Prepared by Thermal Degradation Synthesis

Bi_2S_3 nanomaterials were synthesized by both the hot injection method and the standard method. Initial experiments used the hot injection method (HI-Bi_2S_3), where elemental sulfur was dissolved in oleylamine and injected into the reaction vessel at 295 °C. This resulted in a color change from clear to an opalescent black. The HI-Bi_2S_3 nanomaterial was easily

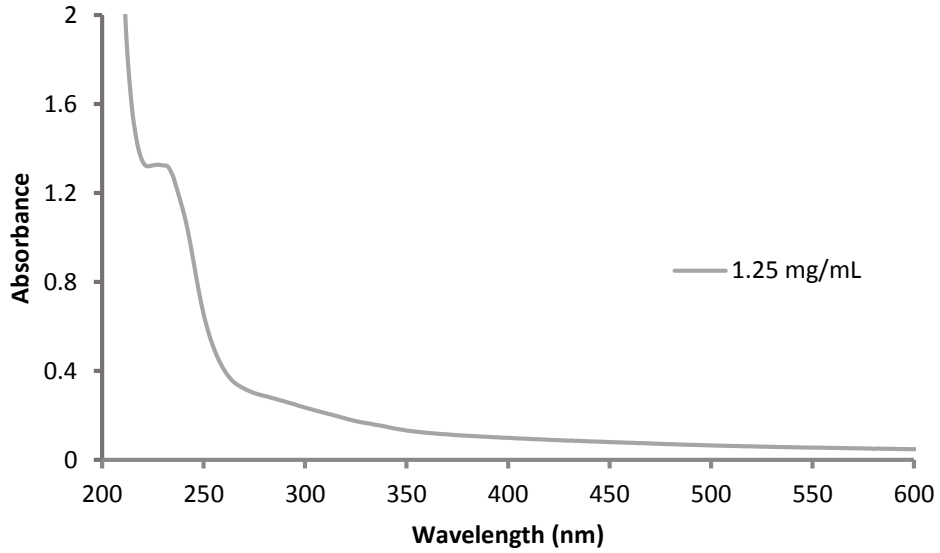

Figure 2.3 - UV/Vis spectrum of a 1.25 mg/mL solution of ZrO_2 nanoparticles in hexanes.

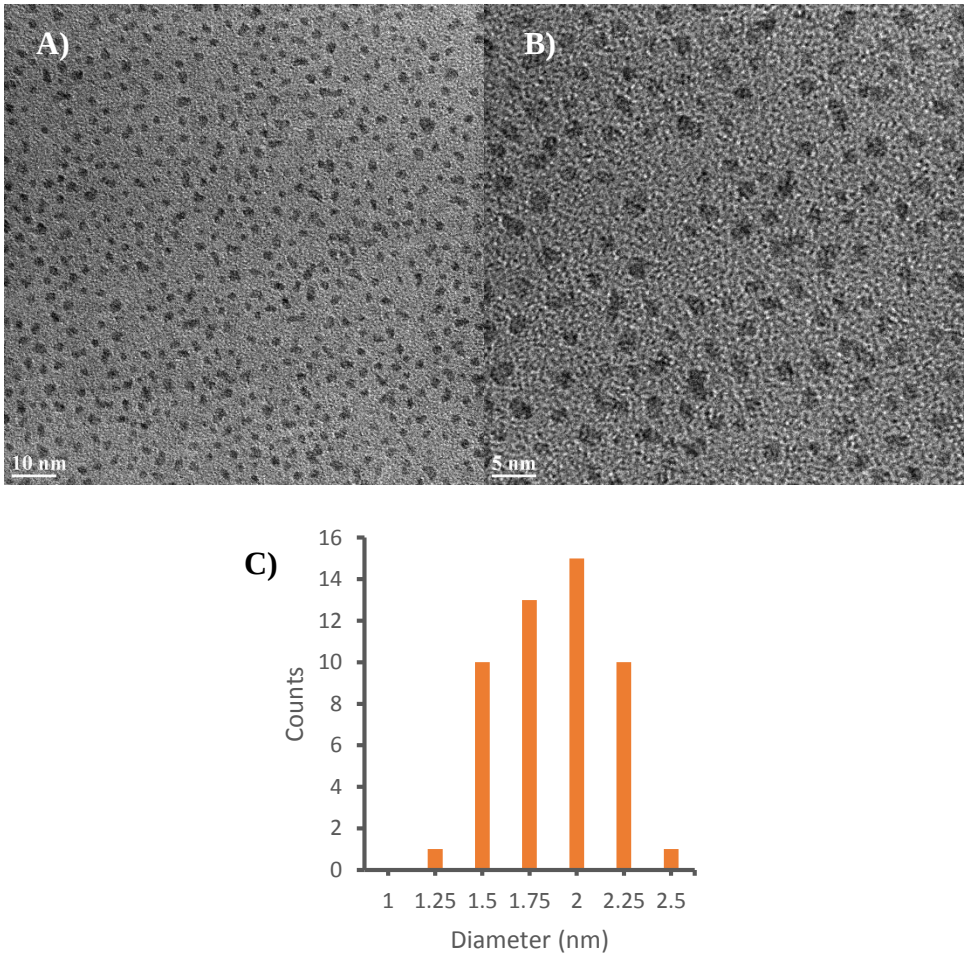

Figure 2.4 – TEM Images of IrO_2 nanoparticles (1.8 ± 0.3 nm); panels A and B scale bars are 10 nm and 5 nm, respectively. C shows a histogram of the nanoparticle size dispersion.

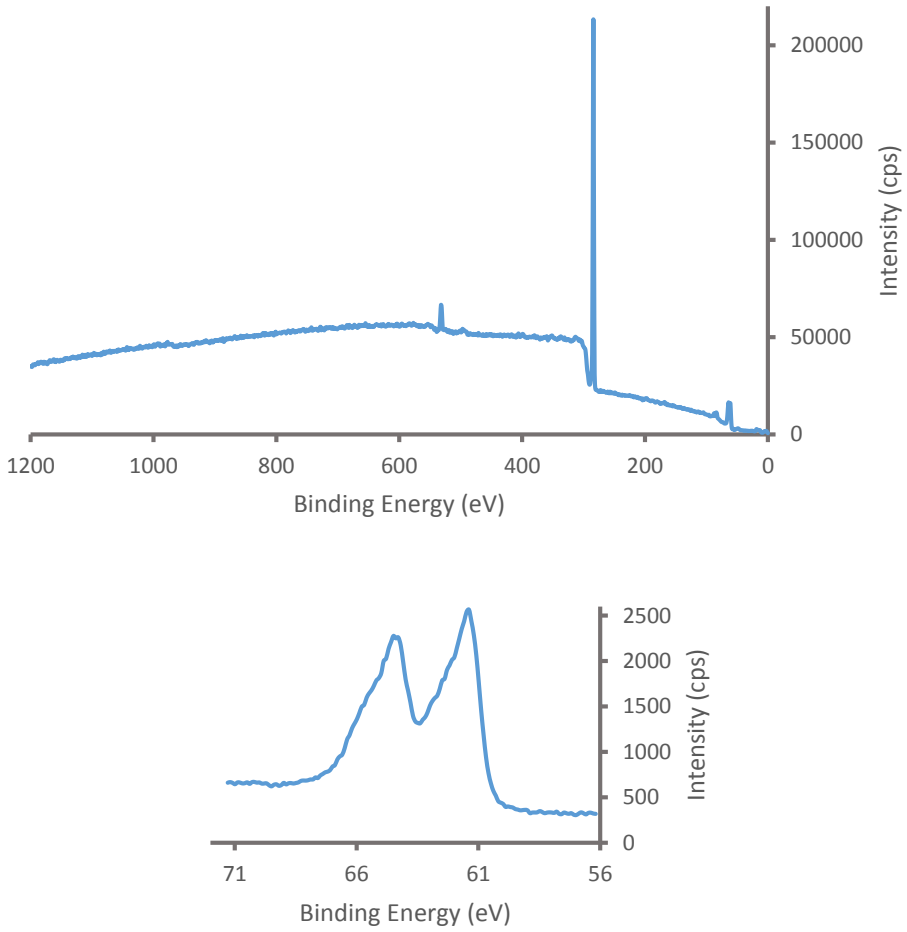

Figure 2.5 – XPS of A) as-synthesized IrO_2 nanoparticles. B shows a high resolution scan of the Ir 4f region.

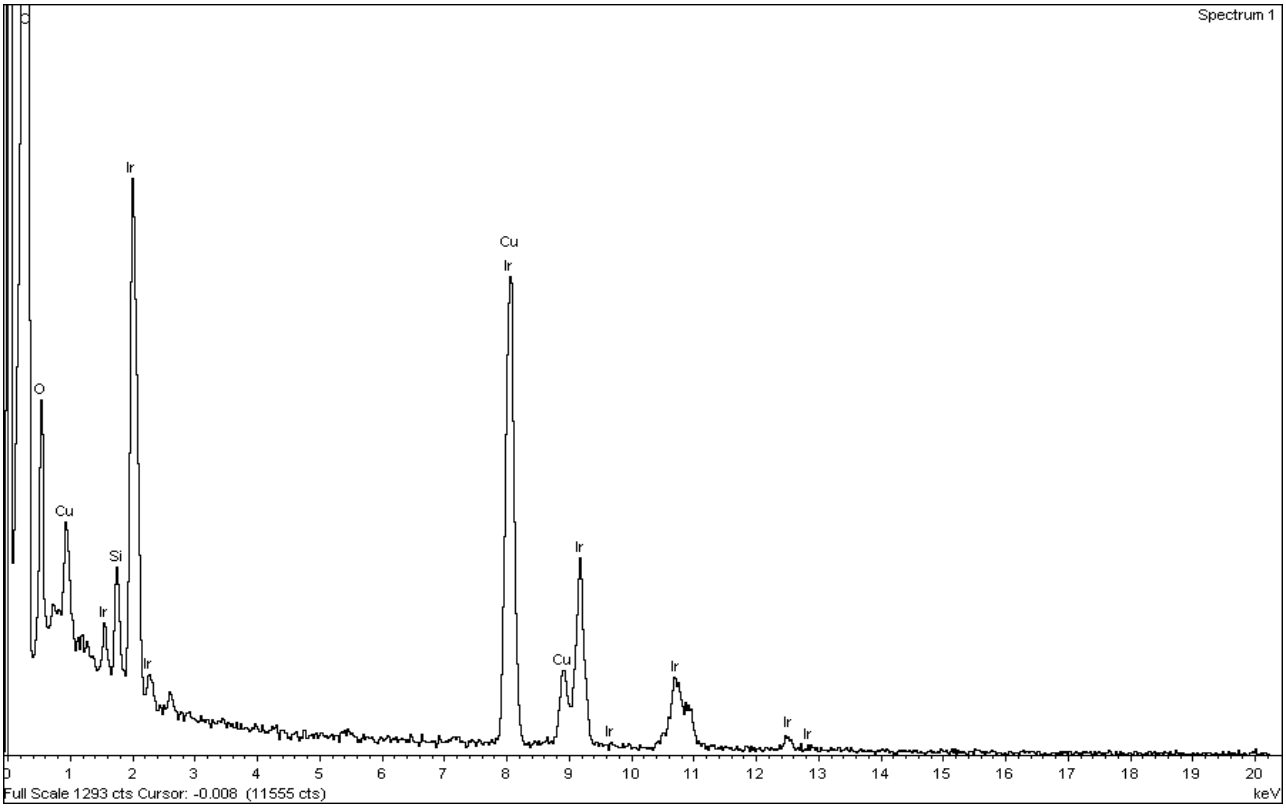

Figure 2.6 – EDX of the as-synthesized IrO_2 nanoparticles.

Table 2.2 – XPS and EDX Atomic Values for IrO_2

Sample Name	Method	Ir Atomic Percent (%)	Ir:O Ratio
IrO_2	XPS	0.85	0.24
	EDS	0.16	0.43

precipitated using ethanol, but did not disperse in non-polar solvents as expected. Instead, this nanomaterial formed a hazy suspension for ca. 2 hrs. before precipitating out of solution. This behavior suggests an incomplete protective surfactant shell, which might mean that the carboxylic acid and primary amine chosen (oleylamine and oleic acid) do not interact strongly with the crystalline planes of Bi_2S_3. TEM analysis of the suspension, as well as the unperturbed solution, showed two separate nanomaterials existed in the suspended (Fig 2.7a), small nanorods and large ca. 200 nm nanoparticles. For comparison, two additional procedures were attempted, 1) where sulfur was hot injected without oleylamine (SI-Bi_2S_3) and 2) a standard TD synthesis with sulfur added to the starting materials (Bi_2S_3). Hot injection of sulfur produced only the Bi_2S_3 nanorods seen previously in HI-Bi_2S_3 (Fig. 2.7b) while the standard TD synthesis produced a nanostructure hybrid somewhere between a cube and a sphere (Fig. 2.7c). UV-Vis spectra of the Bi_2S_3 nanoparticles (Fig 2.9) show very similar absorbance with a predominate shoulder at 235 nm and minor absorbance at 290, 415, and 660 nm. The similarity in spectra suggests that the structure of the material has little effect on the absorbance.

The Bi_2O_3 nanoparticles synthesized by the hot injection method proved to be anomalous compared to other MO_x nanoparticles made through this route. Instead of the small (<10 nm) nanoparticles typically observed, the Bi_2O_3 nanoparticles are 270 ± 190 nm in diameter (Fig 2.10a). These nanoparticles are similar to the large nanoparticles present in the HI-Bi_2S_3 TEM image suggesting that the large nanoparticles in that sample are likely Bi_2O_3 formed before the hot injection of elemental sulfur, resulting in both materials presence in the sample. The Bi_2O_3 nanoparticles also exhibited the same precipitation from non-polar solvents as the Bi_2S_3 samples. The lack of solubility coupled with the large nanoparticle size suggests minimal interaction with the capping ligands during synthesis. The ligands typically mediate nanoparticle

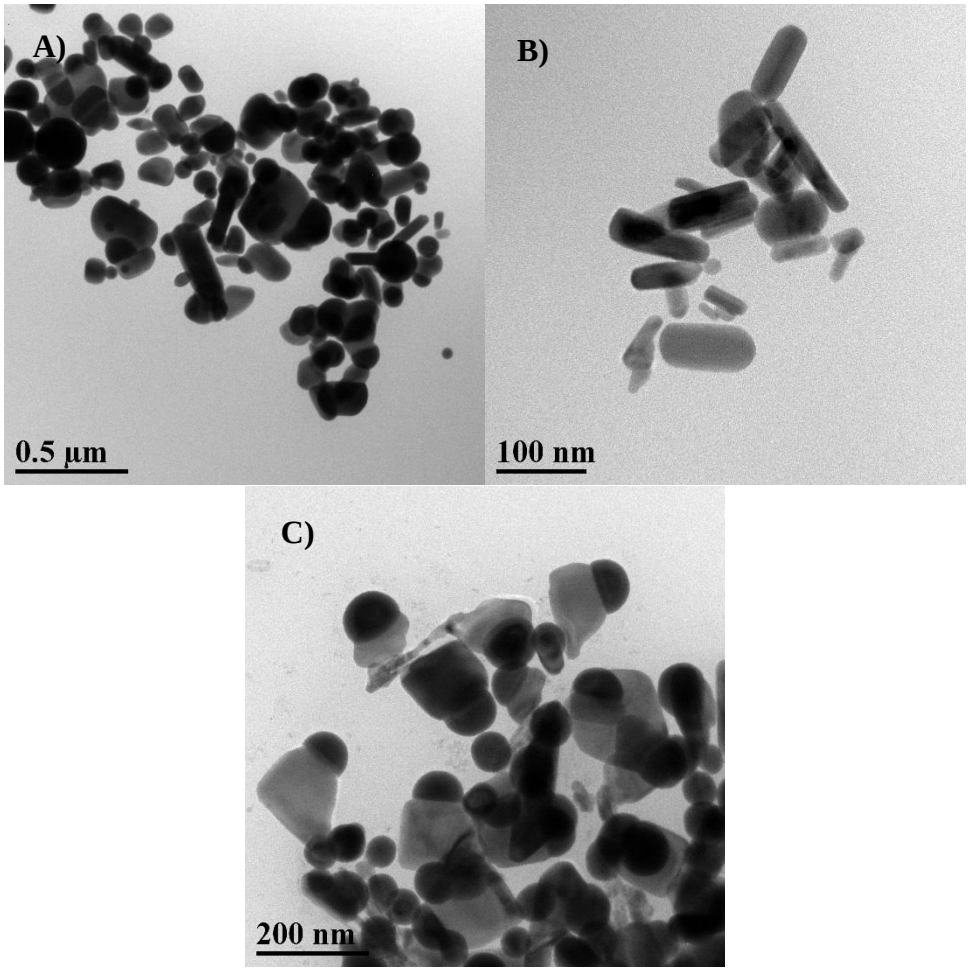

Figure 2.7 – TEM Images of Bi_2S_3 nanomaterials. A) shows HI- Bi_2S_3 (scale bar is 0.5 µm), B) shows SI- Bi_2S_3 Bi_2S_3 (scale bar is 100 nm) and C) shows Bi_2S_3 (scale bar is 200 nm).

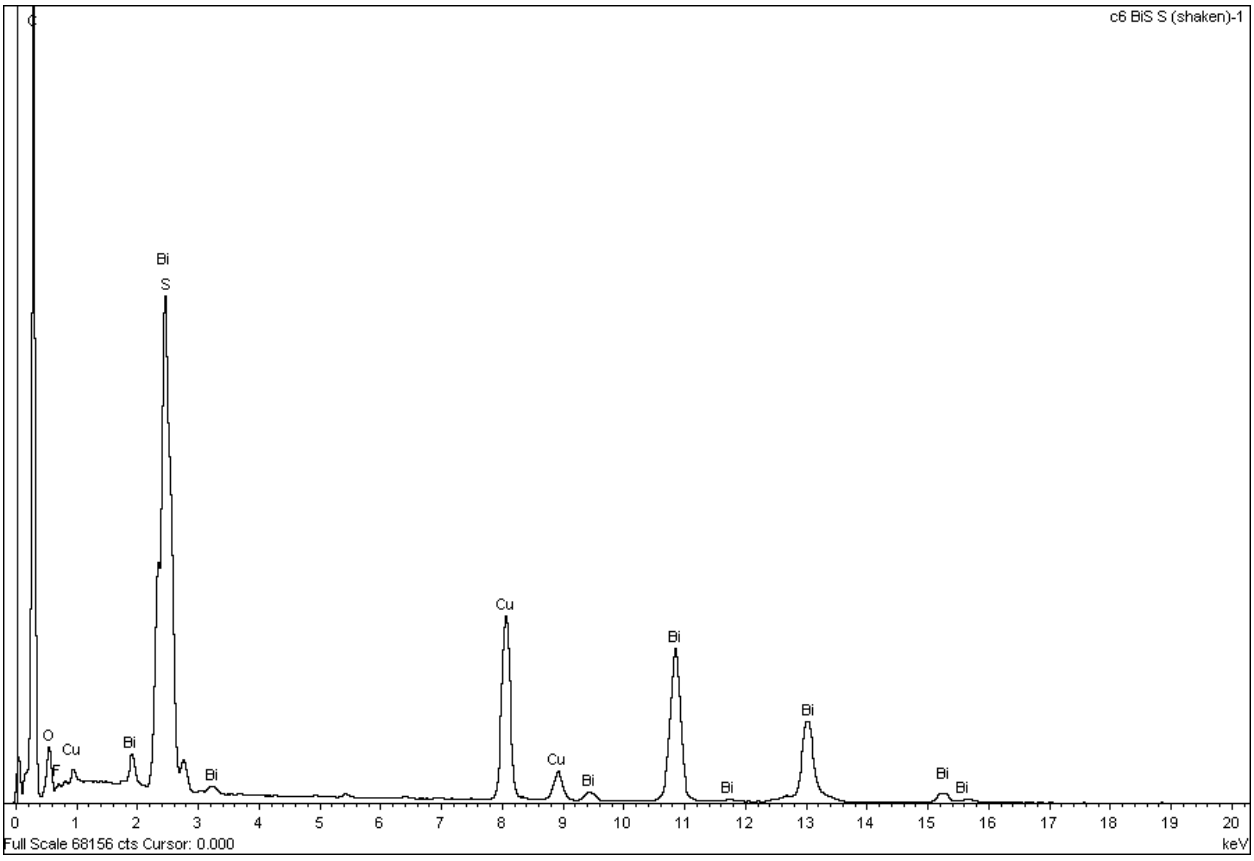

Figure 2.8 – EDX of Bi_2S_3 nanoparticles

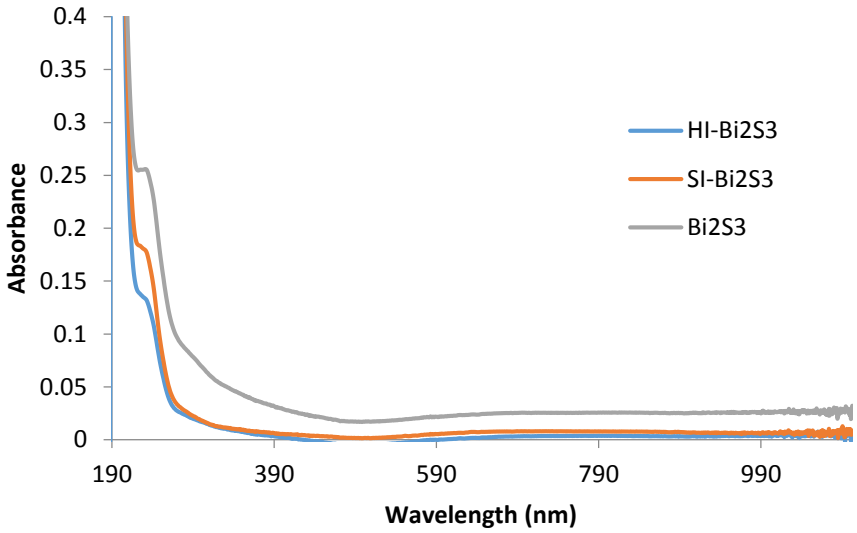

Figure 2.9 – UV-Vis spectrum a of 1 mg/mL Bi_2S_3 nanoparticle solution in hexanes.

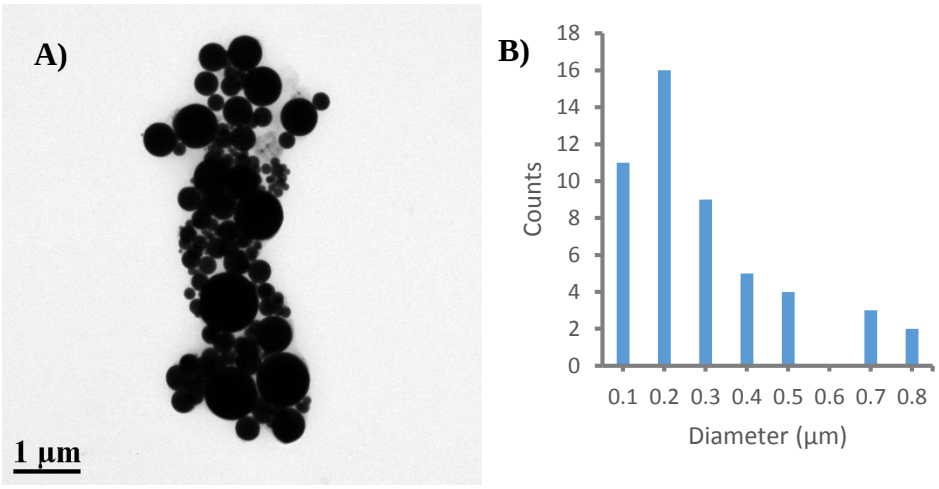

Figure 2.10 – TEM Images of Bi_2O_3 nanoparticles (290 ± 190 nm); panel A scale bar is 1 µm. B shows a histogram of the nanoparticle size dispersion.

growth by passivating one or more crystalline planes. Without passivation, the nanoparticle growth is limited only by the reaction time. XPS and EDX of the Bi_2O_3 nanoparticles disagree in this case. XPS shows very little Bi, even in the citrate capped sampled. The EDX shows substantial amounts of Bi, but very little oxygen yielding a Bi:O ratio of 16.5. Further investigation is needed to determine the composition of the "Bi_2O_3" nanoparticles.

2.3.4 Characterization of RuO_2 Nanoparticles Prepared by Thermal Degradation Synthesis

Attempts were made to synthesize Ru_2O_3 nanoparticles using Ru(III) acetylacetonate in the presence of oleylamine and oleic acid. During the reaction the solution turned from dark red to black, indicating a reaction had occurred. The reaction produced a material that was insoluble in ethanol, as would be expected for the surfactant capped nanoparticles. Analysis by TEM however, indicated no nanoparticles were present. The resultant nanoparticles were either too small to be resolved or unable to resolved due to the surfactant shell. No further analysis was attempted, but ruthenium was only metal acetylacetonate tested without evident nanoparticle formation.

2.3.5 Characterization of ITO Nanoparticles Prepared by Solvothermal Synthesis

Solvothermal ITO nanoparticles were synthesized in an effort to use their uncapped surface for more efficient surface modification (Chapter 3). Indium and tin aceylacetonates (6:1 mol ratio) were placed into benzyl alcohol and suspended before being transferred to a Teflon coated acid digestion bomb (this is step is frequently performed in a glove box under inert atmosphere). Argon was used to purge the vessel before placing it into the oven at 200 °C for 48 hours. The resulting nanoparticles were blue with an average diameter of 7.19 ± 1.42 nm (Fig. 2.13). While the TEM images show nanoparticles with excellent crystallinity, they lack any

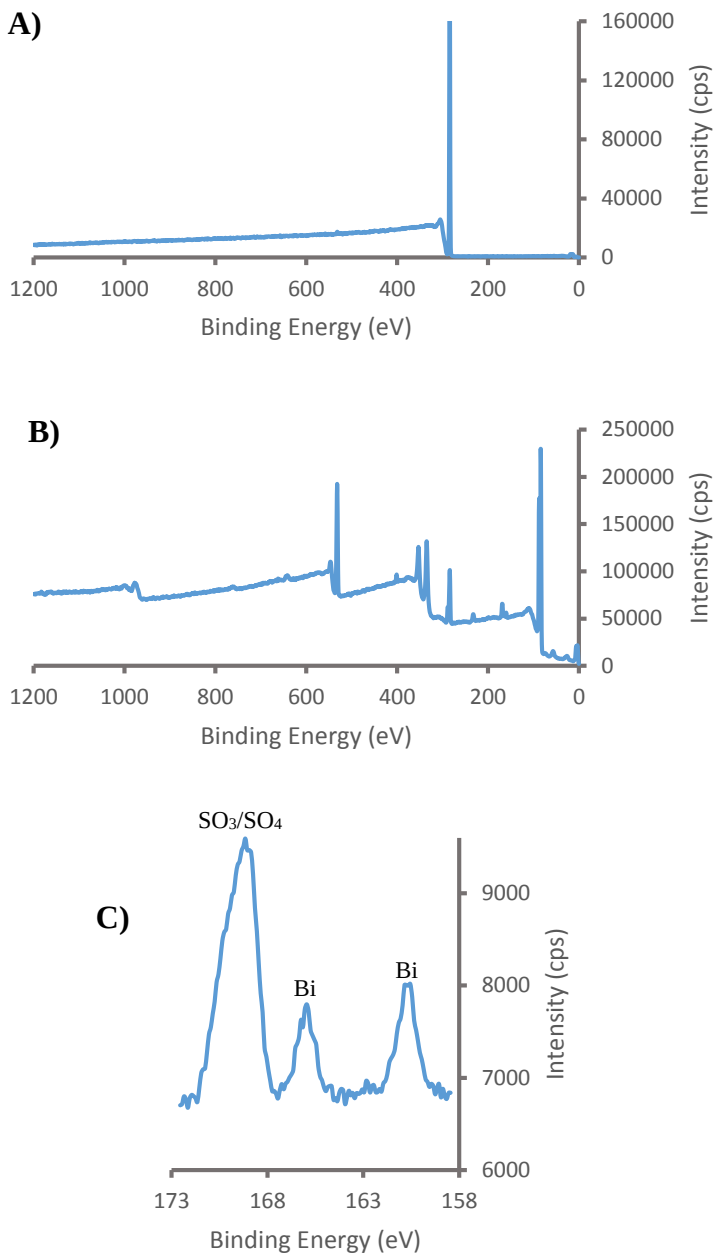

Figure 2.11 - XPS of A) Bi_2O_3 and B) cit-Bi_2O_3. C) depicts a high resolution scan of the S 2p and Bi 4f regions.

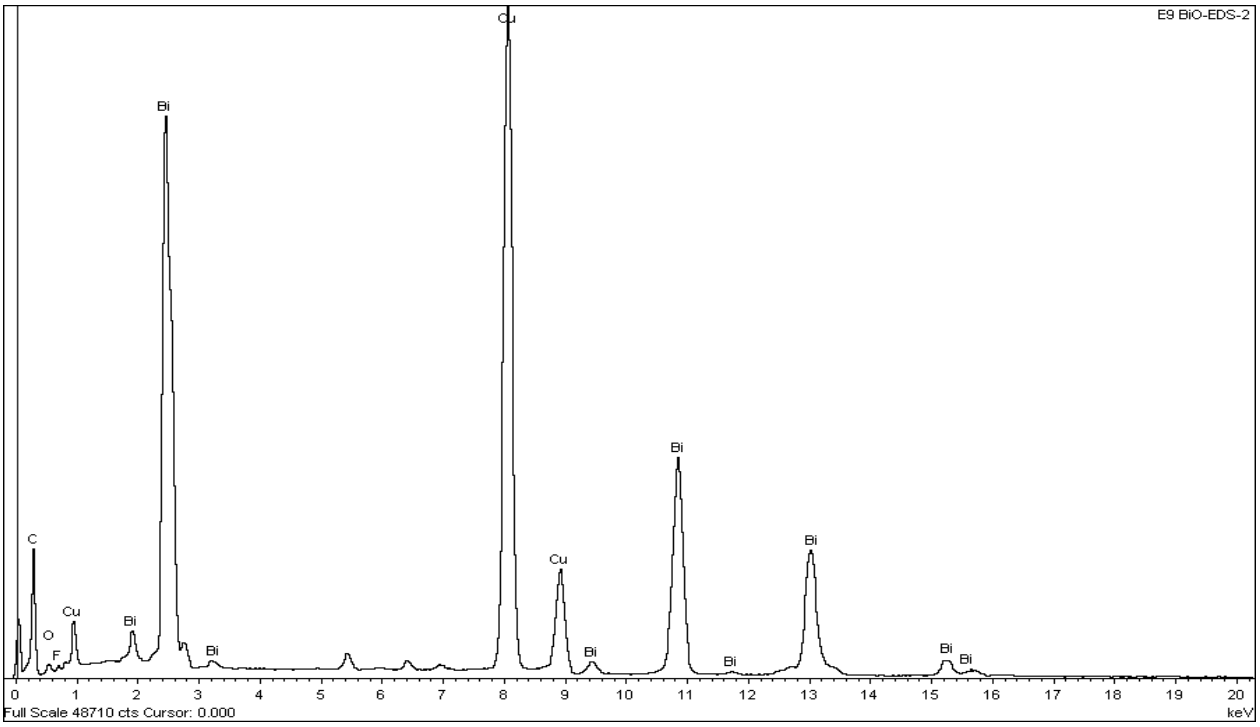

Figure 2.12 – EDX of Bi_2O_3 Nanoparticles

Table 2.3 – XPS and EDX Atomic Values for Bi_2O_3

Sample Name	Method	Ir Atomic Percent (%)	Bi:O Ratio
Bi_2O_3	XPS	0.00	-
	EDS	22.32	16.53
Cit- Bi_2O_3	XPS	0.13	0.004

type of controlled size distribution. Histograms for thermal degradation nanoparticles are Gaussian in nature, and the solvothermal distribution doesn't appear to have any pattern. The images also show large amounts of flocculation, which is expected due to the unprotected nature of their surfaces. Solubility further limits the utility of solvothermal ITO nanoparticles. The powder was insoluble in all commonly used laboratory solvents. In order to solubilize them, an additional surface molecule, like citric acid or octanoic acid, was required. Ultimately, solvothermal ITO did not offer enough advantages over the TD synthesis to make it worthwhile. The unpassivated surface was arguably more of hindrance than replacing the surfactant shell in TD. The reaction times were also substantially longer for nanoparticles with a poor size distribution and lower yield.

2.4 Conclusions

These results clearly show the power and versatility of the thermal degradation synthesis. All of the MO_x nanomaterials generated are currently undocumented in the literature and suggest that MO_x of almost any material can be generated assuming a metal aceylacetone is commercially available. The TD nanoparticles also displayed a tight size distribution, compared to those generated through solvothermal routes. ZrO_2 nanoparticles were further characterized by surface modification (Chapter 4). Altering the capping ligands in the Bi_2S_3 and Bi_2O_3 systems could ascertain more about ligand-surface interactions with regards to regulating nanoparticle size. Additional studies with $Ru(acac)_3$ might also provide insight into synthetic limitations of the TD route.

2.5 Acknowledgments

This research was supported in part by the Office of Naval Research and the National Science Foundation. We gratefully acknowledge TEM, EDX, and XPS measurements

performed by Carrie Donley and Amar Kumbhar of the Analytical and Nanofabrication Laboratory of the UNC Institute for Advanced Materials.

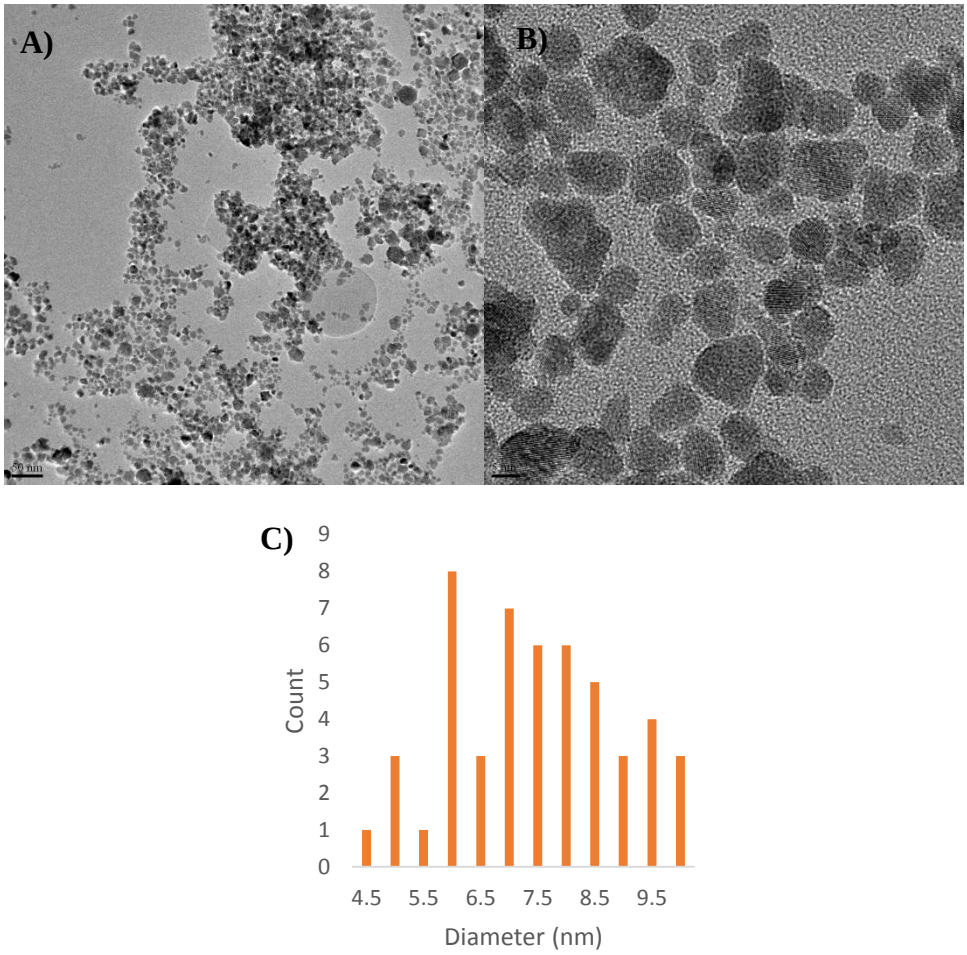

Figure 2.13 – TEM of solvothermal ITO nanoparticles (7.19 ± 1.42 nm); panels A and B scale bars are 50 nm and 5 nm, respectively. C shows a histogram of the nanoparticle size dispersion.

2.6 References

1. Thomas, P. J.; Stansfield, G. L.; Vanitha, P. V., Nanoparticles. *Annual Reports Section "A" (Inorganic Chemistry)* **2011,** *107* (0), 505-518.

2. Sardar, R.; Funston, A. M.; Mulvaney, P.; Murray, R. W., Gold Nanoparticles: Past, Present, and Future†. *Langmuir* **2009,** *25* (24), 13840-13851.

3. Zhang, Z.; Lu, M.; Xu, H.; Chin, W.-S., Shape-Controlled Synthesis of Zinc Oxide: A Simple Method for the Preparation of Metal Oxide Nanocrystals in Non-aqueous Medium. *Chemistry – A European Journal* **2007,** *13* (2), 632-638.

4. Sun, S.; Zeng, H.; Robinson, D. B.; Raoux, S.; Rice, P. M.; Wang, S. X.; Li, G., Monodisperse MFe2O4 (M = Fe, Co, Mn) Nanoparticles. *J. Am. Chem. Soc.* **2003,** *126* (1), 273-279.

5. Sun, Z.; He, J.; Kumbhar, A.; Fang, J., Nonaqueous Synthesis and Photoluminescence of ITO Nanoparticles. *Langmuir* **2010,** *26* (6), 4246-4250.

6. Gilstrap Jr, R. A.; Summers, C. J., Synthesis and analysis of an indium tin oxide nanoparticle dispersion. *Thin Solid Films* **2009,** *518* (4), 1136-1139.

7. Zhen, G.; Muir, B. W.; Moffat, B. A.; Harbour, P.; Murray, K. S.; Moubaraki, B.; Suzuki, K.; Madsen, I.; Agron-Olshina, N.; Waddington, L.; Mulvaney, P.; Hartley, P. G., Comparative Study of the Magnetic Behavior of Spherical and Cubic Superparamagnetic Iron Oxide Nanoparticles. *The Journal of Physical Chemistry C* **2010,** *115* (2), 327-334.

8. Charles, J. C.; Ilia, N. I.; Salil, J.; Rosario, A. G., The effect of the atmosphere on the optical properties of as-synthesized colloidal indium tin oxide. *Nanotechnology* **2009,** *20* (14), 145701.

9. Sasaki, T.; Endo, Y.; Nakaya, M.; Kanie, K.; Nagatomi, A.; Tanoue, K.; Nakamura, R.; Muramatsu, A., One-step solvothermal synthesis of cubic-shaped ITO nanoparticles precisely controlled in size and shape and their electrical resistivity. *J. Mater. Chem.* **2010,** *20* (37), 8153-8157.

10. Neri, G.; Bonavita, A.; Micali, G.; Rizzo, G.; Pinna, N.; Niederberger, M.; Ba, J., Effect of the chemical composition on the sensing properties of In2O3–SnO2 nanoparticles synthesized by a non-aqueous method. *Sensors and Actuators B: Chemical* **2008,** *130* (1), 222-230.

11. Ba, J.; Feldhoff, A.; Fattakhova Rohlfing, D.; Wark, M.; Antonietti, M.; Niederberger, M., Crystallization of Indium Tin Oxide Nanoparticles: From Cooperative Behavior to Individuality. *Small* **2007,** *3* (2), 310-317.

12. Ba, J.; Fattakhova Rohlfing, D.; Feldhoff, A.; Brezesinski, T.; Djerdj, I.; Wark, M.; Niederberger, M., Nonaqueous Synthesis of Uniform Indium Tin Oxide Nanocrystals and Their Electrical Conductivity in Dependence of the Tin Oxide Concentration. *Chem. Mater.* **2006,** *18* (12), 2848-2854.

13. Campelj, S.; Makovec, D.; Drofenik, M., Preparation and properties of water-based magnetic fluids. *J. Phys.: Condens. Matter* **2008,** *20* (20), 204101.

14. Bechepeche, A. P.; Treu, O., Jr.; Longo, E.; Paiva-Santos, C. O.; Varela, J. A., Experimental and theoretical aspects of the stabilization of zirconia. *Journal of Materials Science* **1999,** *34* (11), 2751-2756.

15. Bestaoui, N.; Prouzet, E.; Deniard, P.; Brec, R., Structural and analytical characterization of an iridium oxide thin layer. *Thin Solid Films* **1993,** *235* (1–2), 35-42.

16. Koyama, E.; Nakai, I.; Nagashima, K., Crystal chemistry of oxide-chalcogenides. II. Synthesis and crystal structure of the first bismuth oxide-sulfide, Bi2O2S. *Acta Crystallographica Section B* **1984,** *40* (2), 105-109.

17. Sliem, M. A.; Schmidt, D. A.; Bétard, A.; Kalidindi, S. B.; Gross, S.; Havenith, M.; Devi, A.; Fischer, R. A., Surfactant-Induced Nonhydrolytic Synthesis of Phase-Pure ZrO2 Nanoparticles from Metal–Organic and Oxocluster Precursors. *Chem. Mater.* **2012,** *24* (22), 4274-4282.

18. Wöhler, L.; Witzmann, W., Die Oxyde des Iridiums. *Zeitschrift für anorganische Chemie* **1908,** *57* (1), 323-352.

CHAPTER 3 – SYNTHESIS AND ELECTROCHEMISTRY OF 6 NM FERROCENATED INDIUM TIN OXIDE NANOPARTICLES

(This chapter is adapted with permission from Roberts, J. J. P; Vuong K. T.; Murray, R. W. *Langmuir* **2013**, 29, 474. Copyright 2013 American Chemical Society.)

3.1 Introduction

Being both optically transmissive and electrically conductive, the n-type semiconductor indium tin oxide (ITO) has substantial industrial utility in flat panel display technology[1], solar cell windows[2], gas sensing devices[3], and transparent electrodes[4]. Methods for generating bulk ITO materials tend to require specialized instrumentation and are subject to variability of produced materials. Preparation of ITO in nanoparticle forms and spreading as films followed by sintering provides a less expensive route while retaining desired conductive and optical characteristics[5]. Modern synthetic methods can produce crystalline ITO nanoparticles with well-defined morphologies and narrow size distributions[6-8]. One synthesis involves decomposition of indium and tin precursors (commonly as acetates or acetylacetonate complexes) in a high boiling point solvent (at *ca*. 300˚ C) in the presence of fatty amine and carboxylic acid surfactants[9]. Nanoparticles are formed in which tin atoms are substituted for indium sites in the cubic bixbyte structure of In_2O_3. Thusly prepared ITO nanoparticles can be formed as films by dip coating or spin coating, followed by sintering. The films can be tuned by controlling the capping surfactant and its concentration in solution[10].

This chapter reports the synthesis of small (6 nm diameter) indium tin oxide (ITO) nanoparticles capped with a redox active species (ferrocene). Rather than ITO film preparation, the goal is to create ITO nanoparticles having ferrocenated surfaces (abbrev. as FcITO) and to

examine their electrochemical behavior as diffusing nanoparticle species, including assessing the nanoparticles' ferrocene surface coverage. Very small nanoparticles are desired, in the interest of solution solubility. ITO surfaces, like those of many metal oxides, are known to react with chloro- and alkoxysilanes[11]. Here, reaction with an excess of the monoalkoxysilane 3-aminopropyldimethylethoxysilane (APTMES) is calculated to displace the original capping surfactants from the surfaces of prepared ITO nanoparticles. The amine-terminated silanized nanoparticle surface provides a platform for an amide-coupling reaction with ferrocenoyl chloride. The study provides a further example[12] of redox-labeled nanoparticle electrochemical behavior, of assessment of the surface coverage of redox labels, and is part of an on-going exploration of electroactive nanoparticle materials[13] as components of electrochemical charge storage systems.

3.2 Experimental

3.2.1 Chemicals and Materials

. Indium(III) acetate ($In(ac)_3$; 99.99%), tin(II) (acetate) ($Sn(ac)_2$; 99.99%) were obtained from Alfa Aeser, oleylamine ($C_9H_{18}=C_9H_{17}NH_2$; 80-90%), oleic acid ($C_9H_{18}=C_8H_{15}COOH$; 97%), octadecene ($C_{16}H_{33}=CH_2$; 90%), ferrocene carboxylic acid (97%), oxalyl chloride (98%), imidazole (>99%), pyridine (> 99.0%), triethylamine (>99%) and copper(II) perchlorate hexahydrate (98%) from Sigma-Aldrich, and tetrabutylammonium perchlorate (Bu_4NClO_4) from Fisher Scientific. Acetonitrile (CH_3CN), absolute ethanol, hexanes, dichloromethane (DCM), petroleum ether, toluene, and chloroform obtained from Fisher Scientific were dried over 4 Angstrom molecular sieves. The functionalized silane, 3-aminopropyldimethylethoxysilane

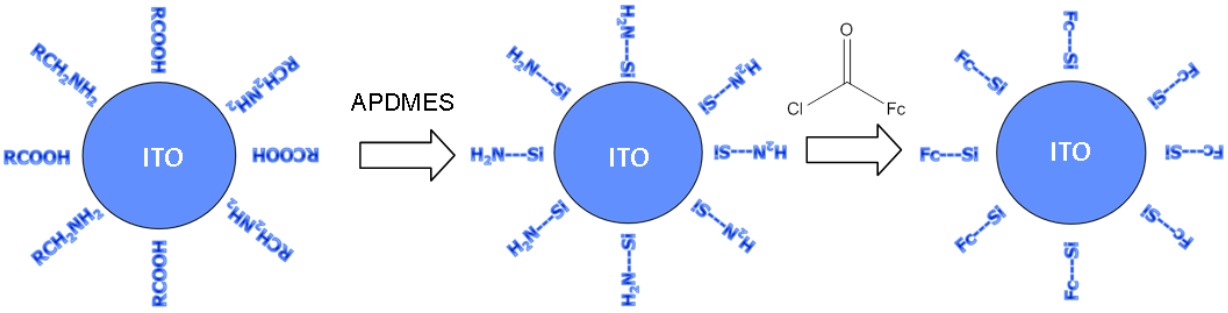

Scheme 3.1 - The as-synthesized ITO nanoparticles are covalently reacted with APDMES to displace the initial surfactants and to aminate the nanoparticle surfaces. Ferrocenoyl chloride then reacts with the primary amine.

(APTMES), was obtained from Gelest, Inc. (Morrisville, PA) and stored refrigerated. Use of a monoalkoxy reagent was calculated to avoid polymeric siloxane layer formation.

3.2.2 Instrumentation and Electrochemical Details

Cyclic Voltammetry (CV). CV was performed on a CH Instruments (CHI) 660a potentiostat with Pt working electrode (area 0.02 cm^2), Pt mesh counter electrode, and Ag/AgCl/3 M KCl (aq) reference electrode in acetonitrile solutions with 0.1 M tetrabutylammonium perchlorate electrolyte.

Programmable Temperature Control Unit. A lab constructed device controlled by a CAL 9500P programmable process controller with attached to a thermal couple was used to accurately control synthesis temperatures.

High Resolution Transmission Electron Microscopy (TEM). TEM images were obtained on a JEOL 2010F FasTEM on nanoparticle samples prepared on copper grids (200 carbon mesh, carbon-coated Formvar; Ted Pella, Redding, CA)

Energy-Dispersive X-Ray Spectroscopy (EDS). EDS analysis was performed using Oxford INCA EnergyTEM 250 TEM microanalysis system attached to the JEOL 2010F FasTEM.

Centrifuge. Centrifugation was done with an Eppendorf 5810 centrifuge with a fixed-angle rotator at 3000-4000 rpm for 10 minutes.

X-Ray Photoelectric Spectroscopy (XPS). XPS data were taken on a Kratos Axis Ultra DLD system with monochromatic Al Kα x-ray source. High resolution scans were taken at pass energy = 20 eV, and the spectral energy axis was aligned at the C 1s peak at 284.6 eV.

Ultraviolet-Visible Spectroscopy (UV-Vis). UV-Vis spectra were taken on a Thermo Evolution Array UV-Vis spectrophotometer (Thermo, Waltham, MA)

3.2.3 Synthesis of 6 nm Indium Tin Oxide Nanoparticles .

The procedure was modified from Sun *et al*[8]. $In(acac)_3$ (0.20 mmol), $Sn(acac)_2Cl_2$ (0.02 mmol), and 0.60 mL oleic acid (1.9 mmol) were added to octadecene (5 mL) in a 50 mL 3-neck round bottom flask equipped with a magnetic stir bar, thermocouple and condenser, closing the third port with a septum. Using a 100 mL heating mantle packed with sand to promote even heating, the vessel was evacuated and heated 1 hr at 120˚ C with vigorous stirring. The temperature was then rapidly increased to 295˚ C at which point 0.80 mL oleylamine (2.4 mmol) in 0.2 mL octadecene was injected via syringe. The solution color changed from bright orange to murky green, signaling formation of ITO nanoparticles. The reaction was refluxed at 320˚ C for an hour, and allowed to cool to room temperature. The cloudy blue-green suspension was transferred to a 50 mL centrifugation tube and 40 mL of absolute ethanol added, precipitating the nanoparticles, followed by centrifugation at 3000 RPM for 10 minutes. This process was repeated three times. The nanoparticles were then taken up into 3 mL of either hexanes or chloroform and stored at room temperature. The solution ranged from dark blue to green and the nanoparticles produced had average dia. 6.1 ± 0.8 nm. Figure 1 shows TEM images.

3.2.4 Silane-Capped ITO Nanoparticles.

A 1 mL hexane solution of nanoparticles was rotovapped to dryness, the nanoparticles were weighed and redissolved in 4 mL toluene in a scintillation vial. APTMES was added in 10-fold excess (relative to estimated total nanoparticle surface area), which was ~0.03 g per 0.1 g nanoparticles. 0.05 g (0.75 mmol) of imidazole was added as catalyst and the solution, which became a turbid blue, was stirred vigorously at room temperature for 1 hr. The solution was

transferred to a 15 mL centrifuge tube and centrifuged at 4000 RPM for 10 minutes. The aminated nanoparticles were washed twice more with fresh toluene and then dispersed in 3 mL of toluene for storage.

3.2.5 Synthesis of Ferrocenoyl Chloride and of Ferrocene-Functionalized ITO Nanoparticles.

0.23 g of ferrocene carboxylic acid (1.00 mmol) was suspended in 4 mL of petroleum ether in a 25 mL round bottom flask. 2 drops of pyridine were added followed by slow addition of 100 μL oxalyl chloride (1.20 mmol); the solution bubbled and gassed upon this addition. The reaction solution was stirred under Ar for 1.5 hrs, and the petroleum ether and excess oxalyl chloride removed by pumping under vacuum (ca. 2 hr). The red-orange solid was collected in CH_2Cl_2 and placed into a 15 mL centrifuge tube and centrifuged at 4000 RPM for 10 minutes to separate the unreacted FcCOOH from the FcCOOCl. The bright red product solution was decanted and immediately reacted with silane capped ITO nanoparticles.

The 3 mL solution of silane capped ITO nanoparticles in toluene plus 50 μL triethylamine (to aid activation of the acid chloride) was reacted for 1 hr. in a scintillation vial with 100 μL of the ferrocenoyl chloride solution and then transferred to a 15 mL centrifuge tube and centrifuged at 4000 RPM for 10 minutes. The blue-brown precipitate was washed twice more with 5 mL toluene, then dissolved in 3 mL of acetonitrile and stored at room temperature.

3.3 Results and Discussion

3.3.1 ITO Synthesis.

The ITO nanoparticle synthesis was modified from Sun *et al.*[8] Rather than heating the reaction mixture with all reagents present, the oleylamine, which activates the nanoparticle formation, was hot injected at 25 ˚C below the solvent boiling point. This modification, along

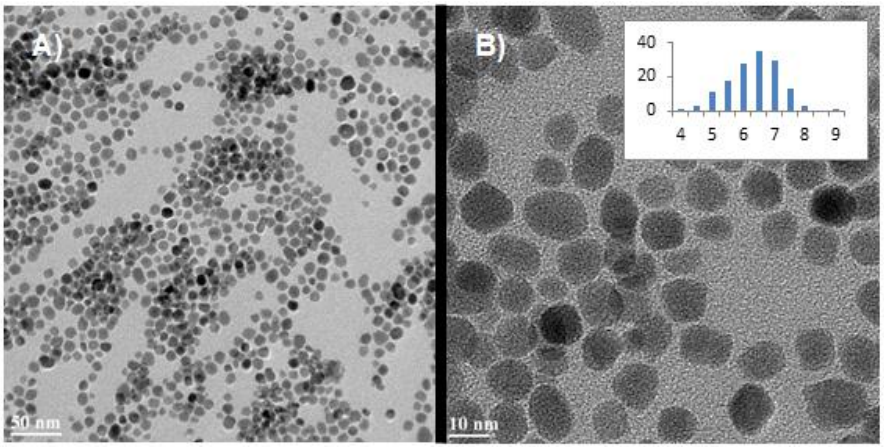

Figure 3.1 - TEM Images of ITO nanoparticles (6.1 ± 0.8 nm); panels A and B scale bars are 50 nm and 10 nm, respectively. The inset shows a histogram of the nanoparticle size dispersion.

with maintaining accurate temperature control, substantially improved reproducibility of synthetic nanoparticle batches. The color of the as-synthesized ITO nanoparticle solutions range from dark blue to vivid green, after *ca*. 24 hr shifting towards blue, or teal, and is blue after the silanization step. It is suggested that the color changes reflect the slow equilibration of Sn^{IV} sites with interstitial oxygen. The ITO nanoparticles are by TEM (Fig. 3.1) reasonably monodisperse, with little aggregation. The nanoparticle diameter, from TEM images of multiple synthetic batches, averages 6.1±0.8 nm.

3.3.2 Replacement of Surfactants with Silane Ligands and Ferrocenation.

Aiming at gaining control of the ITO nanoparticle surface chemistry, the original capping ligands on the synthesized ITO nanoparticles were displaced by silanization of the ITO surface. Silanization of macroscopic ITO surfaces is a known reaction[14] and can be anticipated for ITO nanoparticle surfaces. The goal was to form an aminated, functionalized nanoparticle surface for reaction with ferrocenoyl chloride. (Electroactive ligands have been previously attached to Au and SiO_2 nanoparticles[12, 15] by this laboratory.) A monodentate alkoxysilane reagent was selected to avoid formation of silane polymer on the nanoparticles. After some experimentation, the silanization reaction was carried out at room temperature for ~ 1 hr, with little flocculation being noticed by TEM imaging. (Test silanizations for longer periods (12-24 hrs) and at elevated temperatures (~80˚ C) tended to provoke nanoparticle aggregation.)

The silanized ITO nanoparticles would usually remain dispersed in toluene for about a week (in some cases some precipitation then commenced). Variability of solubility probably reflects incomplete displacement of the original surfactant. The nanoparticles could be isolated from toluene by centrifugation. Nanoparticle surface composition was monitored with XPS (Fig 3.2b). Post-silanization, indium 3d peaks are seen at 444.5 and 451.5 eV, and tin 3d peaks at

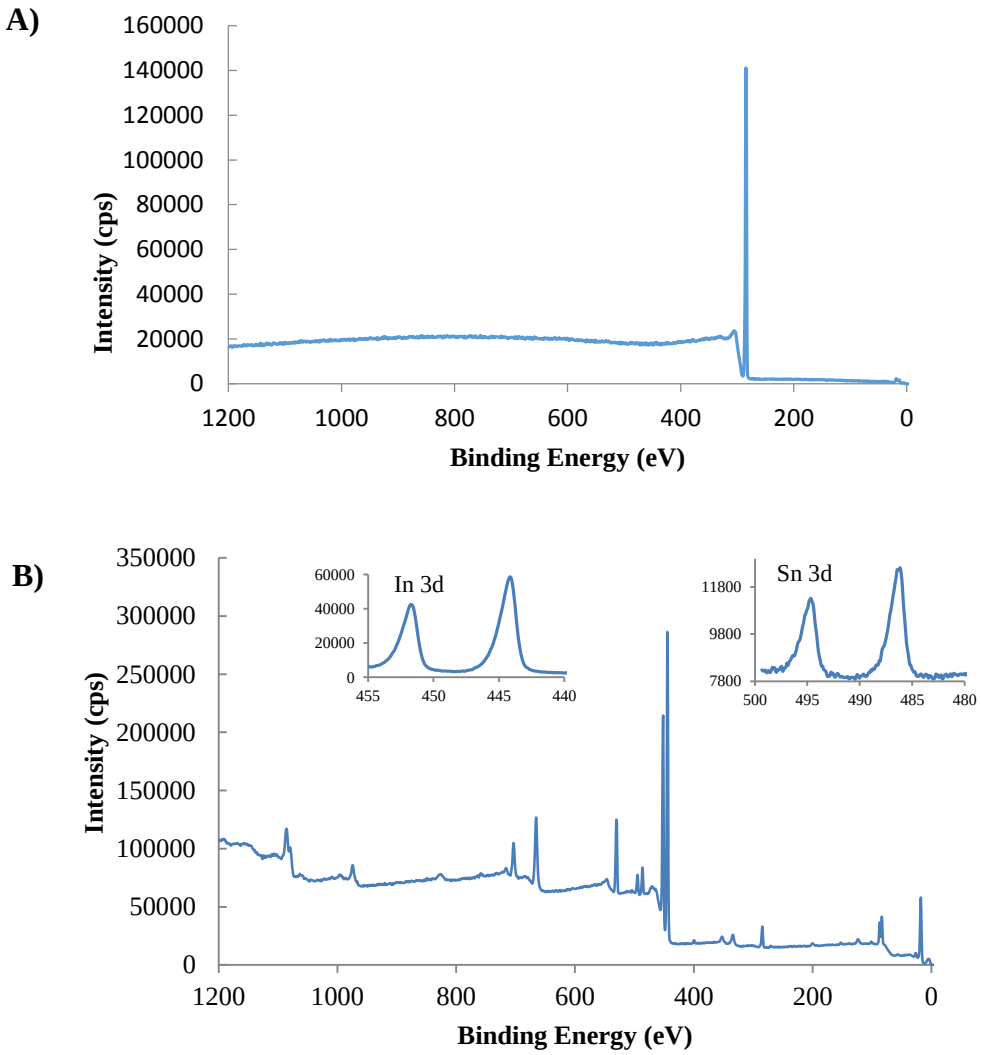

Figure 3.2 – XPS spectrum of ITO nanoparticles A) as synthesized and B) after silanization. Insets depict In 3d and Sn 3d regions

486 and 494.5 eV. Before silanization, these peaks are masked by scattering of photoelectrons by the nanoparticle capping ligands (Fig. 3.2a), which produces the large C 1s peak. Post-silanization, the C 1s peak is greatly diminished and indium and tin peaks can be seen, as are low intensity Si 2p, Si 2s, and N 1s peaks.

Following silanization, a measured mass of the aminated ITO nanoparticles is reacted with ferrocenoyl chloride. In this procedure and in subsequent washing steps, considerable loss of product occurs in the centrifugal isolation. At least two wash steps were necessary to remove unattached ferrocene reagent, whose presence would interfere in the subsequent electrochemistry studies. TEM imaging shows that the average core diameters of the ferrocenated ITO nanoparticles (abbrev. FcITO) are substantially unchanged from the as-synthesized ITO nanoparticles (Fig. 3.1). (The lower atomic weight ferrocene substituents are not expected to contribute significantly to the image diameter.) Assuming complete nanoparticle surface coverage by the amine silane reagent, its complete coupling with ferrocenoyl chloride, and a ferrocene surface footprint of 1 nm^2, the typical 0.006 g mass of isolated FcITO nanoparticle product in a 3 ml acetonitrile solution ideally corresponds to an overall *ca*. 5 mM ferrocene concentration.

The actual reactive ferrocene concentration in 1 mL of the ITO nanoparticle solution was assessed by a potentiometric titration (Fig 3.3) with Cu^{2+}, which in acetonitrile is an effective ferrocene oxidant[16-17]. During the titration, the nanoparticle solution color changes from light blue-brown to yellow. This coloration is due to the combination of the ITO nanoparticles and the ferrocene attached to the surface. Multiple trials give indicate an overall ferrocene concentration of 1.3 ± 0.2 mM. Based on the model coverage calculation above, the actual ferrocene coverage of the ITO surface is about 25%.

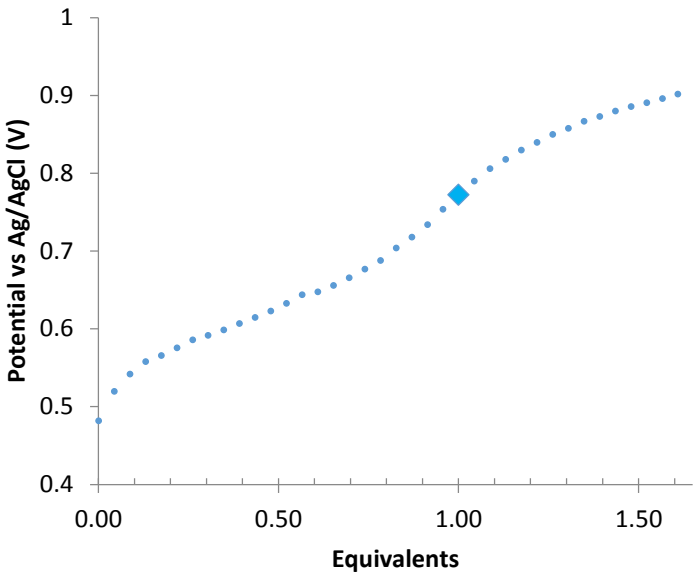

Figure 3.3 - Potentiometric titration of a 1 mL CH_3CN solution of ferrocenated ITO nanoparticles with 1.18 mM $Cu(ClO_4)_2$ CH_3CN solution. The equivalence point is marked with a diamond; titration volume is 1.15 mL

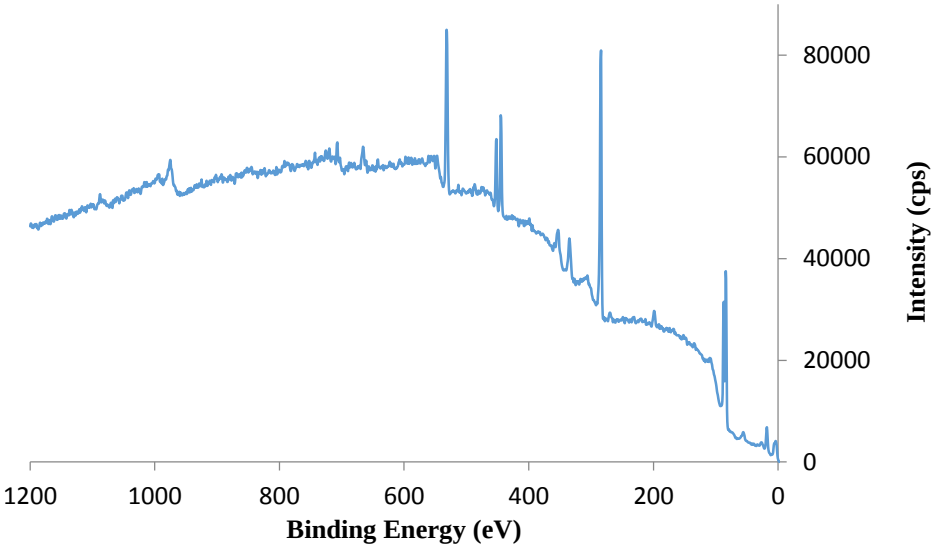

Figure 3.4 - XPS spectrum of ITO nanoparticles after silanization and reaction with ferrocene acid chloride.

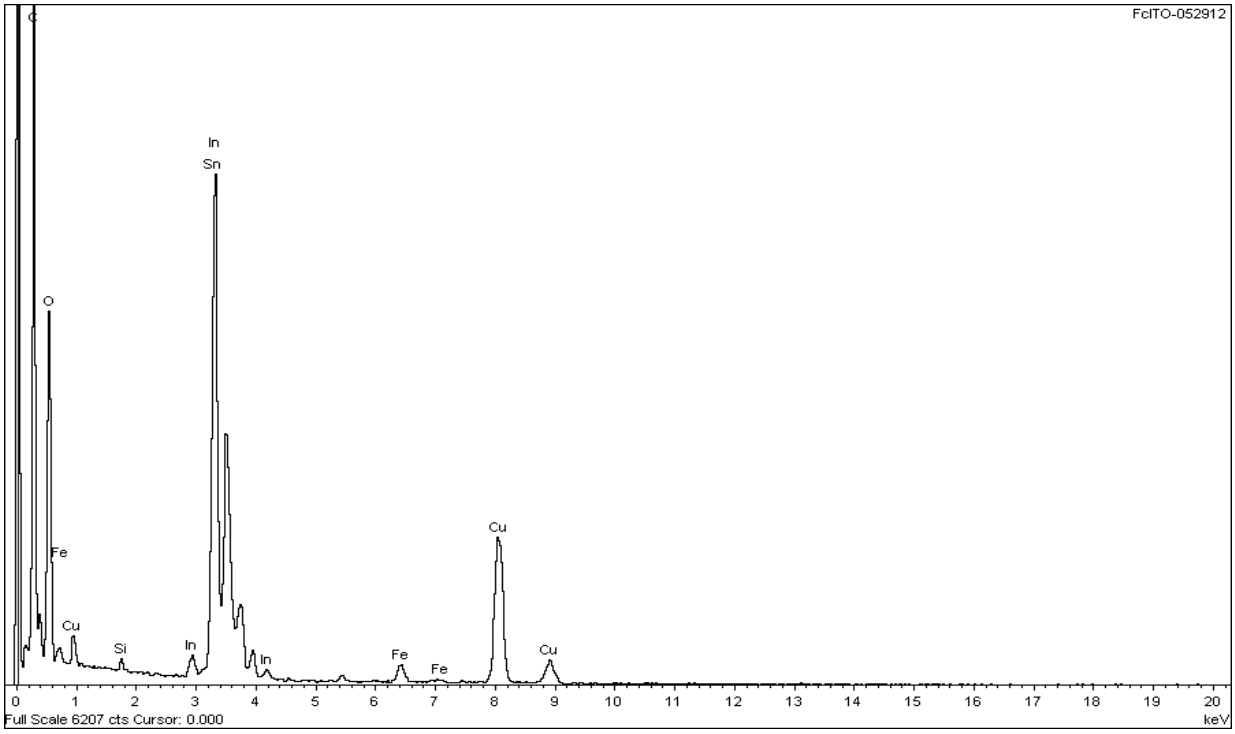

Figure 3.5 - EDX of ferrocenated ITO nanoparticles.

The ferrocenated (FcITO) nanoparticles were stably soluble in acetonitrile, which was chosen for the electrochemical experiments. (Before ferrocenation, the ITO nanoparticles are insoluble in acetonitrile.) The presence of iron on the FcITO nanoparticles was confirmed by XPS (Fig. 3.4) and EDX (Figure 3.5). The observed N/Fe peak ratio (with normalization for elemental sensitivity) was *ca*. 1:0.5, differing from the ideal 1:1 for the ferrocene amide grouping. This result is consistent with the above indication of non-exhaustive coupling between the amine sites and the ferrocenoyl chloride.

3.3.3 Voltammetry of Ferrocenated ITO Nanoparticles.

Voltammetry of the FcITO nanoparticles was carried out in 0.1 M Bu_4NClO_4/acetonitrile solutions. The ferrocene wave was readily seen in cyclic voltammetry (Figure 3.6) although the currents were modest due to the low concentration and slowed nanoparticle diffusion rates. Measurement of the nanoparticle diffusion coefficient (D) was set as a target in quantifying the electrochemical assessment, using cyclic voltammetry, chronoamperometry, and microdisk electrode voltammetry.

The diffusion coefficient expected was estimated using the no-slip version of the Stokes-Einstein equation, which is

$$D = \frac{kT}{6\pi\eta r} \qquad (1)$$

where r is nanoparticle hydrodynamic radius and η is acetonitrile viscosity (0.343 cP). Based on the 6.1 nm TEM nanoparticle core diameter and plus a 2 nm increment for the ferrocene sites, this equation predicts a FcITO nanoparticle diffusion coefficient of $D = 2.1 \times 10^{-6}$ cm^2/s. Previous measurements of diffusion coefficients of organothiolate coated Au nanoparticles (1-5 nm diameter), using the classical Taylor Dispersion method[18], show that a) Equation (1) can

predict nanoparticle diffusion coefficients to within a factor of *ca*. two and b) that the organothiolate monolayer on the nanoparticles may be partially free-draining.

Cyclic voltammetry of the amide-connected ferrocene on the FcITO nanoparticles shows a one electron chemically reversible wave with formal potential *ca*. 0.46 mV *vs*. Ag/AgCl(aq) (Fig. 3.6). The Randles-Sevcik equation for linear sweep voltammetry[19] is

$$i_p = 2.69 * 10^5 \, n^{3/2} A D^{1/2} C v^{1/2} \qquad (2)$$

where n is the number of electrons delivered (per ferrocene), D (cm^2/s) is nanoparticle diffusion coefficient and C (mol/cm^3) is the concentration of reactive ferrocene. Figure 3.7 shows that the peak currents do not follow the expected $v^{1/2}$ potential scan rate dependency, but show a non-zero intercept and curve upward in a manner suggesting adsorption of the ferrocenated nanoparticles on the electrode. Note the lessening of ΔE_{PEAK} at the fastest scan rate in Figure 3.6, which is consistent with this conclusion. We therefore elected not to employ linear sweep current results in estimates of the nanoparticle diffusion coefficient.

Currents from potential step chronoamperometry and from microelectrode voltammetry should be relatively little affected by a modest extent of nanoparticle adsorption. These two experiments yield nanoparticle diffusion coefficient and concentration, without assumptions, by combining their $D^{1/2}C$ and DC results, as shown next. Microdisk voltammetry, seen in Figure 3.8, yields the product DC from the relation for steady state limiting current (i_{LIM}) and C,

$$i_{lim} = 4 \, nFDCr_0 \qquad (3)$$

where r_0 is microdisk radius (cm). Solving for DC gives a value of 2.1×10^{-13} mol/s cm. Currents for ferrocenes on any adsorbed nanoparticles would be minimized by the slow potential scan rate.

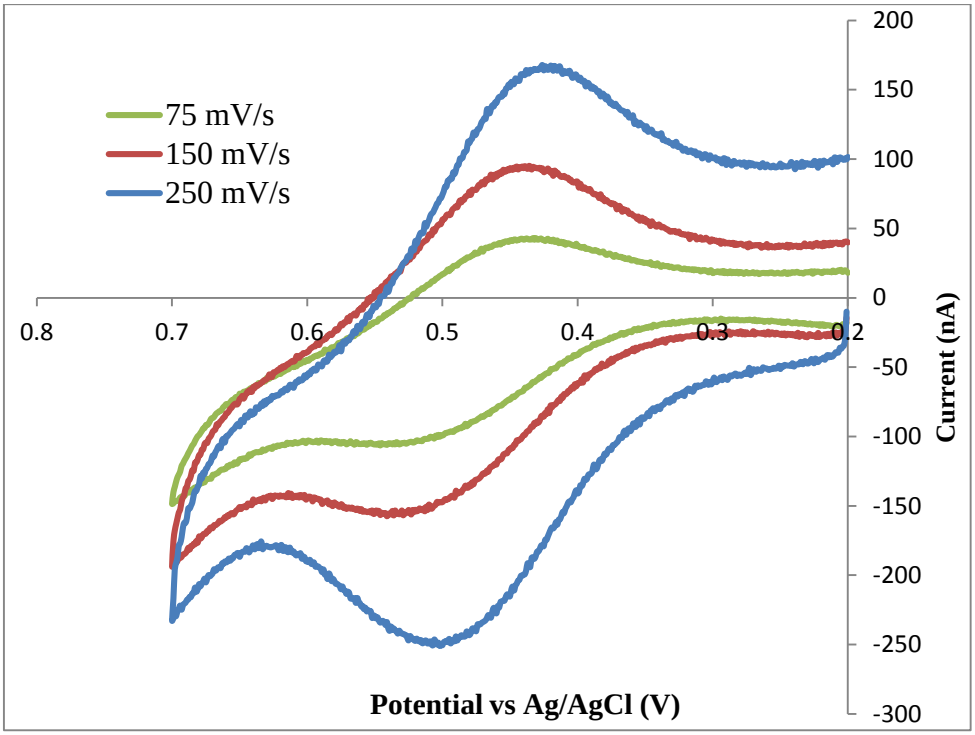

Figure 3.6 - Background subtracted cyclic voltammetry of FcITO in acetonitrile (0.1M Bu_4NClO_4) at indicated potential scan rates. Electrode area = 0.020 cm^2 .

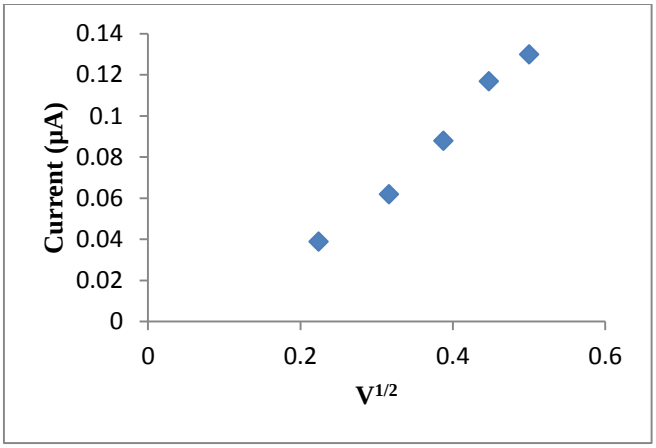

Figure 3.7 – Plot of ferrocene oxidation peak current (i_{PEAK}) *vs*. square root of potential scan rate for solution of FcITO in acetonitrile. Note the curvature and non-zero intercept, which is interpreted as indicating some nanoparticle adsorption.

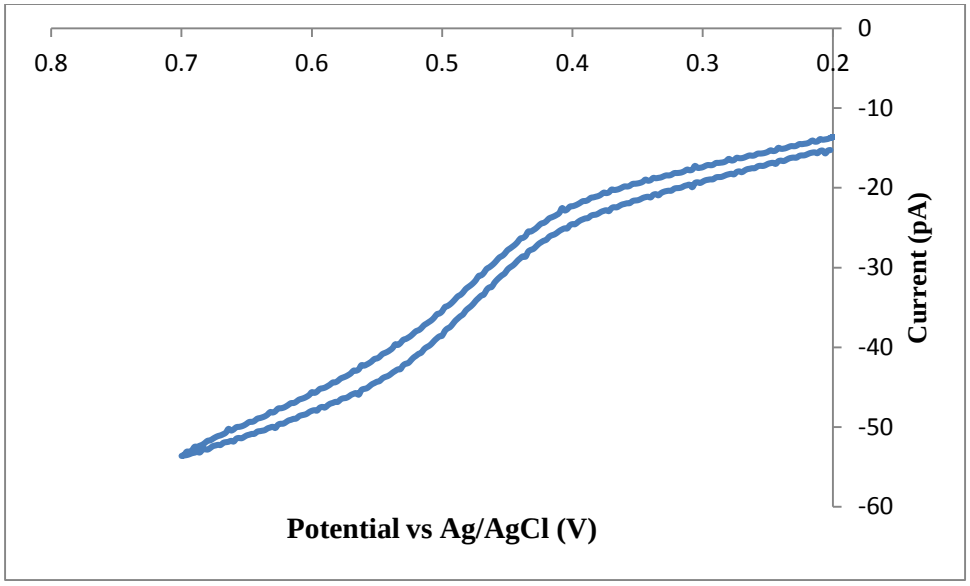

Figure 3.8 - Voltammetry of a solution of FcITO nanoparticles in acetonitrile (0.1 M Bu_4NClO_4) using a 5 μm radius disk microelectrode; potential scan rate 1 mV/s. $i_{LIM} = 1.28 \times 10^{-11}$ A.

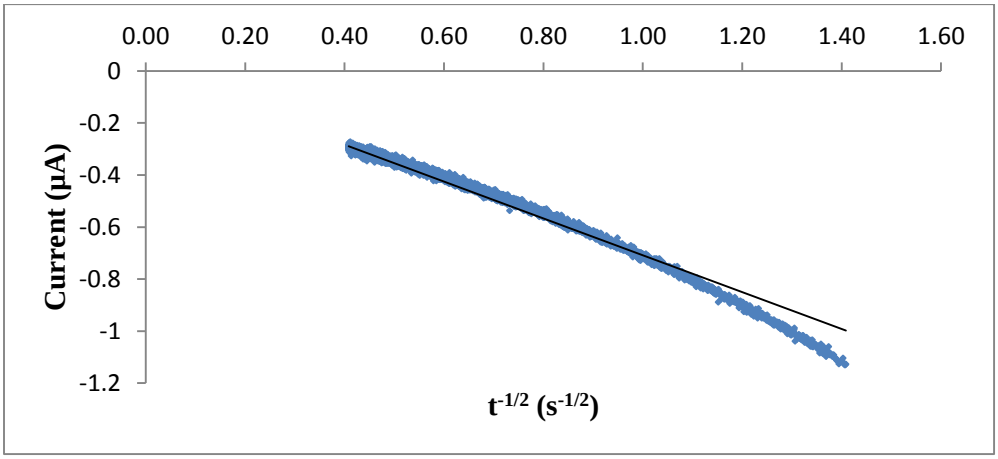

Figure 3.9 - Cottrell plot of ferrocenated ITO in acetonitrile. The potential step was from 0.45 to 0.85 V. The plot is forced through the origin as is required for linear diffusion control. Pt electrode area is 0.020 cm^2.

In potential step chronoamperometry, currents for ferrocenes on any adsorbed nanoparticles should contribute only at short electrolysis times. Currents at longer times should follow a normal Cottrell relationship, which is seen in the result of Figure 3.9 where current is measured out to 6 s. The Cottrell equation is

$$i(t) = nFAC\left(\frac{D}{\pi t}\right)^{1/2} \quad (4)$$

where t is time. From this experiment, $D^{1/2}C = 1.2\text{x}10^{-10}$ mol/s$^{1/2}$ cm^2. Taking the ratio of the two parameters produces D and C without assumptions, and yields $D = 1.0\text{x}10^{-6}$ cm^2/s and ferrocene concentration C = 0.60 mM. We see that the diffusion coefficient determined by this method is within a factor of two of the Einstein-Stokes equation prediction, and the determined ferrocene concentration is more than two-fold smaller than the titration-predicted 1.3 mM.

The preceding results—from the ferrocene titration and combined microelectrode-chronoamperometry results indicate that ferrocene sites coupled to the ITO nanoparticles are accessible to a small, diffusing oxidizing reagent (e.g., Cu^{2+}) but are not fully accessible during nanoparticle diffusion-collision with the working electrode (a large reagent). This conclusion is tested in Figure 3.10, where increments of 1 mM ferrocene carboxylic acid solution are added to a 3 mL solution of ferrocenated ITO nanoparticles. The choice of ferrocene carboxylic acid was based on its formal potential which is only slightly more positive than that of the nanoparticle-coupled ferrocene amide group; the leading edge of the ferrocene carboxylic acid wave could mediate reaction of accessible nanoparticle-coupled ferrocene amide groups. Figure 3.10 shows that addition of a small volume of FcCOOH solution immediately enhances the ferrocene amide oxidation wave by roughly a factor of two. Further additions produce a small additional

enhancement at the ferrocene amide oxidation potential. This behavior confirms the hypothesis that the titration-detected ferrocene amides are reactive towards a small molecule oxidant.

The incomplete electrochemical reactivity of the ferrocene amide functionalities on the ITO nanoparticles stands in contrast to results for ferrocenated 13 nm dia. SiO_2 nanoparticles[12], where Cu^{2+} titration analysis indicated 590 ferrocenes had been attached (*ca*. a complete monolayer). Model calculations indicated that rotational diffusion was adequately fast (τ_{ROT} ~ 0.25 μsec) to (sequentially) bring all of these ferrocene sites into proximity with the electrode. Since the FcITO nanoparticles have a smaller diameter, rotational diffusion should in the present ideally not be a factor lessening the reactivity of all of the ITO-attached ferrocene sites, so some other factors require consideration. One is that the tendency of FcITO nanoparticles to adsorb precludes an entirely free rotational diffusion at the electrode interface. A second and equally likely issue is the lack of complete accessibility (mentioned above) owing to the roughness or porosity of the ITO nanoparticle surfaces. This latter factor could potentially be overcome using a longer chain linker between the nanoparticle and ferrocene.

3.4 Acknowledgment.

This research was supported in part by the Office of Naval Research and the National Science Foundation. We gratefully acknowledge TEM and EDX measurements performed by the Analytical and Nanofabrication Laboratory of the UNC Institute for Advanced Materials.

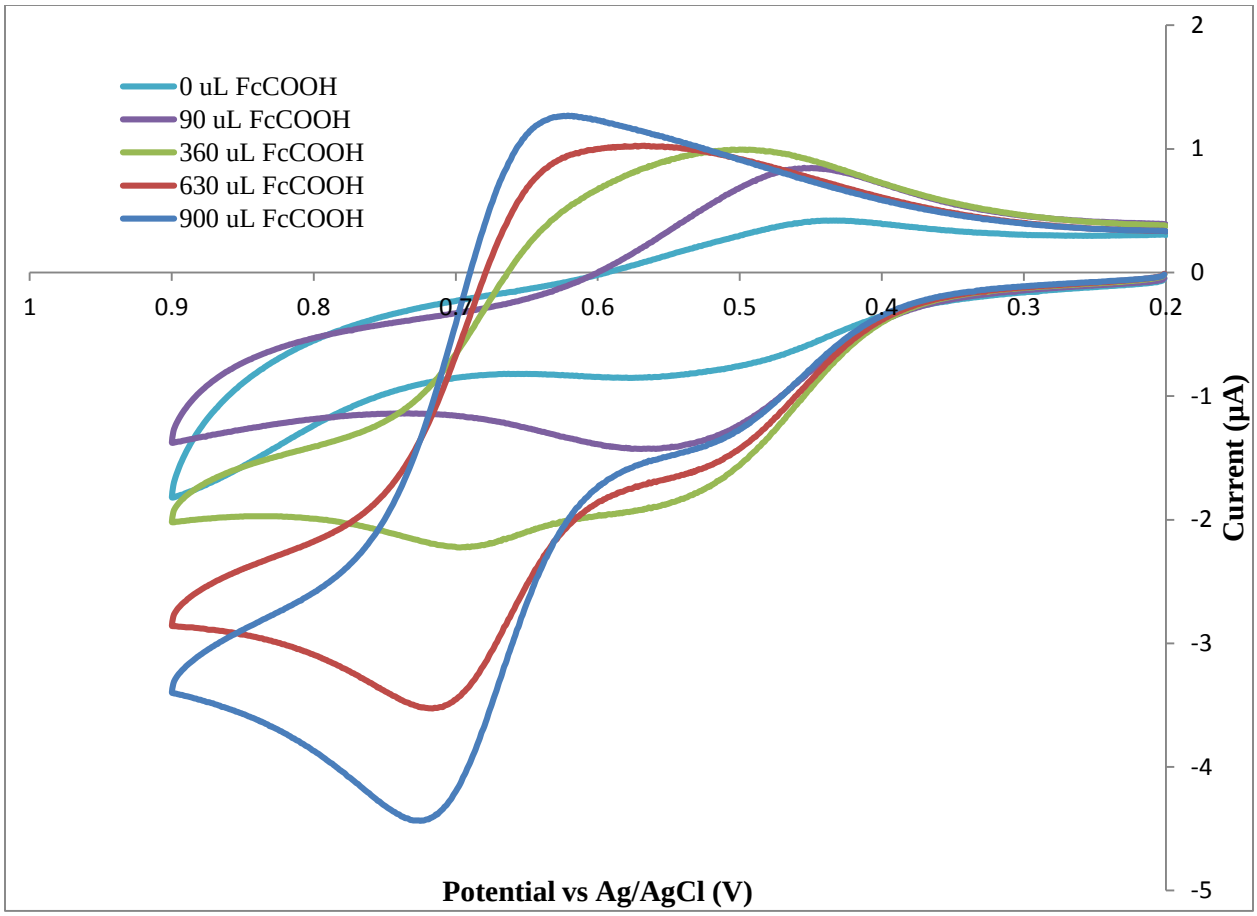

Figure 3.10 - Cyclic voltammetry of ferrocenated ITO with 90 µL additions of 1 mM FcCOOH with a scan rate of 100 mV/s. Additions of 0, 90, 360, 630, and 900 µL are shown.

3.5 References

1. Shen, Z. P. E., Three-color, tunable, organic light-emitting devices. *Science* **1997,** *276* (5321), 2009.

2. Cho, Y.-J.; Ahn, T. K.; Song, H.; Kim, K. S.; Lee, C. Y.; Seo, W. S.; Lee, K.; Kim, S. K.; Kim, D.; Park, J. T., Unusually High Performance Photovoltaic Cell Based on a [60]Fullerene Metal Cluster−Porphyrin Dyad SAM on an ITO Electrode. *J. Am. Chem. Soc.* **2005,** *127* (8), 2380-2381.

3. Neri, G.; Bonavita, A.; Micali, G.; Rizzo, G.; Pinna, N.; Niederberger, M.; Ba, J., Effect of the chemical composition on the sensing properties of In2O3–SnO2 nanoparticles synthesized by a non-aqueous method. *Sensors and Actuators B: Chemical* **2008,** *130* (1), 222-230.

4. Shi, Y.; Slaterbeck, A. F.; Seliskar, C. J.; Heineman, W. R., Spectroelectrochemical Sensing Based on Multimode Selectivity Simultaneously Achievable in a Single Device. 1. Demonstration of Concept with Ferricyanide. *Anal. Chem.* **1997,** *69* (18), 3679-3686.

5. Reindl, A.; Mahajeri, M.; Hanft, J.; Peukert, W., The influence of dispersing and stabilizing of indium tin oxide nanoparticles upon the characteristic properties of thin films. *Thin Solid Films* **2009,** *517* (5), 1624-1629.

6. Choi, S.-I.; Nam, K. M.; Park, B. K.; Seo, W. S.; Park, J. T., Preparation and Optical Properties of Colloidal, Monodisperse, and Highly Crystalline ITO Nanoparticles. *Chem. Mater.* **2008,** *20* (8), 2609-2611.

7. Gilstrap, R. A.; Capozzi, C. J.; Carson, C. G.; Gerhardt, R. A.; Summers, C. J., Synthesis of a Nonagglomerated Indium Tin Oxide Nanoparticle Dispersion. *Adv. Mater.* **2008,** *20* (21), 4163-4166.

8. Sun, Z.; He, J.; Kumbhar, A.; Fang, J., Nonaqueous Synthesis and Photoluminescence of ITO Nanoparticles. *Langmuir* **2010,** *26* (6), 4246-4250.

9. Zhang, Z.; Lu, M.; Xu, H.; Chin, W.-S., Shape-Controlled Synthesis of Zinc Oxide: A Simple Method for the Preparation of Metal Oxide Nanocrystals in Non-aqueous Medium. *Chemistry – A European Journal* **2007,** *13* (2), 632-638.

10. Mahajeri, M.; Voigt, M.; Klupp Taylor, R. N.; Reindl, A.; Peukert, W., Evaluation of the film formation and the charge transport mechanism of indium tin oxide nanoparticle films. *Thin Solid Films* **2010,** *518* (12), 3373-3381.

11. Neouze, M.-A.; Schubert, U., Surface Modification and Functionalization of Metal and Metal Oxide Nanoparticles by Organic Ligands. *Monatshefte für Chemie / Chemical Monthly* **2008,** *139* (3), 183-195.

12. Beasley, C. A.; Murray, R. W., Voltammetry and Redox Charge Storage Capacity of Ferrocene-Functionalized Silica Nanoparticles. *Langmuir* **2009,** *25* (17), 10370-10375.

13. Chow, K.-F.; Sardar, R.; Sassin, M. B.; Wallace, J. M.; Feldberg, S. W.; Rolison, D. R.; Long, J. W.; Murray, R. W., 3D-Addressable Redox: Modifying Porous Carbon Electrodes with Ferrocenated 2 nm Gold Nanoparticles. *The Journal of Physical Chemistry C* **2012,** *116* (16), 9283-9289.

14. Haensch, C.; Hoeppener, S.; Schubert, U. S., Chemical modification of self-assembled silane based monolayers by surface reactions. *Chem. Soc. Rev.* **2010,** *39* (6), 2323-2334.

15. Stiles, R. L.; Balasubramanian, R.; Feldberg, S. W.; Murray, R. W., Anion-Induced Adsorption of Ferrocenated Nanoparticles. *J. Am. Chem. Soc.* **2008,** *130* (6), 1856-1865.

16. Quirk, P. F.; Kratochvil, B., Determination of ferrocene derivatives by oxidation with copper(II) in acetonitrile. *Anal. Chem.* **1970,** *42* (4), 535-536.

17. Schmidt, S. P.; Basolo, F.; Trogler, W. C., Reactions between dimanganese, dirhenium, and manganese–rhenium decacarbonyl and oxidants. *Inorg. Chim. Acta* **1987,** *131* (2), 181-189.

18. Wuelfing, W. P.; Templeton, A. C.; Hicks, J. F.; Murray, R. W., Taylor Dispersion Measurements of Monolayer Protected Clusters: A Physicochemical Determination of Nanoparticle Size. *Anal. Chem.* **1999,** *71* (18), 4069-4074.

19. Faulkner, A. J. B. a. L. R., *Electrochemical Methods: Fundamentals and Applications*. 2nd ed.; John Wiley & Sons, Inc.: Phoenix, Az, 2001.

CHAPTER 4 – SPECTROSCOPIC AND ELECTROCHEMICAL MODIFICATION OF SMALL (<10 NM) METAL OXIDE NANOPARTICLES

4.1 Introduction

A wealth of research has been dedicated to modifying the surfaces of MO_x nanoparticles. Surface passivation helps prevent flocculation and agglomeration, and can control nanoparticle solubility and functionality. Iron oxide nanoparticles are receiving biological attention due to their magnetism and low toxicity[1-2]. However, as synthesized iron oxide nanoparticles are not suitable for physiological environments and must undergo surface modification. Frequently these modifications aspire to make nanoparticles polar by coating them in inert polar shells[3]. Other times, the surface is functionalized to interact with specific biological moieties in a system for enhanced detection[4]. Biological applications are only a subset of nanoparticle surface modifications found in the literature. Solar energy researchers have an interest in modifying the surface of transparent conducting oxide (TCOs) nanoparticles deposited on transparent conductive electrodes. The nanoparticles can be modified with chromophore-bearing phosphates that generate photocurrent when exposed to light[5]. This current can flow through the transparent conducting electrode to generate hydrogen fuel at an opposite electrode. Many common organic function groups are known to interact with MO_x surfaces[6]. Most common are carboxylic acids, amines, silanes, and phosphates/phosphonates. Carboxylic acids and amines attach by physisorptive and chemisorptive interactions, meaning they often form an equilibrium between

the nanoparticle surface and the surrounding solution. They are typically used for short term modification or simple changes in polarity. Silanes, phosphates, and phosphonates covalently attach to the metal oxide surface, typically only being removed by the addition of strong acid or strong base. This work focuses on siloxane and phosphate surface modification with the goal of quantifying surface changes through the use of a spectroscopic or electrochemical tag.

4.1.1 Surface Modification by Siloxane Chemisty

Silanes are known to react with hydroxyl groups on the surface of MO_x nanoparticles, creating covalent bonds[7-8]. These bonds are relatively strong, but are subject to hydrolytic cleavage in the presence of strong base or strong acid and function best between pH ranges of 4-12. Multidentate silane reactions must be kept extremely dry as when moistened they will polymerize by undergoing self-hydrolysis. This is especially true with chlorosilanes which will immediately react with water to form very reactive Si-OH bonds which then quickly react with other Si-OH bonds to form Si-O-Si chains. Alkoxysilanes are more resistant to hydrolysis, often requiring a small amount of catalyst to facilitate formation of Si-OH bonds. These Si-OH bonds can react with surface hydroxyl groups on the metal ion to generate Si-O-M bridges. The polymerization makes forming silane monolayers on nanoparticles difficult. Unless special care is taken, nanoparticles may become flocculated due to silanes polymerizing around them. A trade-off must be made between reactivity and polymerization potential if accurate quantification of surface modification is desired. Monodentate silanes exist, and though slow to react they do prevent multilayer formation on the nanoparticle surface. Perhaps the greatest advantage of using silanes for surface modification is the sheer number of commercially available chemicals. Silanes are very popular for a wide range of chemistries and many companies, like Gelest[9],

produce huge catalogues filled with materials for surface modifications at extremely affordable rates.

Many siloxane surface modification routes utilize 3-aminopropyltriethoxysilane (APTS) or a similar amine terminated molecule[10-11]. Primary amine attachment is often coupled with a significant change in solubility, providing a qualitative indicator of successful surface modification. Primary amines also allow for many simple organic reactions to further alter the surface chemistry via multistep functionalization. Primary amines are known to react with activated carboxylic acid groups which allow a wide range of coupling reactions, most notable acyl chloride[12-13] and carbodiimide couplings[14-15]. The primary amines can also form imide bonds with aldehydes[16]. These bonds are easily hydrolyzed and allow a temporary and reversible surface modification.

In this work we demonstrate attachment of UV sensitive tags via siloxane modification and electrochemically active tags by siloxane and click routes to small MO_x nanoparticles of varying composition. These experiments are undertaken to analytically quantify surface changes on the nanoscale level.

4.1.2 Surface Modification by Phosphate Chemistry

Phosphates, similarly to silanes, also react with surface OH groups found on the MO_x nanoparticle surface. These P-O-M bonds are more stable vs hydrolysis than the Si-O-M bonds, but pH extremes can still cause the bonds to hydrolyze. Multidentate phosphates are also incapable of forming the P-O-P bonds that would lead to polymerization. This makes them a much better choice for analytic treatment of nanoparticle surface modification. Unfortunately, there is not as diverse a selection of functionalities commercially available for phosphates. Obtaining the desired functionality often requires synthesis of the phosphate from starting

materials capable of producing that functionality. While these are frequently textbook organic reactions, they can prove difficult for those unfamiliar with common organic practices.

Recently, phosphates have received some attention as surface ligands to support click chemistry. Work by Turro *et. al.*[17] showed a simple route to generate an azide terminated phosphate ligand. This ligand was attached to a MO_x surface and then further reacted by using the azide alkyne Huisgen cycloaddition in the presence of a Cu(I) catalyst. Turro showed functionalization with 5-chloropentyne and α-acetylene-poly(*tert*-butyl acrylate) polymer, but suitable functionalities are limited by their ability to support an alkyne. Xian *et. al.* used this route to graft ferrocene to iron oxide nanoparticle surfaces for magnetically controlled electrochemistry[18]. Click chemistry products are inherently easy to work up, with limited by-products and low hazard wastes[19] and make a very attractive route to analytically tag nanoparticles when coupled with the covalent surface attachment of phosphate groups.

4.1.3 Analytical Methods for Quantification of Surface Modification

The literature on how to modify MO_x surfaces is quite large, but there is only a small body of work discussing analytical quantification of the proposed surface changes. Several spectroscopic methods exist for quantifying surface amines[13, 20-21]. One of these methods is to use an UV sensitive aldehyde to form an imine bond[16]. This bond can easily be hydrolyzed to restore the primary amine, so dry conditions are required to collect quantitative data. Another route is to use acyl chloride coupling to construct an azo-dye from the primary amine[22]. This route is not water sensitive, but requires many synthetic steps to ultimately yield the dye. It also relies on the fact that the silanes are bound to substrates as a film, making cleaning the reaction substantially easier. Modifying the surfaces of freely diffusing nanoparticles is more difficult.

Alternately, electrochemical methods have been used to modify MO_x nanoparticle surfaces. An electrochemically active silane ligand was synthesized in the Murray lab using carbodiimide coupling of ferrocene carboxylic acid and 3-aminpropyltrimethoxysilane[14]. The nanoparticles showed excellent electrochemical behavior and demonstrated that all of the 600 ferrocenes are the nanoparticle were electrochemically active at the same formal potential. This work was later followed up with ITO nanoparticles (Chapter 3)[12]. In this case the nanoparticle surface was first modified with a monodentate silane and later modified with ferrocenoyl chloride. Electrochemistry of the FcITO also showed one formal potential but curiously showed that not all of the ferrocene in solution reacted at the electrode surface. Other systems now exist for attaching ferrocene to nanoparticle surfaces via phosphates[18]; this provides a more attractive analytic route for surface modification.

4.2 Experimental

4.2.1 Chemicals and Materials

Indium(III) acetate ($In(ac)_3$; 99.99%), tin(II) (acetate) ($Sn(ac)_2$; 99.99%) were obtained from Alfa Aeser, zirconium(IV) acetate hydroxide ($Zr(ac)_xOH_y$), zirconium(IV) acetylacetonate ($Zr(acac)_4$; 98%), oleylamine ($C_9H_{18}=C_9H_{17}NH_2$; 80-90%), oleic acid ($C_9H_{18}=C_8H_{15}COOH$; 97%), myristic acid ($CH_3(CH_2)_{12}COOH$; 99%), octadecylamine ($CH_3(CH_2)_{17}NH_2$; 90%), octadecene ($C_{16}H_{33}=CH_2$; 90%), ferrocene carboxylic acid (FcCOOH; 97%), oxalyl chloride (ClCOCOCl; 98%), ethynylferrocene (FcC_2H; 97%), copper sulfate ($CuSO_4$; 99%), sodium ascorbate ($C_6H_7NaO_6$; 98%), sodium azide (NaN_3; 99%), sodium carbonate (Na_2CO_3; 99%), phosporyl chloride ($POCl_3$; 99%), 4-nitrobenzyl chloride ($O_2NC_6H_4CH_2Cl$; 99%), α-bromoisobutyryl bromide ($(CH_3)_2CBrCOBr$; 98%), nitrobenzaldehyde ($O_2NC_6H_4CHO$; 98%), sodium borohydride ($NaBH_4$; 96%), palladium on carbon (Pd/C; 5 wt%), sodium nitrite ($NaNO_2$;

97%), imidazole (>99%), pyridine (> 99.0%), ethylene glycol (HOC_2H_4OH; 99%), and propylamine ($C_3H_7NH_2$; 98%) from Sigma-Aldrich and tetrabutylammonium perchlorate (Bu_4NClO_4) and glacial acetic acid (99.7%) from Fisher Scientific. Acetonitrile (MeCN), absolute ethanol, hexanes, dichloromethane (DCM), petroleum ether, toluene, and chloroform obtained from Fisher Scientific were dried over 4 Angstrom molecular sieves. Silanes, 3-aminopropyldimethylethoxysilane (APTMES), and N-(2-aminoethyl)-3-aminopropyltrimethoxysilane (NAATMS) was obtained from Gelest, Inc. (Morrisville, PA) and stored refrigerated.

4.2.2 Instrumentation and Electrochemical Details

Cyclic Voltammetry (CV). CV was performed on a CH Instruments (CHI) 660a potentiostat with Pt working electrode (area 0.02 cm^2), Pt mesh counter electrode, and Ag/AgCl/3 M KCl (aq) reference electrode. Acetonitrile solutions were made with 0.1 M tetrabutylammonium perchlorate electrolyte while DCM solution contained 1.0 M tetrabutylammonium perchorate to minimize the solvents resistivity.

Programmable Temperature Control Unit. A lab constructed device controlled by a CAL 9500P programmable process controller with attached to a thermal couple was used to accurately control synthesis temperatures.

Centrifuge. Centrifugation was done with an Eppendorf 5810 centrifuge with a fixed-angle rotator at 3000-4000 rpm for 10 minutes.

Ultraviolet-Visible Spectroscopy (UV-Vis). UV-Vis spectra were taken on a Thermo Evolution Array UV-Vis spectrophotometer (Thermo, Waltham, MA)

4.2.3 Silane-Capped ITO and ZrO Nanoparticles.

A 1 mL hexane solution of nanoparticles was rotovapped to dryness, the nanoparticles were weighed and redissolved in 4 mL toluene in a scintillation vial. APTMES was added in 10-fold excess (relative to estimated total nanoparticle surface area), which was ~0.03 g per 0.1 g nanoparticles. 0.05 g (0.75 mmol) of imidazole was added as catalyst and the solution, which became a turbid blue, was stirred vigorously at room temperature for 24 hr. The solution was transferred to a 15 mL centrifuge tube and centrifuged at 4000 RPM for 10 minutes. The aminated nanoparticles were washed twice more with fresh toluene and then dispersed in 3 mL of toluene for storage.

4.2.4 Synthesis of N,N-Dimethylaniline Dye

The synthesis of dye modification of ITO is modified from the previously reported synthesis of an N,N-dimethylaniline free indicator dye[22] (Scheme 4.1). Propylamine (120 mmol) (**1**) and sodium carbonate (37.5 mmol) were placed in 25 mL of distilled water and heated at 60 °C for 90 minutes while 4-nitrobenzyl chloride (**2**) (16 mmol) was slowly added to the solution. The white precipitate formed was collected by filtration and washed several times with distilled water (**3**). Reduction of **3** was performed in a 100 mL ice bath with sodium borohydride (19.2 mmol) and a catalytic amount of %5 Pd/C (ca. 1 mol% Pd) (**4**). The pH was adjusted with sodium carbonate to make the solution slightly basic and **4** was extracted with CF (3x50 mL) and concentrated. **4** was acidified slightly to protonate the primary amine and added to cold water in the presence of sodium nitrite (1.5 mmol) to form the diazonium salt (**5**). **5** was filtered, washed, and immediately reacted with 5 mL N,N-dimethylaniline (39 mmol; **6**) in 2 mL acetic acid. The resulting solution was adjusted to pH 9 to form a precipitate which was collected and washed

with distilled water (**7**). A similar process was attempted with silane-capped ITO nanoparticles replacing propylamine.

4.2.5 Amine Quantification via Imine Coupling with ZrO_2 Nanoparticles

The procedure for imine coupling to amine terminated surface was previously reported[16]. Briefly, 5 mg of silane-capped ZrO_2 in CF was placed into a 1.5 mL microcentrifuge tube. The nanoparticles were washed 4 times with 1 mL of a coupling solution (0.8% v/v glacial acetic acid in anhydrous methanol) to protonate the primary amine. A 5 mM solution of 4-nitrobenzaldehyde (0.05 mmol) in 10 mL coupling solution was prepared. 1 mL of the 4-nitrobenzaldehyde solution was added to the silane-capped nanoparticles and was sonicated for 3 hr. The nitrobenzaldehyde nanoparticles were isolated via centrifugation in a microcentrifuge at 8000 RPM for 10 minutes and washed 4 times 1 mL of coupling solution. 1 mL of hydrolysis solution (75 mL H_2O, 75 mL methanol, and 0.2 mL glacial acetic acid) and sonicated for an additional hour. The supernatant was collected after centrifugation and used for UV-Vis experiments.

4.2.6 Synthesis of Ferrocenoyl Chloride and of Ferrocene-Functionalized ZrO Nanoparticles.

0.23 g of ferrocene carboxylic acid (1.00 mmol) was suspended in 4 mL of petroleum ether in a 25 mL round bottom flask. 2 drops of pyridine were added followed by slow addition of 100 μL oxalyl chloride (1.20 mmol); the solution bubbled and gassed upon this addition. The reaction solution was stirred under Ar for 1.5 hrs, and the petroleum ether and excess oxalyl chloride removed by pumping under vacuum (ca. 2 hr). The red-orange solid was collected in CH_2Cl_2 and placed into a 15 mL centrifuge tube and centrifuged at 4000 RPM for 10 minutes to separate the unreacted FcCOOH from the FcCOOCl. The bright red product solution was

Scheme 4.1 – Synthetic route for azo-dye modified ITO

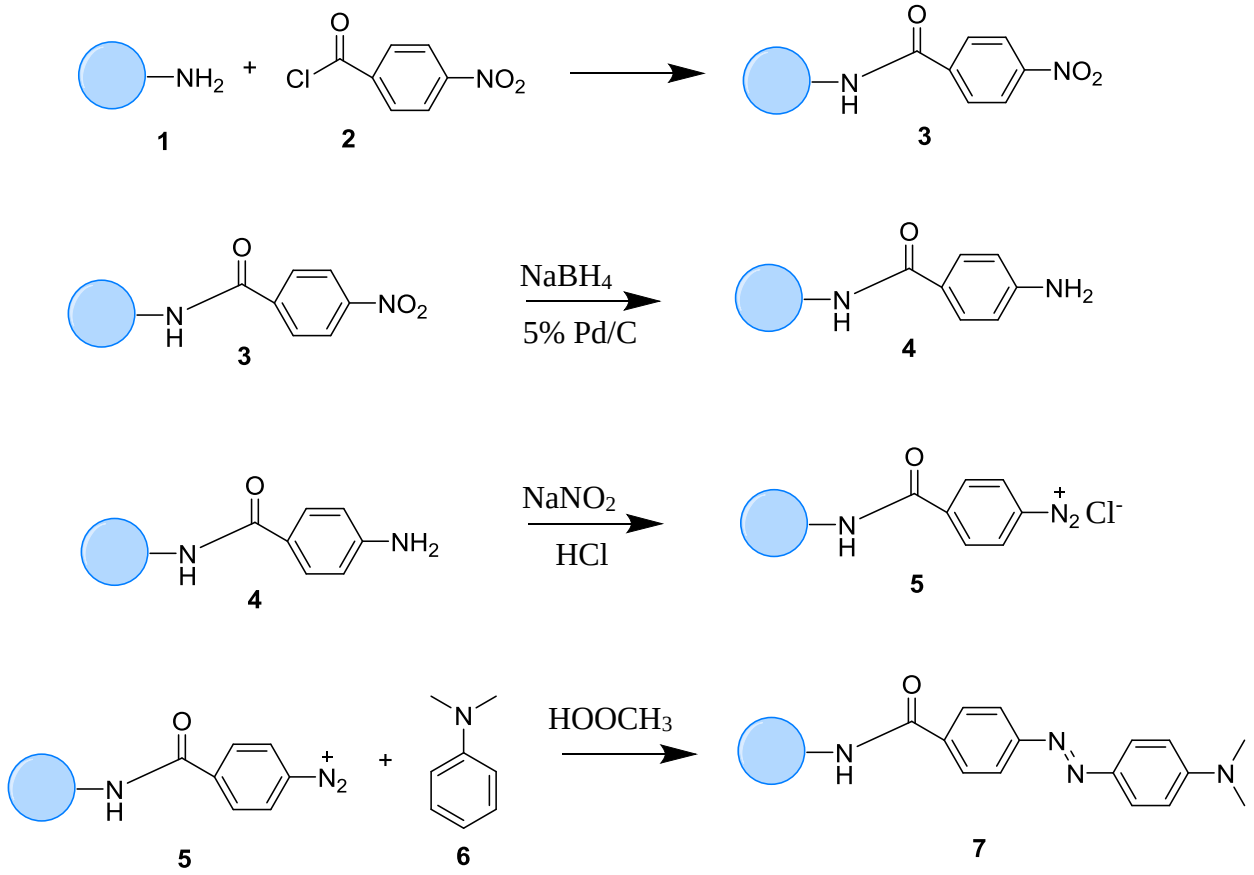

Scheme 4.2 – Synthetic route for click modified ZrO_2 and IrO_2.

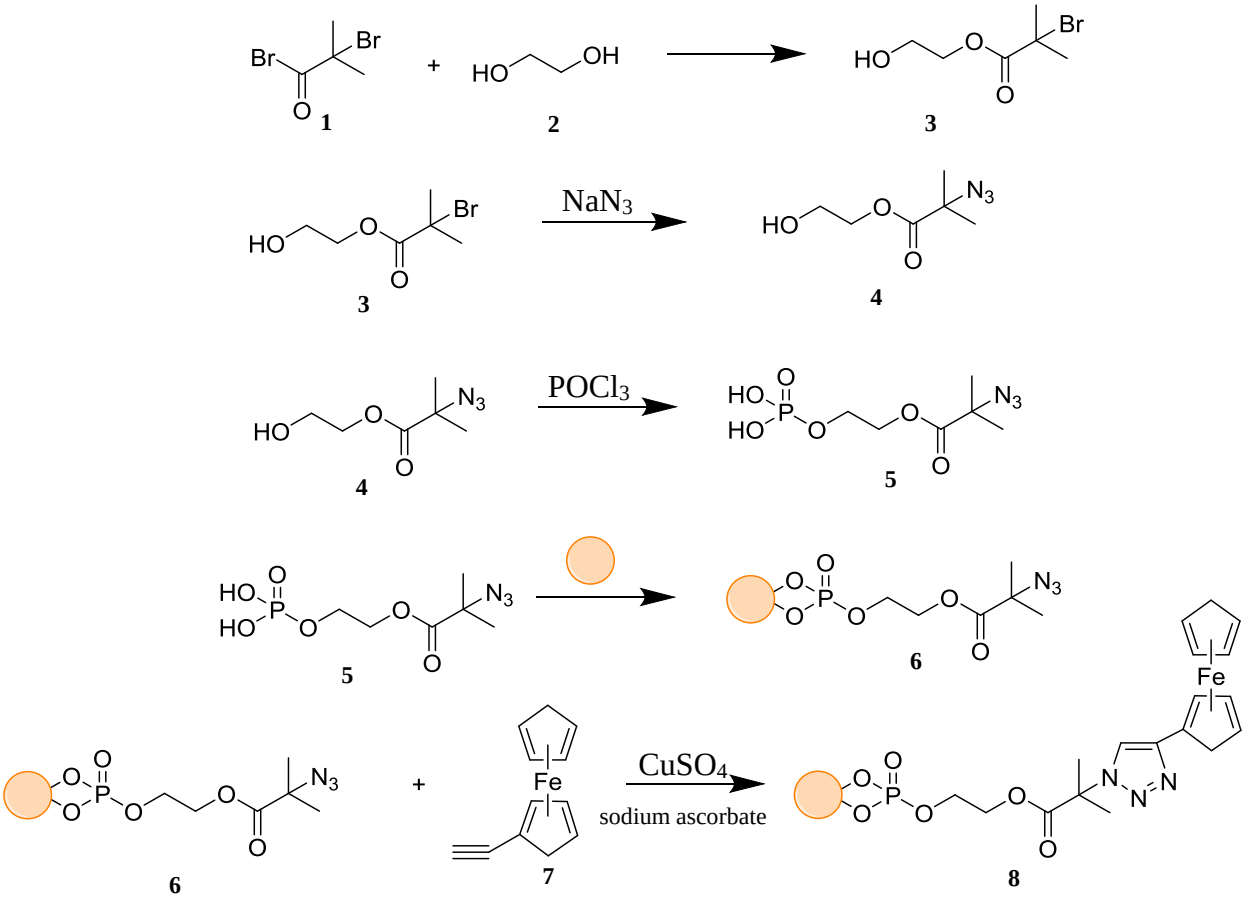

decanted and immediately reacted with silane capped ITO nanoparticles.

The 3 mL solution of silane capped ITO nanoparticles in toluene plus 50 µL pyridine (to aid activation of the acid chloride) was reacted for 1 hr. in a scintillation vial with 100 µL of the ferrocenoyl chloride solution and then transferred to a 15 mL centrifuge tube and centrifuged at 4000 RPM for 10 minutes. The precipitate was washed twice more with 5 mL toluene, then dissolved in 3 mL of acetonitrile or DCM and stored at room temperature.

4.2.7 Synthesis of Ferrocene Functionalized ZrO_2 and IrO_2 via Click Chemisty

Synthesis of the azo terminated phosphate ligand was previously reported by Turro *et. al.*[17] Click attachment of ethynyl ferrocene was previous reported by Xian *et. al.*[18] 55 mL of anhydrous ethylene glycol (1.0 mmol, **1**) was added to a flame-dried, argon-purged 100 mL round bottom flask. The flask was equipped with a magnetic stir bar and a septum and cooled to 0 °C in an icebath. 5 mL of α-bromoisobutyryl bromide (40.5 mmol, **2**) was slowly added dropwise from a syringe to the ethylene glycol and allowed to react under vigorous stirring for 3 hr. 100 mL of distilled water was added to quench the reaction and the product was extracted with chloroform (3x50 mL). The organic extract was dried over $MgSO_4$, filtered, and concentrated to a viscous clear liquid (**3**).

3 (2.0 g; 9.5 mmol) was dissolved in 15 mL of anhydrous DMF in a flame-dried, argon-purged 100 mL round bottom flask. The flask was equipped with a magnetic stir bar and septum. 680 mg of NaN_3 (10.4 mmol) was added to the solution and allowed to stir for 20 hrs. at room temperature. 20 mL of H_2O was added to quench the reaction and the product was extracted with chloroform (3x20 mL). The organic extract was dried over $MgSO_4$, filtered, and concentrated to a viscous clear liquid (**4)**. This liquid was dried *en vacuo* overnight to remove excess DMF

4 (1.0g; 5.8 mmol) was dissolved in 15 mL of anhydrous THF in a flame-dried, argon-purged 100 mL round bottom flask. The flask was equipped with a magnetic stir bar and septum. The solution was cooled to 0 °C in an ice bath and 0.9 mL of anhydrous triethylamine (6.4 mmol) was added. 0.6 mL of $POCl_3$ (6.4 mmol) was slowly added dropwise to the solution from a syringe which became cloudy white after addition. The reaction was allowed to warm to room temperature as the ice melted and allowed to stir for 3 additional hours at which point the solution became light yellow. 10 mL of H_2O was added to quench the reaction and the pH was adjusted to <2 before the product was extracted with chloroform (3x15 mL). The organic extract was dried over $MgSO_4$, filtered, concentrated, and dried under vacuum yielding a viscous yellow oil (**5**).

A 1:1 weight ratio of **5**:nanoparticles was added to 5 mL chloroform in a small scintillation vial. The solution was stirred rapidly for 24 hr before being transferred to a 15 mL centrifuge tube. Excess hexanes was added and caused the solution to become turbid. The turbid solution was centrifuged at 4000 RPM for 10 minutes. The precipitate was collected and washed 3 additional times with hexanes (**6**).

6 was dissolved in 5 mL of 4:1 DMSO:H_2O and placed in a scintillation vial with a stir bar. 26 mg of ethynylferrocene (0.124 mmol) was added followed by 3 mg $CuSO_4 \cdot 5H_2O$ (0.008 mmol) and 4 mg sodium ascorbate (0.021 mmol). The reaction was stirred for 24 h at room temperature. 1 mL $CHCl_3$, 1 mL acetone, and 1 mL ethanol were added to the solution which was transferred to a 15 mL centrifuge tube and centrifuged at 4000 RPM for 10 minutes. The precipitate was collected and washed with 3x with 4:1 DMSO:H_2O. The nanoparticles are then dispersed in DMSO for storage.

4.3 Results and Discussion

4.3.1 Spectroscopic Surface Quantification by Dye-Modified ITO Nanoparticles

Much of the previous work using azo-dyes to quantify amination involved silanes immobilized on glass or quartz substrates. This simplifies purification as the slide can be removed from excess starting material and washed independently. Many of these glass slides were used to do simple pH measurements by protonating the N,N-dimethylaniline derived dye. Synthesis of unbound N,N-dimethylaniline was substantially difficult, even before the addition of freely diffusing nanoparticles. Several attempts to synthesize the free indicator dye following the procedure by Bracci *et. al.* resulted in similar, but differing spectroscopic data. Figure 4.1 shows the UV-Vis spectra of the protonated and unprotonated forms of the N,N-dimethylaniline dye. The UV-Vis data reported by Bracci shows the protonated peak at 490 nm, an increase of 70 nm from where our dye absorbed. The absorbance spectra for the unprotonated dye from both groups were identical.

Ultimately, the bottom up approach of building the dye on the silane-capped ITO nanoparticles proved difficult. The addition of the nanoparticles caused unexpected changes during the synthesis, specifically in regards to product solubility in water. Emulsions would form during wash phases that prevented further reaction progress. However, other routes for spectroscopically tagging amines exist. Building the dye from the unbound silane could be a viable option. The 3- aminpropyldimethylethoxysilane (APTMES) only has good solubility in all of the solvents used in the synthesis, even water. The monodentate nature of APTMES makes water a minimal issue, as any self-hydrolysis would produce a dimer. The dimer would be unable to react with the nanoparticle surface and be discarded during subsequent wash steps. Alternately the N,N- dimethylaniline dye synthesis could build from 4-nitrobenzoic acid instead of

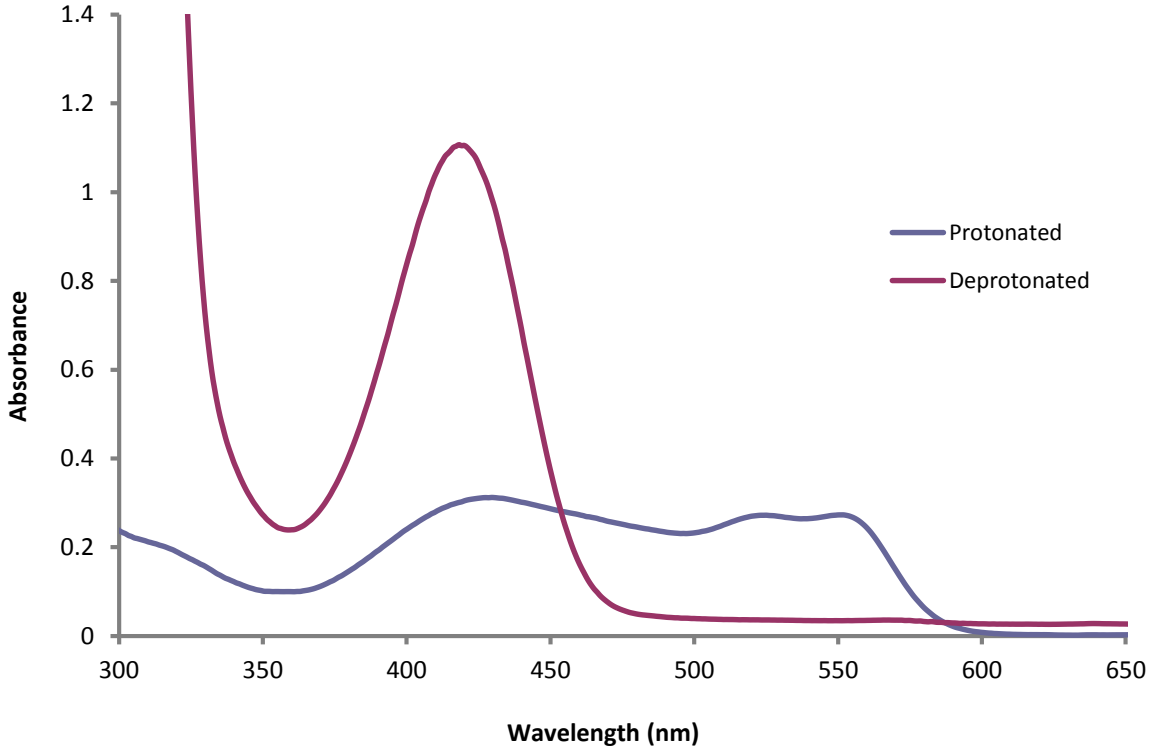

Figure 4.1 – UV-Vis spectra of protonated and unprotonated 10 mM N,N-dimethylaniline dye in water.

4-nitrobenzyl chloride and a primary amine. Once the dye was completed and purified, a subsequent reaction with oxalyl chloride would produce an acid chloride for a further reaction with the aminated nanoparticle surface. Reactivity could be an issue, and additional steps to protect functional groups might be required. This method for spectroscopically quantifying nanoparticle surface coverage was eventually abandoned for the less synthetically demanding imide coupling.

4.3.2 Spectroscopic Surface Quantification by Imine Coupled ZrO_2 Nanoparticles

Attachment of 4-nitrobenzaldehyde proved more manageable than building an azo-dye on the surface of aminated nanoparticles. A small portion of the silane-capped ZrO_2 nanoparticles was slightly acidified to form an imine bond with the UV active 4-nitrobenzaldehyde. The excess 4NBA was then washed away and the imine bond hydrolyzed to release the 4-nitrobenzaldehyde for spectroscopic quantification by Beer's Law. This simple hydrolysis regenerates the original aminated nanoparticle sample, allowing the sample to be used in further experiments after the spectroscopic analysis was complete. Ideally, an aminated nanoparticle's surface modification could be quantified spectroscopically and then electrochemically, effectively eliminating sample disparity.

The UV-Vis spectrum for 4NBA is shown in Fig. 4.2a. There is a strong absorbance at 267 nm that was used to form the calibration curve shown in Fig 4.2b, with a calculated molar absorptivity of 12106 cm^{-1} M^{-1}. Several silane-capped ZrO_2 samples were tagged with 4NBA and quantified using the calibration curve shown. Table 4.1 shows the absorbance values and subsequent concentration for 5 samples from the same batch of silane-capped ZrO_2. Each of the samples displayed concentrations in the 10-50 μM range. Comparisons were then made between the estimated surface coverage (based on the nanoparticle diameter and estimated mass) and the

concentration measured. Nearly all of the samples showed estimate surface coverages of less than 10%, suggesting an issue with either the surfactant replacement or the spectroscopic quantification. Electrochemical quantification (see below) did not agree with the spectroscopic quantification. The discrepancy between the two methods can be attributed to the difficulties keeping the samples anhydrous. While anhydrous MeOH was purchased and carefully used, individual samples of silane capped ZrO_2 were exposed to pre-prepared coupling solutions and open air conditions during washes. The original procedure also called for 3 h of end over end rotation during the formation of the imine bond, a method which would produce more vigorous solution perturbations than sonication. Generating a new calibration curve, one with multiple points in the 5-60 μM, would also improve the concentrations calculations. The author believes that access to a glove box with a contained microcentrifuge would have drastically improved the performance of spectroscopic quantification with 4NBA.

4.3.3 Surface Modification of ZrO_2 with Silane Bound Ferrocene.

Aiming at gaining control of the ZrO_2 nanoparticle surface chemistry, the surfactant capping ligands on the as-synthesized ZrO_2 nanoparticles were displaced by silanization of the surface. Silanization of macroscopic MO_x surfaces is well known reaction[23] and there are many sources for the silanization of MO_x nanoparticles as well. The goal was to form a single aminated monolayer on the nanoparticle surface for reaction with ferrocenoyl chloride. (Electroactive ligands have been previously attached to Au, SiO_2, and ITO nanoparticles[12, 14, 24] by this laboratory.) NAAPTMS was selected for this work, primarily to enhance reactivity and to prevent propylamine from interacting with the MO_x surface. After some experimentation, the silanization reaction was carried out at room temperature for 24 h, with minimal flocculation being noticed by TEM imaging. The silane coated nanoparticles precipitate out of solution after

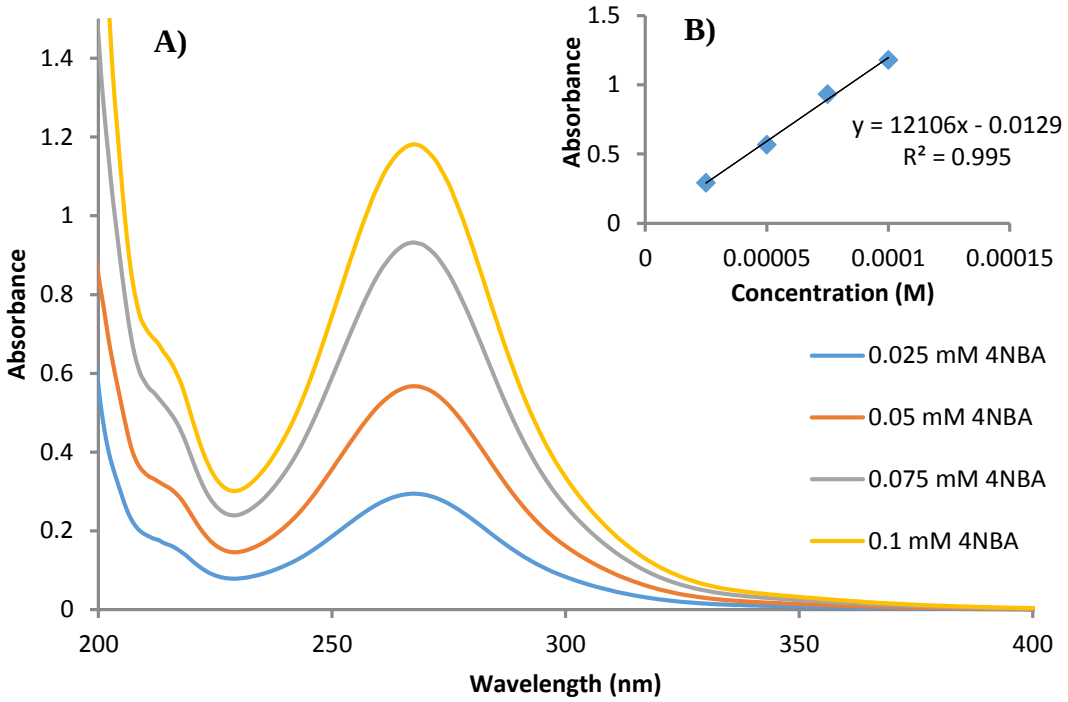

Figure 4.2 – UV-Vis analysis of 4NBA. A) shows the absorbance spectrum of serial dilutions of 0.1 mM 4NBA and B) the Beer's Law calibration curve using the peak at 267 nm.

Table 4.1 – Spectroscopic Quantification of Silane-Capped ZrO_2 Surface Modification[1]

SAMPLE NUMBER	CONCENTRATION MEASURED (μM)	ESTIMATED SURFACE COVERAGE (%)
1	17	2.0
2	43	4.6
3	10	1.2
4	47	5.0
AVERAGE	29	3.2

[1] For 5 mg/mL samples of 1.54 nm ZrO_2 nanoparticles

sufficient coating, allowing for easy collection and cleaning.

The silanized ZrO_2 nanoparticles remain dispersed in toluene for about a week at which point some precipitation usually occurs. Variability in solubility reflects incomplete displacement of the original surfactant. Nanoparticle surface composition was monitored with XPS (Fig 4.4). Post-silanization, zirconium 3d peaks are seen at 181.5 and 184 eV. Before silanization, these peaks are masked by scattering of photoelectrons by the nanoparticle capping ligands (Fig. 2.2a) which produces a large C 1s peak. Post-silanization, the C 1s peak is greatly diminished and the zirconium peak can be seen, as can low intensity Si 2p, Si 2s, and N 1s peaks.

Following silanization, a measured mass of the aminated ZrO_2 nanoparticles is reacted with freshly prepared ferrocenoyl chloride. In this procedure and in subsequent washing steps, considerable loss of product occurs in the centrifugal isolation. At least two wash steps were necessary to remove unattached ferrocene reagent, whose presence would interfere in the subsequent electrochemistry studies. TEM imaging, though difficult to interpret, appears to show that the average core diameters of the ferrocenated ZrO nanoparticles (abbrev. FcZrO) are substantially unchanged from the as-synthesized ZrO nanoparticles (Fig. 2.1). (Ferrocene substituents are not expected to contribute significantly to the image diameter.) Assuming complete nanoparticle surface coverage by the amine silane reagent, its complete coupling with ferrocenoyl chloride, and a ferrocene surface footprint of 1 nm^2, the typical 0.006 g mass of isolated FcZrO nanoparticle product in a 3 ml DCM solution would ideally correspond to an overall *ca*. 9 mM ferrocene concentration.

4.3.4 Voltammetry of Ferrocenated Silane-Capped ZrO_2 Nanoparticles (FcZrO)

Voltammetry of the FcZrO nanoparticles was carried out in 1.0 M Bu_4NClO_4/DCM solutions. The ferrocene wave was readily seen in cyclic voltammetry (Figure 4.7).

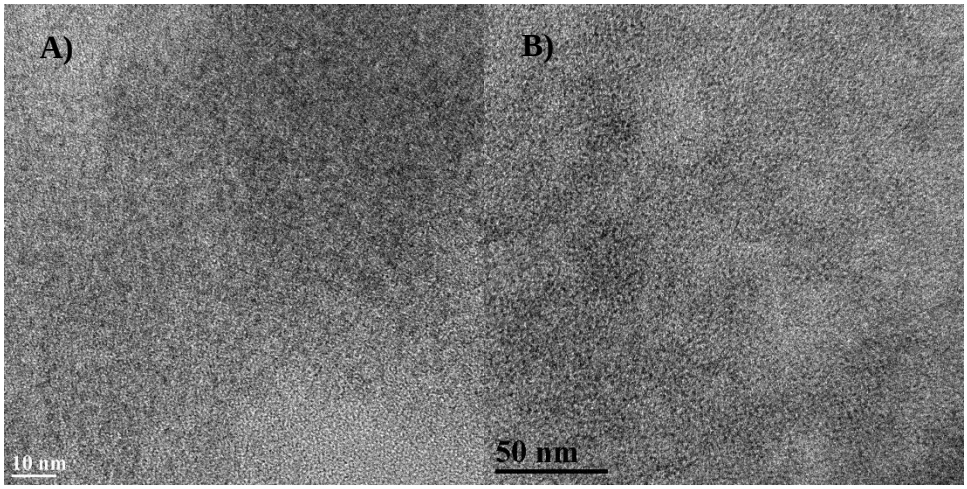

Figure 4.3 – TEM images of A)$SiZrO_2$ and B) $FcZrO_2$ nanoparticles. Scale bars are 10 nmand 50 nm respectively.

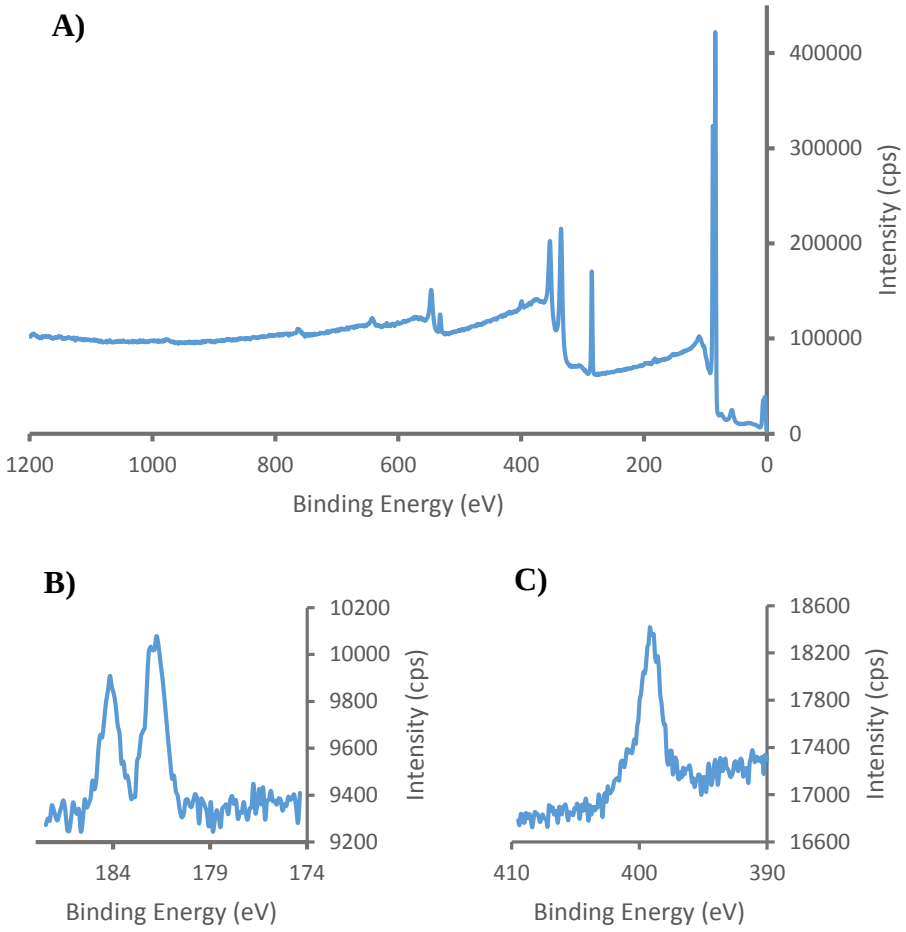

Figure 4.4 - XPS of A) SiZrO nanoparticles. B and C depict a high resolution scans of B) the Zr 3d region and C) the N 1s region.

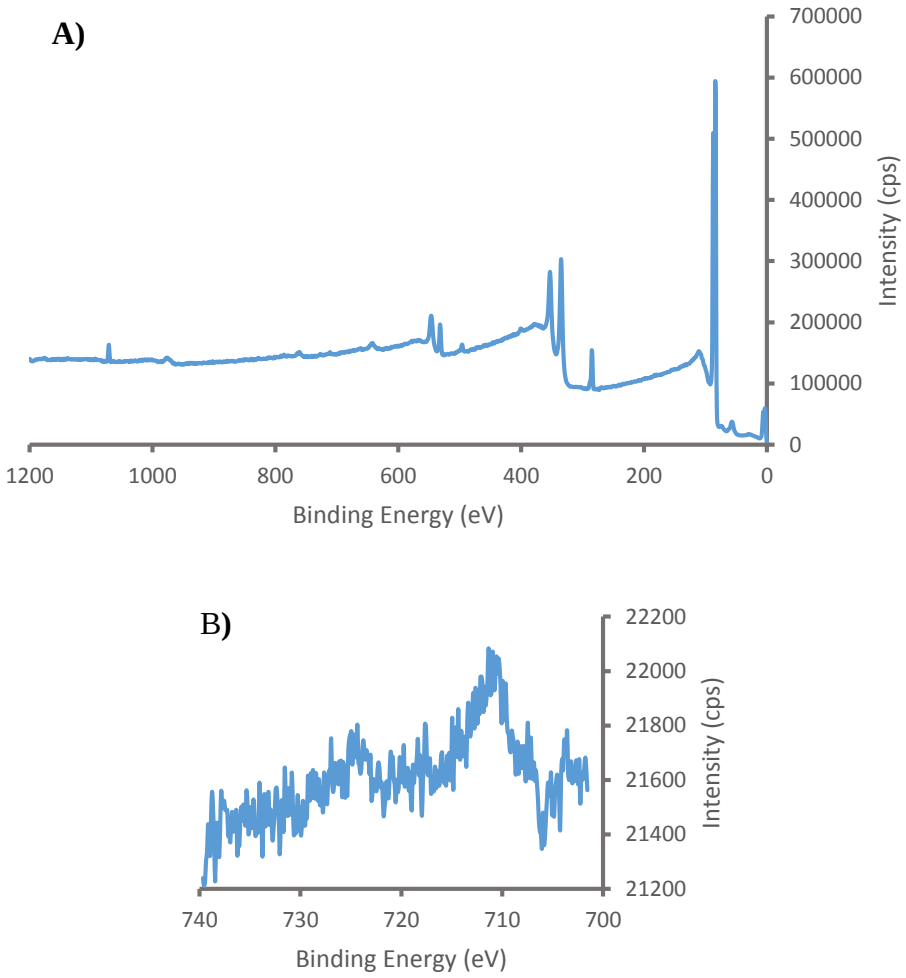

Figure 4.5 - XPS of A) $FcZrO_2$ nanoparticles. B) depicts a high resolution scan of the Fe 2p region.

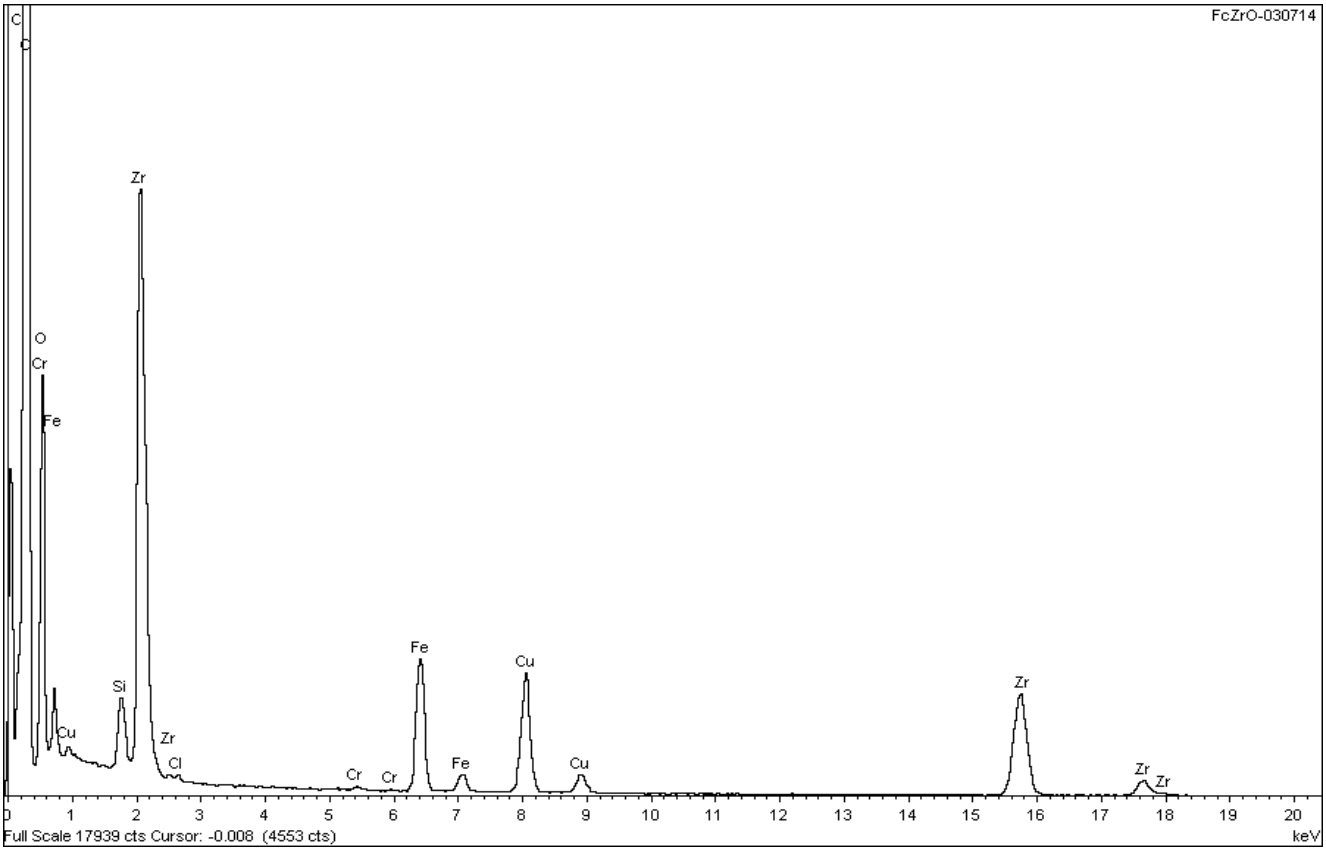

Figure 4.6 - EDX of $FcZrO_2$ nanoparticles

Measurement of the nanoparticle diffusion coefficient (D) was set as a target in quantifying the electrochemical assessment, using cyclic voltammetry, chronoamperometry, and microdisk electrode voltammetry.

The diffusion coefficient expected was estimated using the no-slip version of the Stokes-Einstein equation, which is

$$D = \frac{kT}{6\pi\eta r} \qquad (1)$$

where r is nanoparticle hydrodynamic radius and η is DCM viscosity (0.41 cP). Based on the 1.54 nm TEM nanoparticle core diameter plus a 2 nm increment for the ferrocene sites, this equation predicts a FcZrO nanoparticle diffusion coefficient of D = 3.0 x 10^{-6} cm^2/s. Previous measurements of diffusion coefficients of organothiolate coated Au nanoparticles (1-5 nm diameter), using the classical Taylor Dispersion method[25], show that a) Equation (1) can predict nanoparticle diffusion coefficients to within a factor of *ca*. two and b) that the organothiolate monolayer on the nanoparticles may be partially free-draining.

Cyclic voltammetry of the amide-connected ferrocene on the FcZrO nanoparticles shows a one electron chemically reversible wave with formal potential *ca*. 0.62 mV *vs*. Ag/AgCl(aq) (Fig. 4.3). The ΔE_{PEAK} separation is 40 mV, not 60 mV as expected from Nerstian behavior, suggesting the FcZrO has formed a film on the electrode surface. The Randles-Sevcik equation for linear sweep voltammetry[26] is

$$i_p = 2.69 * 10^5 \, n^{3/2} A D^{1/2} C v^{1/2} \qquad (2)$$

where n is the number of electrons delivered (per ferrocene), D (cm^2/s) is nanoparticle diffusion coefficient and C (mol/cm^3) is the concentration of reactive ferrocene. Figure 4.8 shows that the

peak currents do not follow the expected $v^{1/2}$ potential scan rate dependency, but show a non-zero intercept and curve upward in a manner, again suggesting adsorption of the FcZrO on the electrode. A plot of current vs scan rate (Fig. 4.9) shows excellent linearity, another strong indication of surface adsorbed FcZrO.

Currents from potential step chronoamperometry and from microelectrode voltammetry should be less affected by moderate level of nanoparticle adsorption. These two experiments yield nanoparticle diffusion coefficient and concentration, without assumptions, by combining their $D^{1/2}C$ and DC results, as shown next. Similar calculations utilizing $D^{1/2}C$ from Randles-Sevcik ($D^{1/2}C_{RS}$ = 5.88 x 10^{-10} mol/$s^{1/2}$ cm^2) are shown for comparison, despite the effects of adsorption. Microdisk voltammetry, seen in Figure 4.10, yields the product DC from the relation for steady state limiting current (i_{LIM}) and C,

$$i_{lim} = 4\, nFDCr_0 \qquad (2)$$

where r_0 is microdisk radius (cm). Currents for ferrocenes on any adsorbed nanoparticles would be minimized by the slow potential scan rate. The limiting current (i_{LIM}) was taken to be 1.87 x 10^{-11} A, resulting in a DC of 1.05 x 10^{-13} mol/s cm. Taking the ratio of $D^{1/2}C_{RS}$ and DC produces D and C, and yields D = 3.2 x10^{-8} cm^2/s and ferrocene concentration C = 3.29 mM.

In potential step chronoamperometry, currents for ferrocenes on any adsorbed nanoparticles should contribute only at short electrolysis times. Currents at longer times should measured out to 6 s. The Cottrell equation is

$$i(t) = nFAC\left(\frac{D}{\pi t}\right)^{1/2} \qquad (3)$$

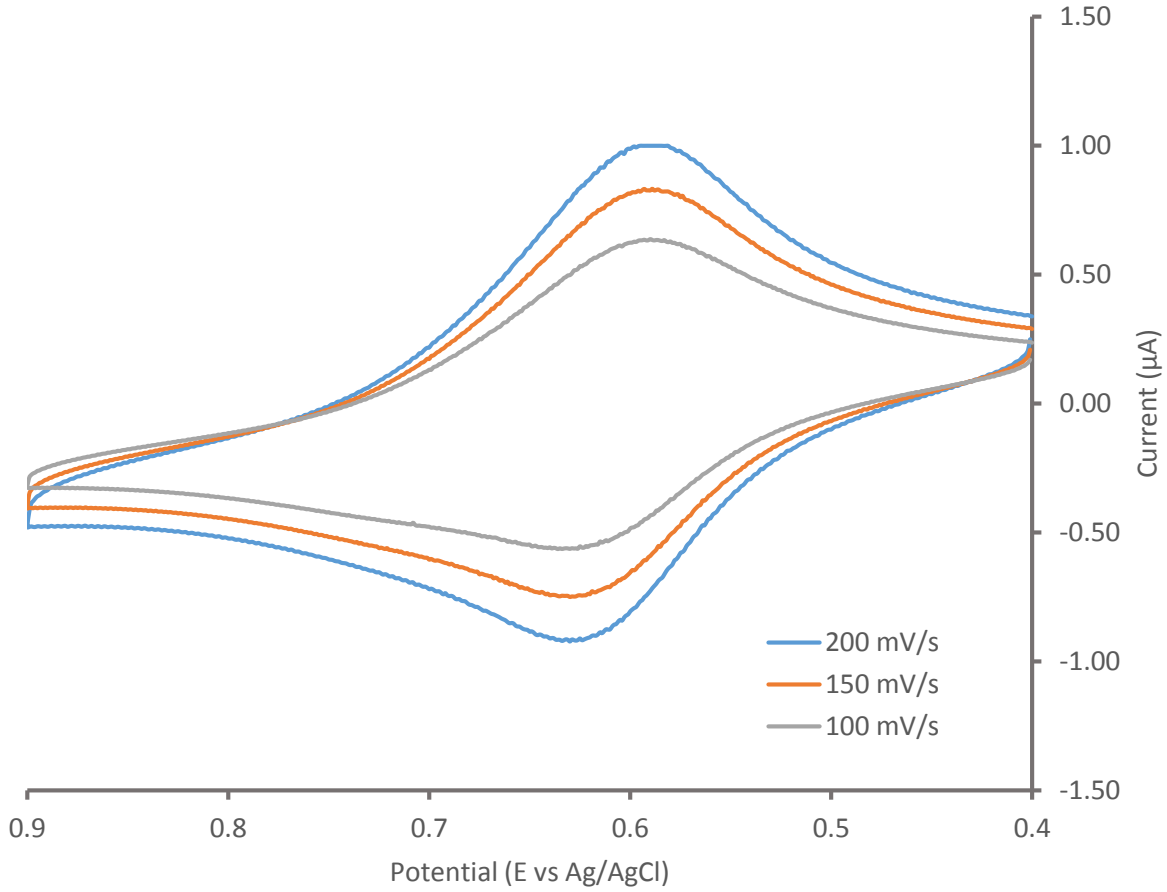

Figure 4.7 – Cyclic voltammetry of 0.4 mM $FcZrO_2$ solution in DCM with added 1 M NB_4ClO_4 electrolyte, at varying potential scan rates.

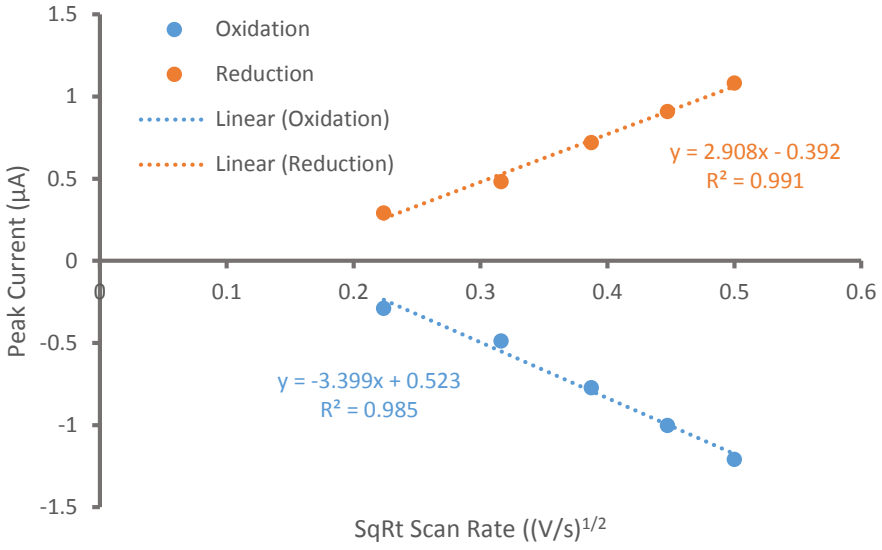

Figure 4.8 – Potential sweep rate dependence of cyclic voltammetry of a 0.4 mM $FcZrO_2$ nanoparticle solution in DCM with 1 M Bu_4NClO_4. The waves do not strongly fit a [scan rate]$^{1/2}$ dependency.

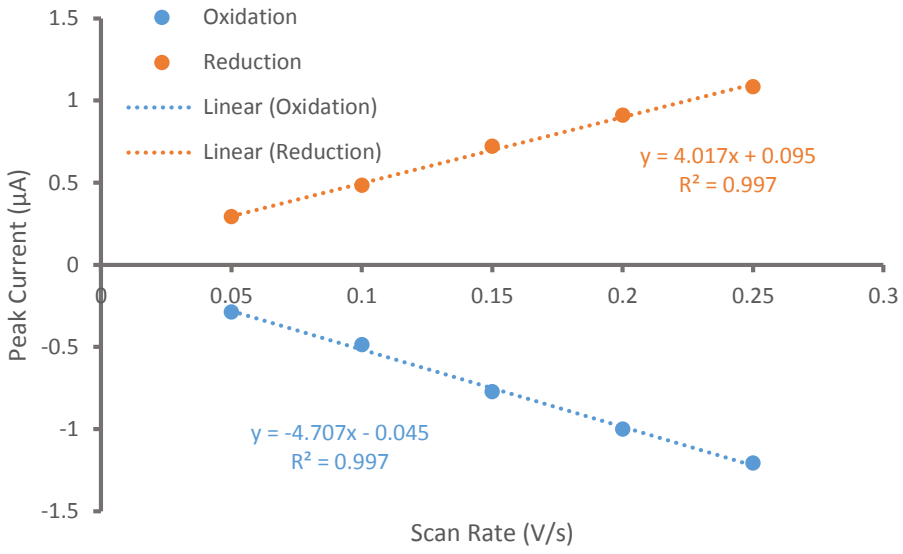

Figure 4.9 – Potential sweep rate dependence of cyclic voltammetry of a 0.4 mM $FcZrO_2$ nanoparticle solution in DCM with 1 M Bu_4NClO_4. The waves fit well with a scan rate dependency

where t is time. Examination of the Cottrell plot (Fig. 4.11) suggests ideal Cottrell behavior with a small amount of curvature at both short and long times. Deviations at short times are unsurprising as CV already suggests adsorption on the electrode. From this experiment, $D^{1/2}C_{CA}$ = $3.96x10^{-10}$ mol/$s^{1/2}$ cm^2. Performing the above ratio again, this time with $D^{1/2}C_{CA,}$ produces D and C with minimal adsorption affects, and yields D = 7.1 $x10^{-8}$ cm^2/s and ferrocene concentration C = 1.49 mM.

We see that both diffusion coefficients determined by this method are *ca*. 2 orders of magnitude lower than the Einstein-Stokes equation prediction. This large discrepancy is largely due to the adsorption effects present in the CV. The FcZrO nanoparticles may be spontaneously forming a film on the Pt electrode that is not removed during subsequent oxidation or reduction. The other possibility is that the nanoparticles have been polymerized together and are acting not as 1.54 nm individual nanoparticles but as large ferrocene coated aggregates. This would require nanoparticle aggregates of *ca.* 75 nm in diameter which have not been observed in TEM samples of FcZrO nanoparticles. Concentrations are in reasonable agreement with both being in the µM range, though a titration with Cu^{2+} is needed to accurately compare the values to the amount of ferrocene present in solution. These concentrations are significantly higher than those previously reported for ferrocene derivatized ITO nanoparticles. The improved ferrocenation of silane-coated ZrO_2 nanoparticles is a topic of ongoing research.

4.3.5 Click Ferrocenation of ZrO_2 and IrO_2 Nanoparticles

Phosphate ligands provide some advantages over their silane counterparts in regards to MO_x surfaces. While they both provide covalent bonds to metal ions, phosphates are incapable of polymerization and are more resistant to hydrolysis. Their lack of self-hydrolysis makes them interesting analytically but their multidentate nature could lead to multiparticle binding. As such

reaction times and conditions must still be optimized to prevent flocculation by the phosphate. The azo-phosphate (referred to as the click ligand) is placed into a solution of as synthesized nanoparticles and allowed to stir overnight at room temperature for ligand exchange. The coated nanoparticles precipitate out of solution due to the changed ligand polarity and are collected via centrifugation. The phosphated nanoparticles can then be redispersed into a 4:1 DMSO:H_2O solution to be clicked with the ethynyl ferrocene. The newly ferrocenated nanoparticles again precipitate and are collected and washed before being placed into DMSO or MeCN for electrochemical analysis.

This work focuses on ZrO_2 nanoparticles ferrocene modified by click chemistry. Details from unpublished work by Michaux *et.al* on click modified IrO_2 nanoparticles have been included for comparison as part of a collaboration. TEM images of the phosphated nanoparticles differ drastically (Fig 4.12ab), with the ZrO_2 nanoparticles showing a flocculated network and the IrO_2 nanoparticles maintaining their single particle nature. Both materials show minimal change in average particle diameter and shape. XPS of the phospho-azo modified IrO_2 shows a double peak for the N 1s at 399.5 and 406 eV, indicating the presence of an azide species. After ferrocenation (Fig 4.12cd) both materials form tightly flocculated clusters. Elemental analysis by XPS (Fig. 4.13 and Fig.4.15) shows the presence of the MO_x core as well as iron and nitrogen indicating some modification has occurred. It is currently unknown why the phosphate bonding varies between the materials. It may be that the rate of ligand exchange beween the capping ligands and the phosphate is heavily influenced by the ligand length (C_5 vs C_{18}). It is also unknown why the ferrocenation causes the previously unflocculated IrO_2 to flocculate. Different batches also vary in behavior. More experiments are required to fully understand these reactions and optimize surface coverage without causing flocculation.

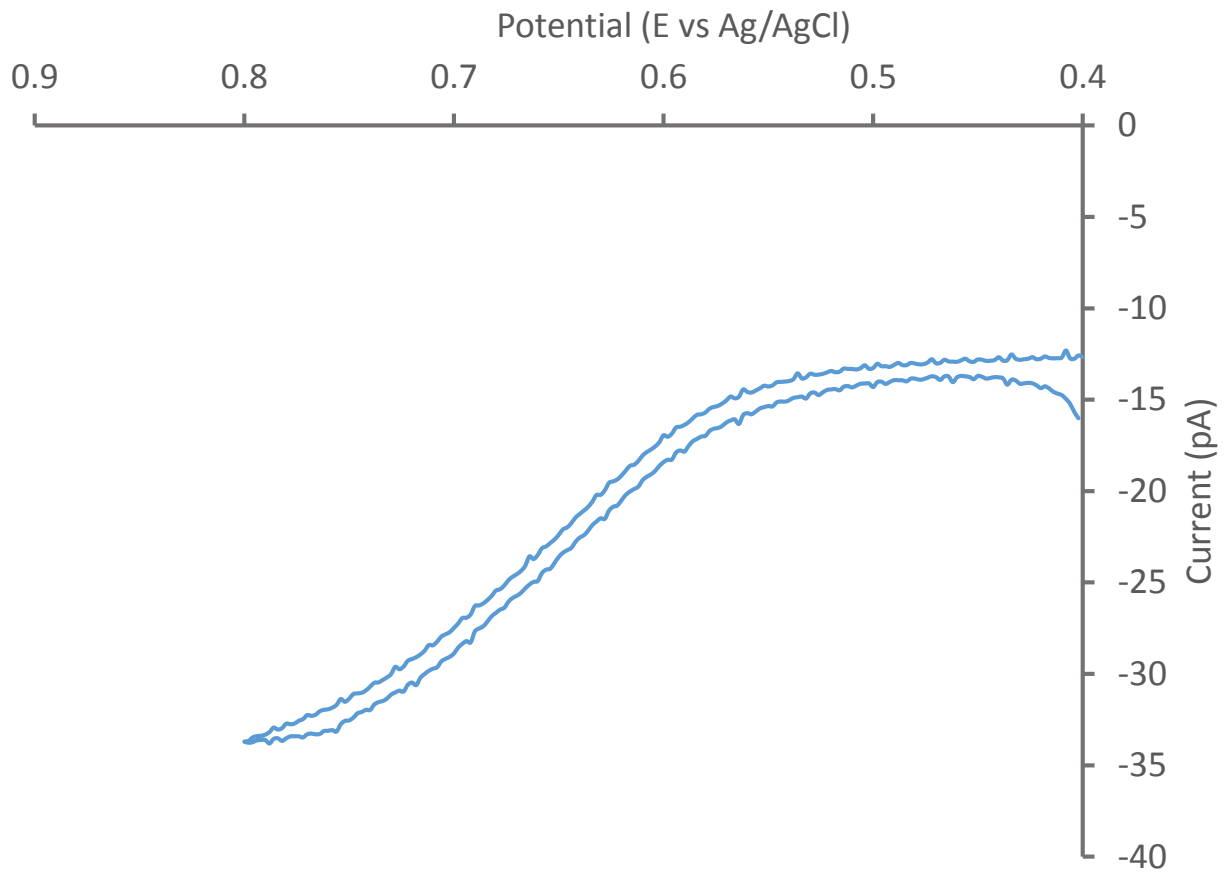

Figure 4.10 – Voltammetry of a solution of $FcZrO_2$ nanoparticles in DCM (1 M Bu_4NClO_4) using a 5 μm radius disk microelectrode; potential scan rate 1 mV/s.

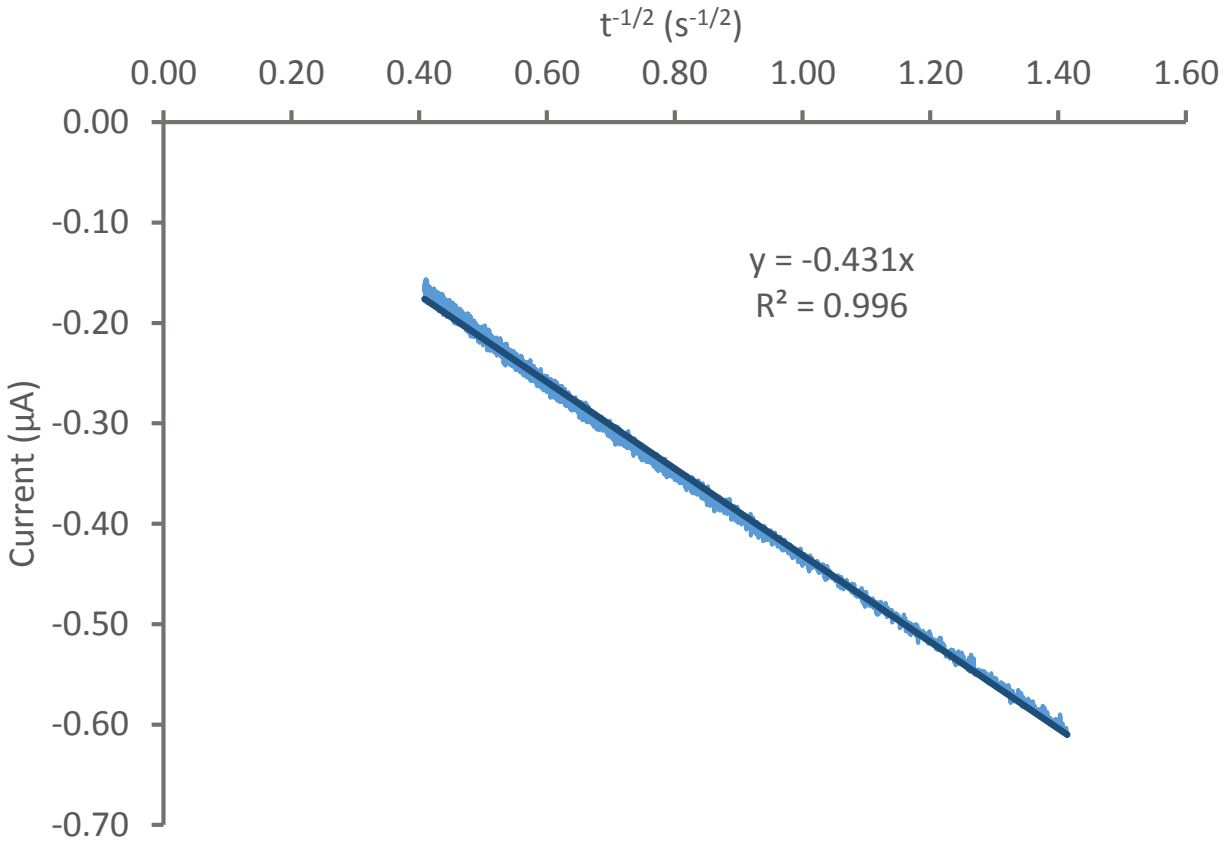

Figure 4.11 – Cottrell plot of chronoamperometric oxidation currents over a 6 second timescale for a potential step to from 0.500 V to 0.700 V vs. Ag/AgCl for a solution of $FcZrO_2$ nanoparticles in DCM with 1 M Bu_4NClO_4. The plot has been forced through a zero origin and shows very minor deviations.

Electrochemical analysis of the clicked ZrO_2 nanoparticles was performed in MeCN in the presence of 0.1 M TBAP. Electrochemisty of the clicked IrO_2 nanoparticles in DMSO with 0.1 M TBAP was performed by Michaux *et. al.* and is again included for comparison. Cyclic voltammetry of the clicked ZrO_2 (Fig. 4.16) shows a one electron, chemically reversible wave with a formal potential of *ca.* 0.61 V and a ΔE_{PEAK} of 68 mV. Comparatively, the clicked IrO_2 nanoparticles show a background dominated CV (Fig. 4.17) with a chemically reversible wave at formal potential *ca.* 0.49 V and a ΔE_{PEAK} of *ca.* 100 mV. Qualitative inquiry of the clicked ZrO_2 electrochemistry is discussed below. Quantitative analysis of clicked ZrO_2 and IrO_2 is a subject of ongoing work.

Randles-Sevcik treatment of the click-ZrO (Figure 4.18) shows excellent linearity, indicating freely diffusing species of ferrocene tagged ZrO_2 nanoparticles, though TEM images (Fig 4.12) show this freely diffusing species is likely a large flocculate of ferrocene tagged nanoparticles and not individually diffusing nanoparticles. A comparison of the Stokes-Einstein predicted diffusion coefficient and an observed diffusion coefficient could expound upon this query and is a subject of continued work. The diffusive electrochemistry is in stark contrast to the FcZrO voltammetry shown in Figure 4.7 which shows strong symptoms of nanoparticle adsorption on the electrode surface. The positively charged ferrocinium species generated during oxidation is expected to have low solubility in DCM and might explain why the MeCN dissolved click-ZrO shows little evidence of nanoparticle adsorption. Chronoamperometry of the click-ZrO oxidation peak also shows ideal Cottrell behavior (Fig. 4.19). The linear fit in Figure 4.19 has been forced through zero, as ideal behavior would predict, and still shows an excellent fit with the data. The only deviations occur at very short times, which is commonly the case during

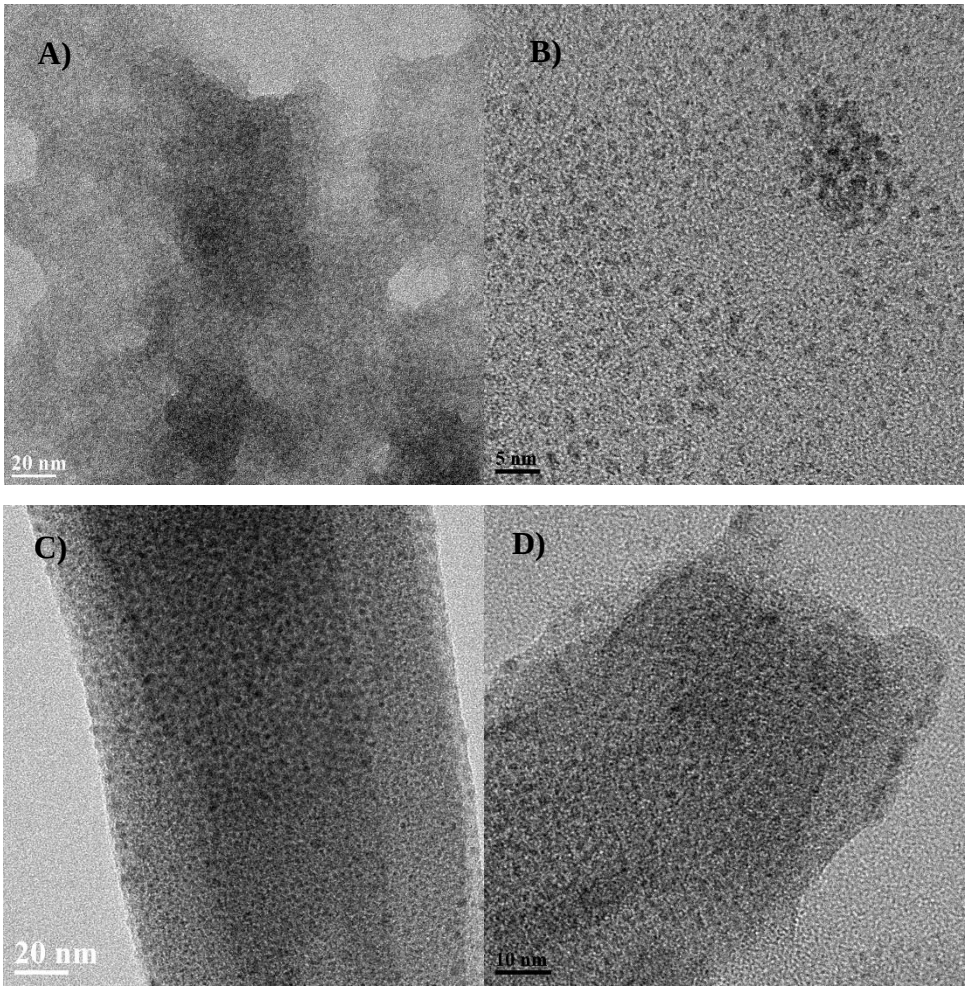

Figure 4.12 – TEM images of the click modified nanoparticles. Panels A and B depict A) phosphate modified ZrO_2 nanoparticles (20 nm scale bar) and B) phosphate modified IrO_2 nanoparticles (5 nm scale bar). C and D show the ferrocene "clicked" nanoparticles C) click-ZrO_2 (20 nm scale bar) and D) click-IrO_2 (10 nm scale bar).

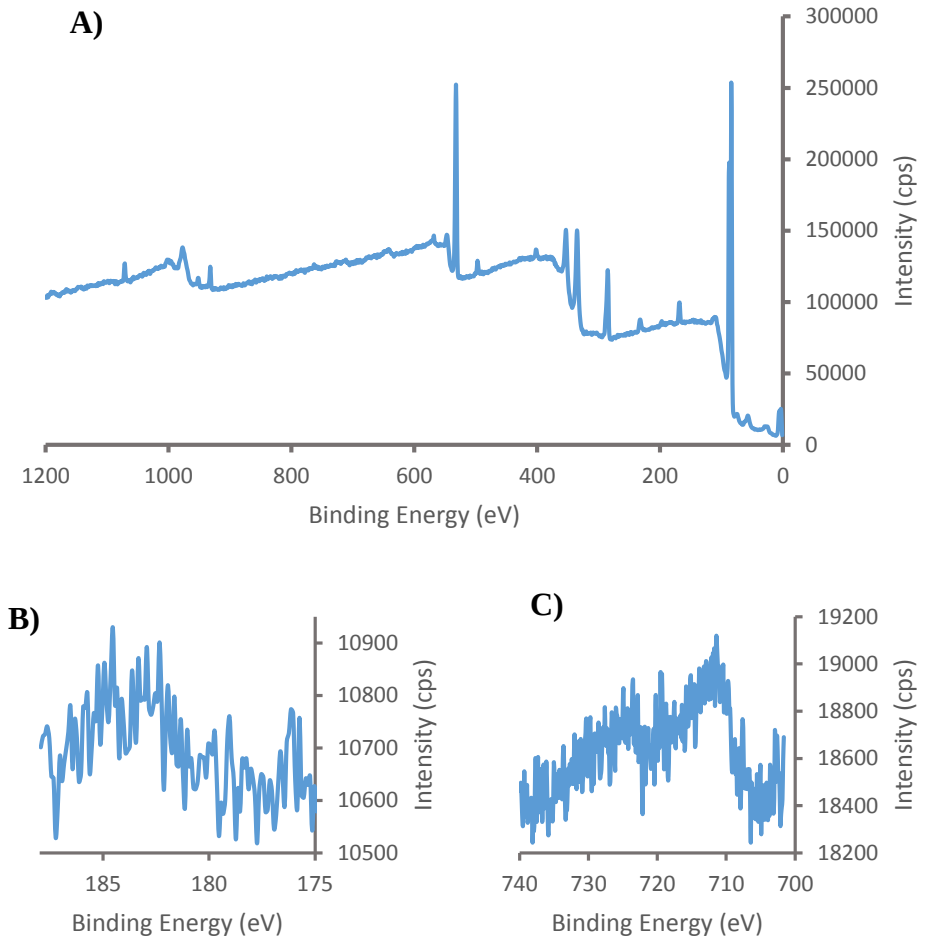

Figure 4.13 – XPS of A) Click-ZrO_2 nanoparticles. B and C show high resolution scans of the B) Zr 3d region and the C) Fe 2p region.

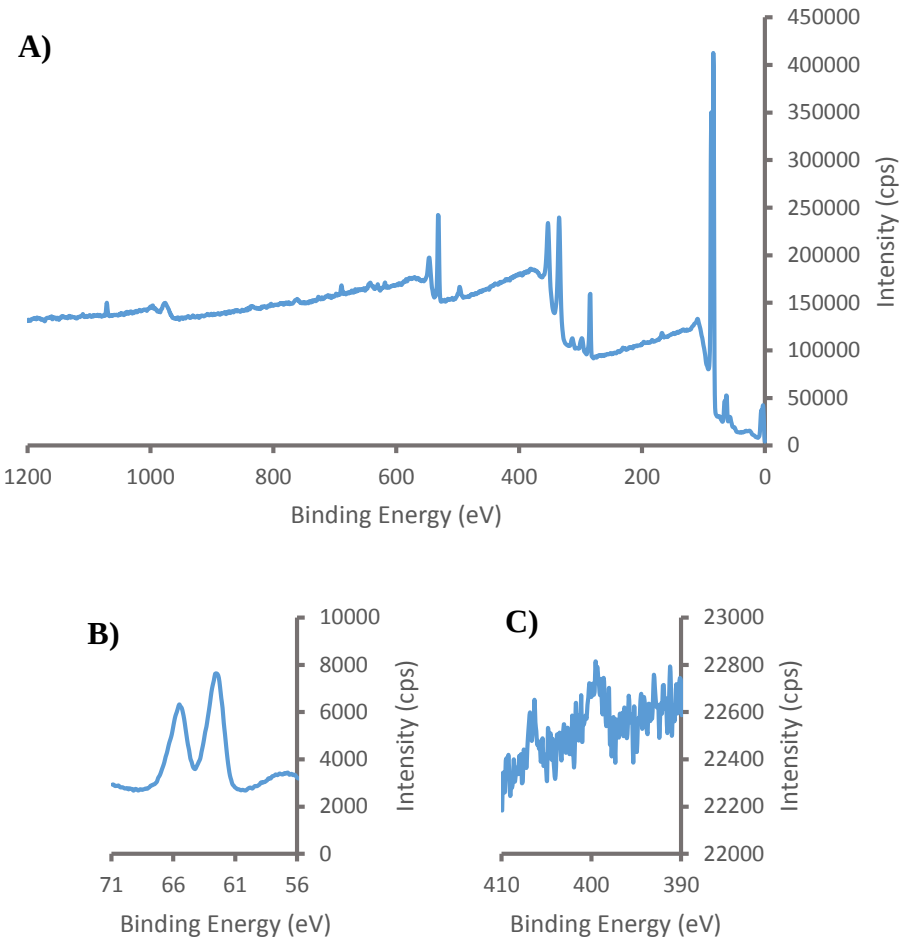

Figure 4.14 - XPS of A) azo-IrOx nanoparticles. B and C show high resolution scans of the B) Ir 4f region and the C) N 1p region.

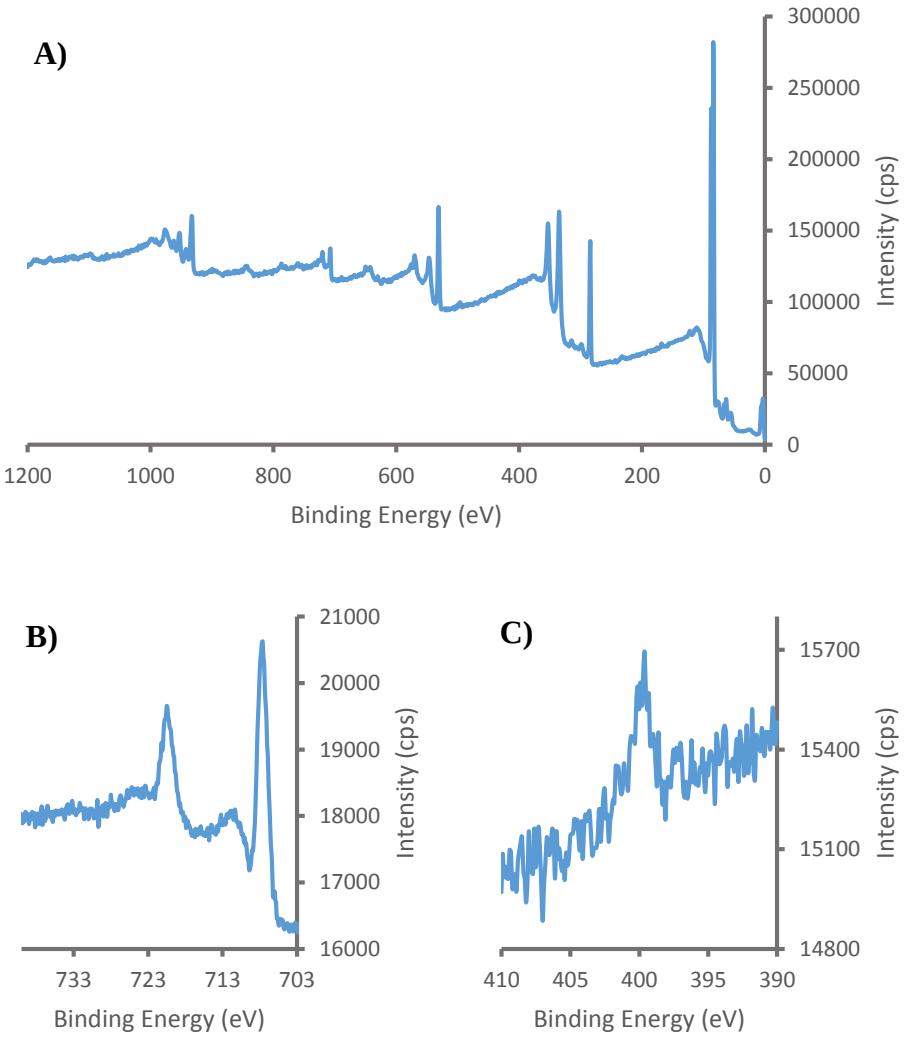

Figure 4.15 - XPS of A) click-IrO_2 nanoparticles. B and C depict high resolution scans of the B) Fe 2p region and C) N 1s region.

chronoamperometry experiments. The data presented here is only representative of the work on click-ZrO. There are many variations between batches, and a careful consideration of the parameters at work is needed to generate consistent data. Future work will include microdisk electrochemistry to calculate no-assumption values of D and C (as done with FcZrO) and Cu^{2+} titrations to determine total ferrocene concentration. With this information we can quantitatively determine surface coverage of the click-ZrO and compare that to values achieved through silanization.

4.4 Acknowledgments

This research was supported in part by the Office of Naval Research and the National Science Foundation. We gratefully acknowledge TEM, EDX, and XPS measurements performed by Carrie Donley and Amar Kumbhar of the Analytical and Nanofabrication Laboratory of the UNC Institute for Advanced Materials.

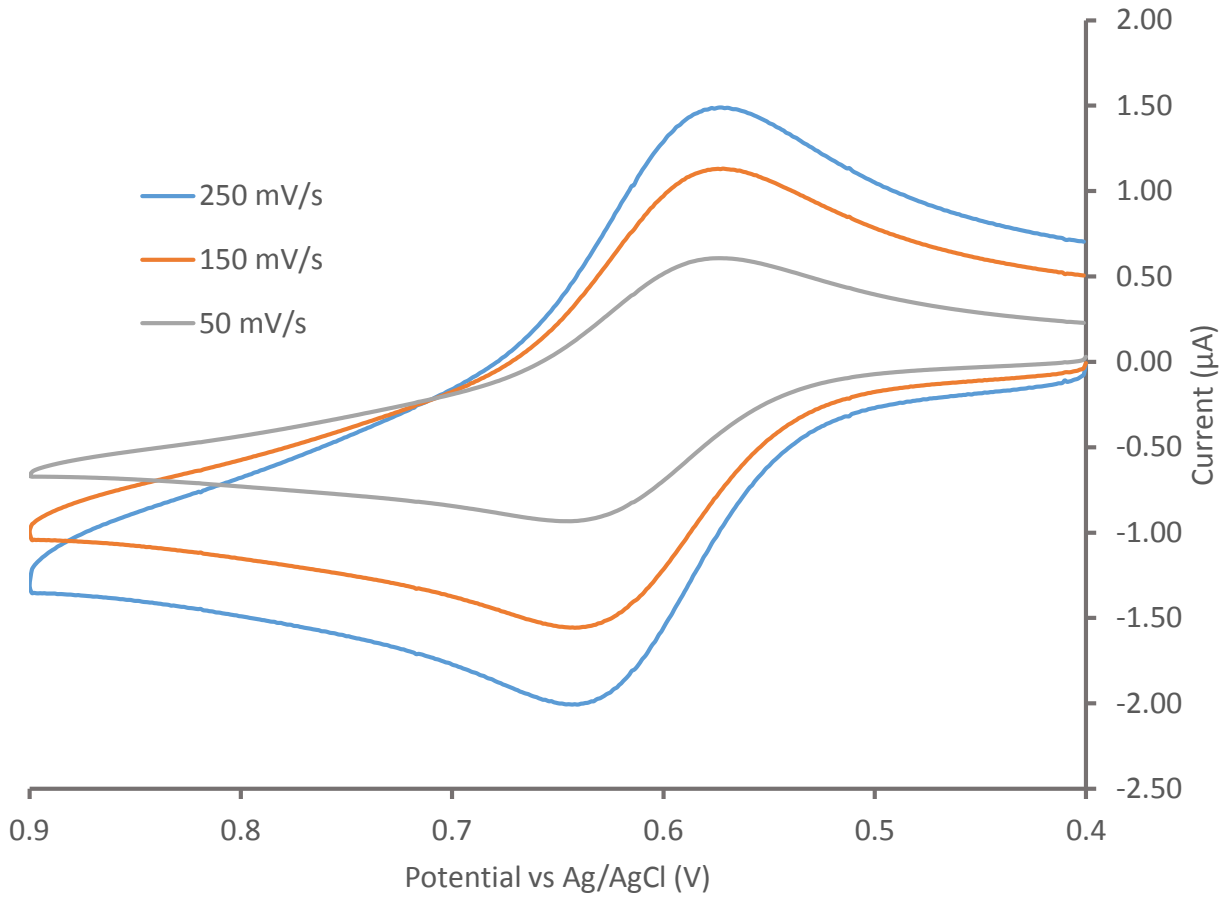

Figure 4.16 – Cyclic voltammetry of a mM click-ZrO_2 solution in acetonitrile with added 0.1 M NB_4ClO_4 electrolyte, at varying potential scan rates.

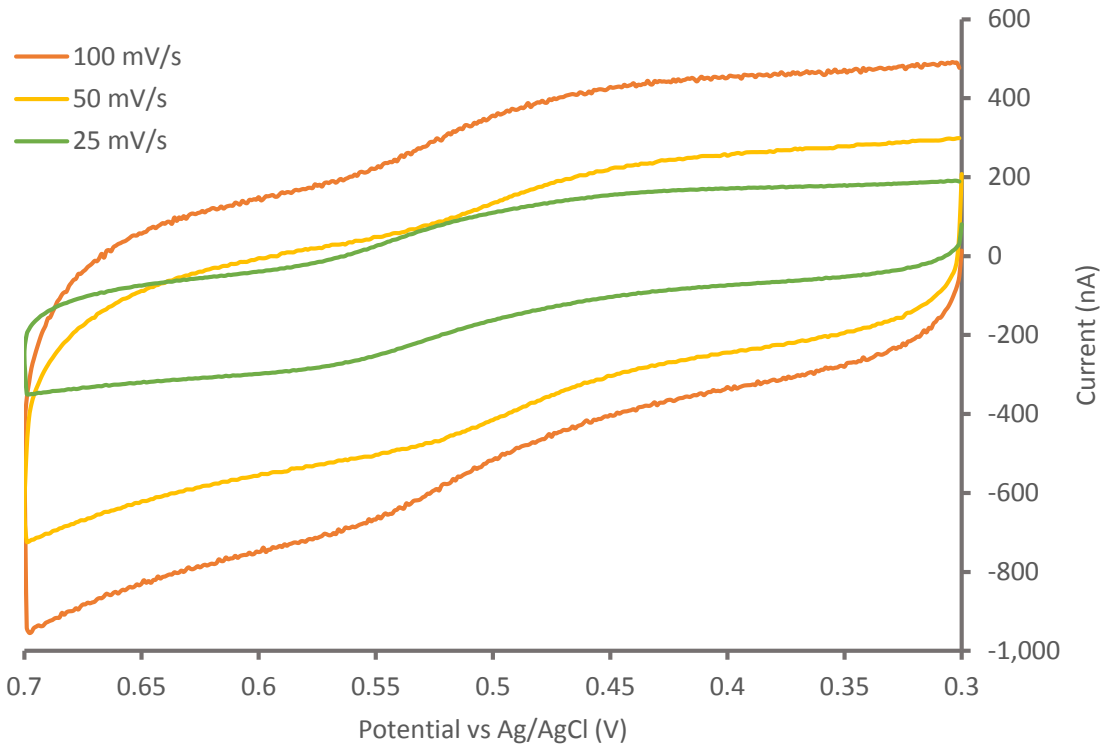

Figure 4.17 – Cyclic voltammetry of a click-IrO_2 solution in DMSO with added 0.1 M NB_4ClO_4 electrolyte, at varying potential scan rates.

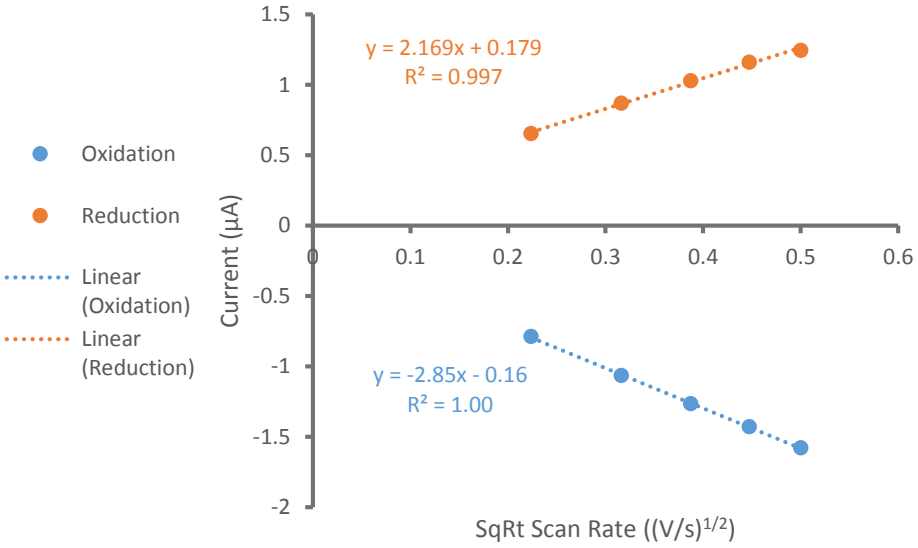

Figure 4.18 – Potential sweep rate dependence of cyclic voltammetry of a click-ZrO_2 nanoparticle solution in acetonitrile with 0.1 M Bu_4NClO_4. The waves fit a [scan rate]$^{1/2}$ dependency

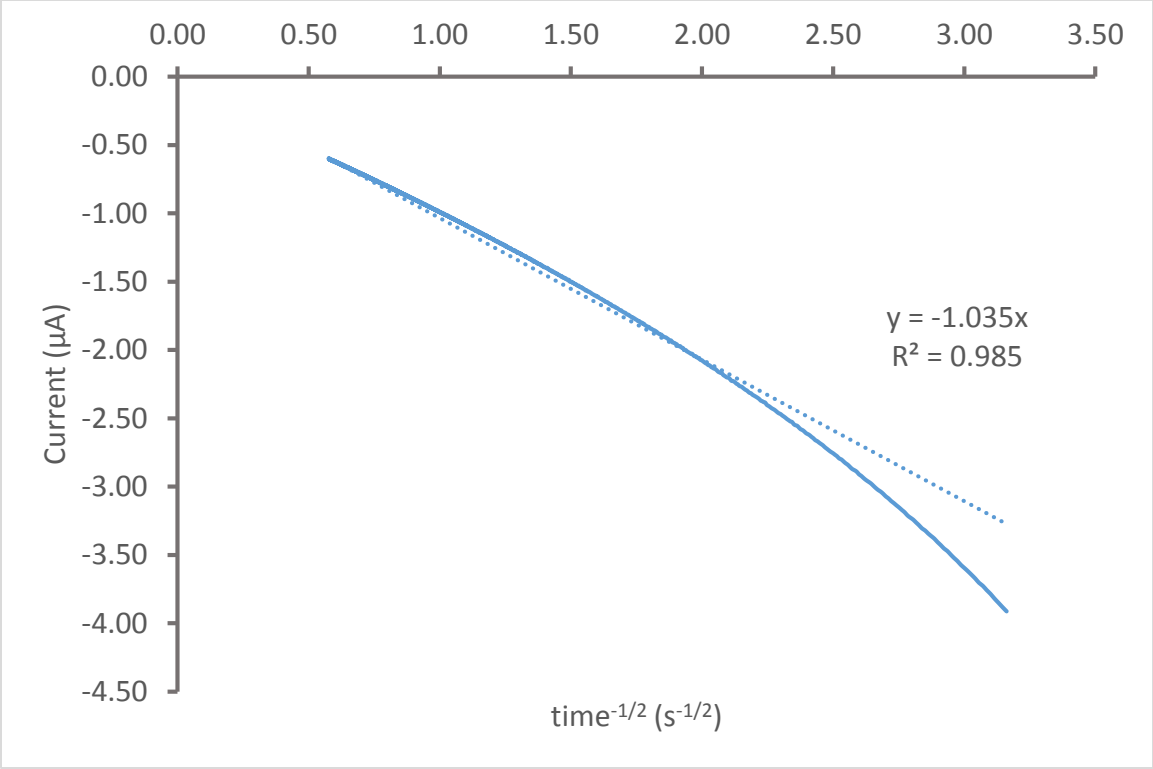

Figure 4.19 – Cottrell plot of chronoamperometric oxidation currents over a 3 second timescale for a potential step to from 0.500 V to 0.700 V vs. Ag/AgCl for a solution of click-ZrO_2 nanoparticles in acetonitrile with 0.1 M Bu_4NClO_4. The plot has been forced through zero and deviates significantly at short times.

4.5 References

1. Yiu, H. H. P., Engineering the multifunctional surface on magnetic nanoparticles for targeted biomedical applications: a chemical approach. *Nanomedicine* **2011,** *6* (8), 1429-1446.

2. Joris, F.; Manshian, B. B.; Peynshaert, K.; De Smedt, S. C.; Braeckmans, K.; Soenen, S. J., Assessing nanoparticle toxicity in cell-based assays: influence of cell culture parameters and optimized models for bridging the in vitro-in vivo gap. *Chem. Soc. Rev.* **2013,** *42* (21), 8339-8359.

3. Barrera, C.; Herrera, A. P.; Rinaldi, C., Colloidal dispersions of monodisperse magnetite nanoparticles modified with poly(ethylene glycol). *J. Colloid Interface Sci.* **2009,** *329* (1), 107-113.

4. Xie, J.; Chen, K.; Lee, H.-Y.; Xu, C.; Hsu, A. R.; Peng, S.; Chen, X.; Sun, S., Ultrasmall c(RGDyK)-Coated Fe3O4 Nanoparticles and Their Specific Targeting to Integrin αvβ3-Rich Tumor Cells. *J. Am. Chem. Soc.* **2008,** *130* (24), 7542-7543.

5. Hoertz, P. G.; Chen, Z.; Kent, C. A.; Meyer, T. J., Application of High Surface Area Tin-Doped Indium Oxide Nanoparticle Films as Transparent Conducting Electrodes. *Inorg. Chem.* **2010,** *49* (18), 8179-8181.

6. Neouze, M.-A.; Schubert, U., Surface Modification and Functionalization of Metal and Metal Oxide Nanoparticles by Organic Ligands. *Monatshefte für Chemie / Chemical Monthly* **2008,** *139* (3), 183-195.

7. Bruce, I. J.; Sen, T., Surface Modification of Magnetic Nanoparticles with Alkoxysilanes and Their Application in Magnetic Bioseparations. *Langmuir* **2005,** *21* (15), 7029-7035.

8. Zhang, C.; Wängler, B.; Morgenstern, B.; Zentgraf, H.; Eisenhut, M.; Untenecker, H.; Krüger, R.; Huss, R.; Seliger, C.; Semmler, W.; Kiessling, F., Silica- and Alkoxysilane-Coated Ultrasmall Superparamagnetic Iron Oxide Particles: A Promising Tool To Label Cells for Magnetic Resonance Imaging. *Langmuir* **2006,** *23* (3), 1427-1434.

9. Arkles, B.; Larson, G., Silicon Compounds: Silanes & Silicones. Gelest, Ed. 2008.

10. Čampelj, S.; Makovec, D.; Drofenik, M., Functionalization of magnetic nanoparticles with 3-aminopropyl silane. *J. Magn. Magn. Mater.* **2009,** *321* (10), 1346-1350.

11. Yamaura, M.; Camilo, R. L.; Sampaio, L. C.; Macêdo, M. A.; Nakamura, M.; Toma, H. E., Preparation and characterization of (3-aminopropyl)triethoxysilane-coated magnetite nanoparticles. *J. Magn. Magn. Mater.* **2004,** *279* (2–3), 210-217.

12. Roberts, J. J. P.; Vuong, K. T.; Murray, R. W., Synthesis and Electrochemistry of 6 nm Ferrocenated Indium–Tin Oxide Nanoparticles. *Langmuir* **2012,** *29* (1), 474-479.

13. Mimms, L. T.; McKnight, M. A.; Murray, R. W., Spectrophotometric study of coverage and acid-base equilibrium of a chemically bonded base. *Anal. Chim. Acta* **1977,** *89* (2), 355-361.

14. Beasley, C. A.; Murray, R. W., Voltammetry and Redox Charge Storage Capacity of Ferrocene-Functionalized Silica Nanoparticles. *Langmuir* **2009,** *25* (17), 10370-10375.

15. Mikhaylova, M.; Kim, D. K.; Berry, C. C.; Zagorodni, A.; Toprak, M.; Curtis, A. S. G.; Muhammed, M., BSA Immobilization on Amine-Functionalized Superparamagnetic Iron Oxide Nanoparticles. *Chem. Mater.* **2004,** *16* (12), 2344-2354.

16. del Campo, A.; Sen, T.; Lellouche, J.-P.; Bruce, I. J., Multifunctional magnetite and silica–magnetite nanoparticles: Synthesis, surface activation and applications in life sciences. *J. Magn. Magn. Mater.* **2005,** *293* (1), 33-40.

17. White, M. A.; Johnson, J. A.; Koberstein, J. T.; Turro, N. J., Toward the Syntheses of Universal Ligands for Metal Oxide Surfaces: Controlling Surface Functionality through Click Chemistry. *J. Am. Chem. Soc.* **2006,** *128* (35), 11356-11357.

18. Peng, R.; Zhang, W.; Ran, Q.; Liang, C.; Jing, L.; Ye, S.; Xian, Y., Magnetically Switchable Bioelectrocatalytic System Based on Ferrocene Grafted Iron Oxide Nanoparticles. *Langmuir* **2011,** *27* (6), 2910-2916.

19. Moses, J. E.; Moorhouse, A. D., The growing applications of click chemistry. *Chem. Soc. Rev.* **2007,** *36* (8), 1249-1262.

20. Harper, G. B., Reusable glass-bound pH indicators. *Anal. Chem.* **1975,** *47* (2), 348-351.

21. Noel, S.; Liberelle, B.; Robitaille, L.; De Crescenzo, G., Quantification of Primary Amine Groups Available for Subsequent Biofunctionalization of Polymer Surfaces. *Bioconjugate Chem.* **2011,** *22* (8), 1690-1699.

22. Bacci, M.; Baldini, F.; Bracci, S., Spectroscopic Behavior of Acid-Base Indicators After Immobilization on Glass Supports. *Appl. Spectrosc.* **1991,** *45* (9), 1508-1515.

23. Haensch, C.; Hoeppener, S.; Schubert, U. S., Chemical modification of self-assembled silane based monolayers by surface reactions. *Chem. Soc. Rev.* **2010,** *39* (6), 2323-2334.

24. Stiles, R. L.; Balasubramanian, R.; Feldberg, S. W.; Murray, R. W., Anion-Induced Adsorption of Ferrocenated Nanoparticles. *J. Am. Chem. Soc.* **2008,** *130* (6), 1856-1865.

25. Wuelfing, W. P.; Templeton, A. C.; Hicks, J. F.; Murray, R. W., Taylor Dispersion Measurements of Monolayer Protected Clusters: A Physicochemical Determination of Nanoparticle Size. *Anal. Chem.* **1999,** *71* (18), 4069-4074.

26. Faulkner, A. J. B. a. L. R., *Electrochemical Methods: Fundamentals and Applications*. 2nd ed.; John Wiley & Sons, Inc.: Phoenix, Az, 2001.

CHAPTER 5 – ELECTROCHEMICAL EVALUATION OF <10 NM CITRATE CAPPED MAGNETITE NANOPARTICLES

5.1 Introduction

Magnetic iron oxide nanoparticles and solutions thereof have experienced interest in the nanomaterials field, having potential technological applications like data storage and improved electronic devices[1]. They are an active topic in medical areas[2-4] given their limited toxicity[5-6], finding use in MRI contrast reagents[7-8], as bio-molecule tags[9-11], for targeted hypothermia treatments[7], and even targeted drug delivery. Magnetite also sees uses in areas such as in ferrofluids for seals and oscillation dampening[12-13]. Among different forms of iron oxides, particles of magnetite (Fe_3O_4) have seen emphasis in such applications.

Magnetite nanoparticles can be prepared in the 4-5 nm diameter range and are soluble in aqueous citrate buffer solutions containing added $NaClO_4$ electrolyte. They display transport-controlled linear sweep and rotated disk voltammetries in chemically irreversible waves that are well-separated (ca. 0.3 V) on the potential axis, corresponding to the two different Fe(III/II) reactions of the nanoparticles. While electrochemistry of iron oxides as films on surfaces has been previously investigated, this is the first report on voltammetry of freely diffusing nanometer scale Fe_3O_4 nanoparticles.

Iron oxide nanoparticles that are viable for biological application need to be smaller than *ca*. 20 nm and have a small l size dispersity (typically <10%)[14], which generally improves

reproducibility in highly sensitive measurements. These small nanoparticles are commonly prepared by an aqueous co-precipitation using $Fe^{II}Cl_2$ and $Fe^{III}Cl_3$ salt mixtures in the presence of a base (such as NaOH or NH_3)[8, 15-17], hydrothermal reactions[18-19], or by electrochemical generation from sacrificial iron electrodes[20-21]. It can be difficult, however, to control the average size, and dispersity, of < 20 nm iron oxide nanoparticles obtained by these approaches. An alternative pathway relies on a non-aqueous high temperature thermal degradation reaction of an iron acetate or acetylacetonate salt with long chain compounds like oleylamine and/or oleic acid in a high boiling point solvent, near its boiling point (often > 260 ˚C). This procedure, although ungainly, reproducibly yields nanoparticle batches with tight size distribution (diameter variability ca. 10%) and bearing a fatty surfactant coating that stabilizes the nanoparticles and prevents aggregation. Control between spherical and cubic nanoparticle morphologies has even be demonstrated with this method[22]. This general procedure was introduced by Sun *et al.*[23] Additional metal acetylacetonates (such as those of Co, Ni, Mn) can be doped into the nanoparticles to manipulate their magnetism[24].

The high temperature thermal degradation synthesis for nanoparticles used in bio-applications brings the issue that their fatty capping makes them quite hydrophobic and potentially toxic. The fatty capping shell can be replaced however, with hydrophilic reagents based on silanes[8, 11, 17, 25-29], carboxylic acids[30], or phosphates[31-32], which for silanes interact covalently with the nanoparticle surfaces and by chemisorption in the case of carboxylic acids and phosphates[33]. These ligands often have specific functionalities allowing them to undergo further modification via coupling reactions (carbodiimide[16, 34], acyl chloride[35], or click[7, 32, 36-37] to address a small number) to adjust solubility and produce a wide variety of nanoparticle surface modifications.

Although magnetite nanoparticles have been employed in bio-sensing schemes, little is known about their electrochemical properties as freely diffusing nanoparticles. Most prior electrochemical analysis is either of bulk iron oxide materials[38] or hematite nanoparticles[39]. Marken *et. al.*[40] attempted to show electrochemistry of freely diffusing 4-5 nm hematite nanoparticles, but were limited by adsorption. Regardless, they still showed a pH dependent reduction of hematite and a stripping response of electrochemically formed $FePO_4$. Other electrochemical analyses of hematite nanoparticles evaluate their potential as capacitors, with the nanoparticles often being pressed into electrodes[19]. Magnetite bulk material does show electrochemisty in low pH solutions[38]. Magnetite nanoparticles have also seen electrochemical evaluation in electrode mixtures for battery applications[18]. The surfactant layers on non-aqueous soluble nanoparticles tend to act as barriers for electron transfers to/from them. In the present work, the original surfactant layer is therefore replaced by more manageable ligands that allow examination of the nanoparticle electrochemistry in aqueous media. The nanoparticle voltammetry is unusual in that the Fe_3O_4 magnetite nanoparticles exhibit reactions that are both formally Fe(II) → Fe (III) and Fe(III) → Fe(II) but with different apparent formal potentials.

5.2 Experimental

5.2.1 Chemicals and Materials

Iron (III) acetylacetonate ($Fe(acac)_3$; 97%), iron(III) citrate ($C_6H_5FeO_7$; technical grade), oleylamine ($C_9H_{18} = C_9H_{17}NH_2$; 80-90%), oleic acid ($C_9H_{18} = C_8H_{15}COOH$; 97%), 1,2-hexadecanediol($CH_3(CH_2)_{13}CHOHCH_2OH$; 90%), diphenyl ether ($(C_6H_5)_2O$; >99%), and sodium perchlorate ($NaClO_4$; >98%) were purchased from Sigma-Aldrich. Absolute ethanol, N,N-dimethylformamide (DMF), hexanes and toluene obtained from Fisher Scientific were dried over 4 A molecular sieves.

5.2.2 Instrumentation and Electrochemical Details

Cyclic Voltammetry (CV). CV was performed on a a CH Instruments model CHI660a and CHI760c with a Pine Instruments rotator (Model AFMSRCE) with Pt working electrode (0.02 cm^2 disk, or 0.196 cm^2 for rotating disk), Pt mesh counter electrode, and Ag/AgCl/3 M KCl (aq) reference electrode in solutions of pH 2.2 citrate buffer with added 1 M $NaClO_4$ electrolyte.

The electrochemical cell for magnetic electrochemical experiments comprised (Scheme 5.18) two main components 1) Teflon boyd (inner dia. 2.5 cm) that holds ~ 20 mL of solution, 2) acrylic bottom that screws onto the body to clamp the working electrode (Pt slide) into place. Where the Teflon body meets the acrylic bottom is a cavity which holds a silicone O-ring (inner dia 0.368 ± 0.013 cm) producing a fixed working electrode area of 0.106 ± 0.0075 cm^2.

Programmable Temperature Control Unit. A lab constructed device controlled by a CAL 9500P programmable process controller with attached to a thermal couple was used to accurately control synthesis temperatures.

High Resolution Transmission Electron Microscopy (TEM). TEM images were obtained on a JEOL 2010F FasTEM on nanoparticle samples prepared on copper grids (200 carbon mesh, carbon-coated Formvar; Ted Pella, Redding, CA)

Energy-Dispersive X-Ray Spectroscopy (EDS). EDS analysis was performed using Oxford INCA EnergyTEM 250 TEM microanalysis system attached to the JEOL 2010F FasTEM.

Centrifuge. Centrifugation was done with an Eppendorf 5810 centrifuge with a fixed-angle rotator at 3000-4000 rpm for 10 minutes.

pH Measurement. pH measurements were performed with a Corning pH meter 445.

X-Ray Photoelectric Spectroscopy (XPS). XPS data were taken on a Kratos Axis Ultra DLD system with monochromatic Al Kα x-ray source. High resolution scans were taken at pass energy = 20 eV, and the spectral energy axis was aligned at the C 1s peak at 284.6 eV.

X-Ray Diffraction (XRD). XRD data were taken on a Rigaku Multiflex powder diffractometer with Cu K-alpha radiation.

Ultraviolet-Visible Spectroscopy (UV-Vis). UV-Vis spectra were taken on a Thermo Evolution Array UV-Vis spectrophotometer (Thermo, Waltham, MA)

5.2.3 Synthesis of 4 nm Magnetite Nanoparticles.

The procedure was similar to that of a previous report[24]. 0.49 g $Fe(acac)_3$ (2 mmol), 1.5 mL oleic acid (6 mmol), 1.3 mL oleylamine (6 mmol), and 2.58 g 1,2-hexadecanediol (10 mmol) were added to 20 mL diphenyl ether in a round bottom flask equipped with a magnetic stir bar, thermocouple and condenser. Using a 100 mL heating mantle packed with sand to promote even heating, the vessel was argon purged and heated for 30 min. at 200˚C with vigorous stirring. The temperature was then rapidly increased to 265˚ C; the solution color changed from dark red to black signaling formation of magnetite nanoparticles. The reaction was refluxed at 265˚C for an hour and allowed to cool to room temperature. The black suspension was transferred to centrifugation tubes and absolute ethanol added to precipitate the nanoparticles which were collected by centrifugation at 6000 RPM for 10 minutes. After repeating this process three times to wash the nanoparticles, they were taken up into 10 mL of hexanes solvent and stored at room temperature. The nanoparticles produced had average dia. 4.4 ± 0.9 nm, as shown in the TEM of Figure 1.

5.2.4 Citrate Capped Magnetite Nanoparticles.

Modified from Drofenik *et. al.*[41] A 1 mL sample of the hexane solution of nanoparticles was rotovapped to dryness and the nanoparticles weighed (~5 mg) and redissolved in 7.5 mL toluene in a scintillation vial. The toluene solution was added to a solution of citric acid (3 mmol, ~0.6 g) in 7.5 mL DMF (e.g., 5 mg citric acid per 5 mg magnetite NPs) which became a turbid brown. The mixture was stirred vigorously at 100 ˚C for 24 hrs, then was transferred to 50 mL centrifuge tubes and the nanoparticles precipitated by adding diethyl ether. They were collected via centrifugation at 6000 RPM for 10 minutes. The red-brown nanoparticle precipitate was washed twice more with fresh diethyl ether and then suspended in 15 mL of pH 2.2 citrate buffer; after 24 hr this yields a homogeneous, yellow solution.

5.3 Results and Discussion

5.3.1 Fe_3O_4 Nanoparticle Synthesis and Characterization.

The produced Fe_3O_4 nanoparticles are 4.4 ± 0.9 nm dia. and readily dissolve in nonpolar solvents (hexanes, toluene, chloroform), forming black solutions that are brownish when highly diluted. At high concentrations they display ferrofluidic behavior (*vide infra*). The nonpolar character of the nanoparticles is attributable to their fatty surfactant coating, which prevents aggregation and flocculation. In TEM images, the nanoparticles (Fig. 5.1) show lattice lines indicating their crystalline nature. The lattice is spaced by ~3Å, corresponding to (220) planes in spinel-structured magnetite[24]. X-ray powder diffraction (XRD) of the nanoparticles (Fig. 5.2) also hints at their crystalline nature, but does not fully agree with previously reported diffraction patterns of magnetite nanoparticles[24]. The UV/Vis spectra of these nanoparticle solutions show strong absorbance in the UV, with several small shoulders at 275 nm, 346 nm, and 480 nm (Fig. 5.3a). The molar absorptivity, in terms of nanoparticle concentration and iron concentration, is

listed in Table 5.1. Optical excitation at 350 nm results in emission peaks at 400 nm and 425 nm and a shoulder at ca. 450 nm (Fig. 5.4). The XPS spectrum of the nanoparticles (Fig. 5.5) is nearly featureless and shows only a strong C 1s peak owing to the dominating surfactant coating, as seen previously for ITO nanoparticles[35]. Electrochemistry of the as-synthesized nanoparticles is featureless, due to the insulating surfactant coating which acts as a barrier to electron transfers.

5.3.2 Surfactant Replacement.

In order to electrochemically access the nanoparticle core, the surfactant coating needed to be replaced. Carboxylic acids and phosphates are known to interact with metal oxide surfaces and to bind to large magnetite particles[33]. Citric acid was found to be a more convenient capping agent.

The citrate capped nanoparticles (abbrev. Cit Fe_3O_4) form a stable, cloudy red-brown suspension immediately after ligand replacement. (They show reduced magnetism as compared to as-synthesized magnetite nanoparticles, but do respond (*vide infra)* to the presence of a magnetic field.) For electrochemical experiments, the suspension was adjusted to pH 2.2 using citric acid; after 24 hr it becomes a yellow, fully dispersed solution. (This color contrasts to the blackish color of as-synthesized magnetite nanoparticle solutions.) TEM images (Fig 5.6) show no change in the size of the nanoparticles after citrate capping, though a small amount of flocculation often occurs in handling these samples. The absorbance spectrum of the Cit Fe_3O_4 shows a significant decrease in the number of shoulders and the appearance of a very broad shoulder at ca. 270 nm (Fig. 5.3b). Molar Absorptivity is presented in Table 1. Cit Fe_3O_4

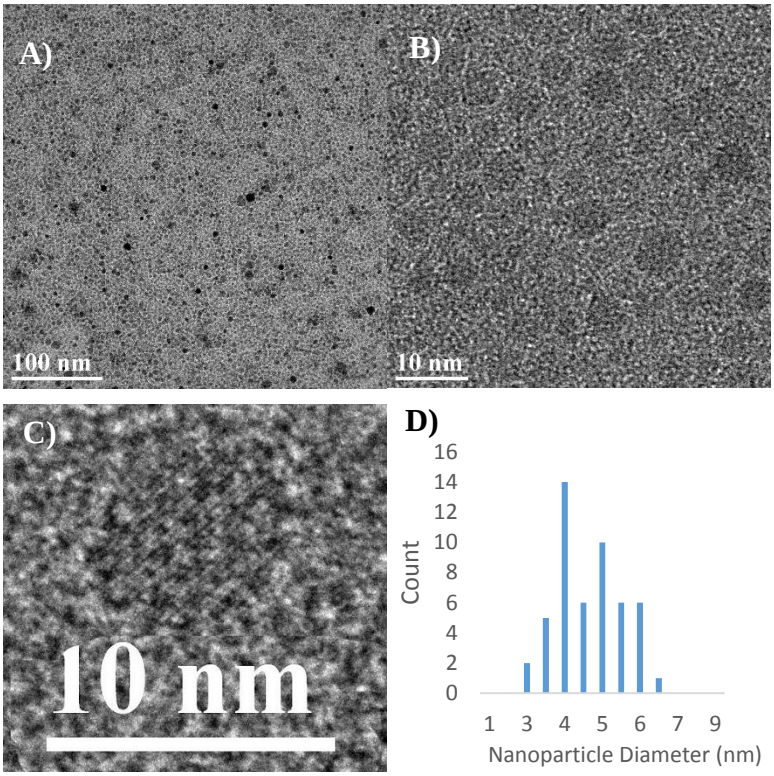

Figure 5.1 - TEM images of as-synthesized magnetite nanoparticles. Scale bar panel A) 100nm; B) 10nm. Panel C) image shows lattice lines of an individual nanoparticle; Panel D) shows a histogram of magnetite nanoparticle diameters (n = 100) indicating an average dia. of 4.4 ± 0.9 nm.

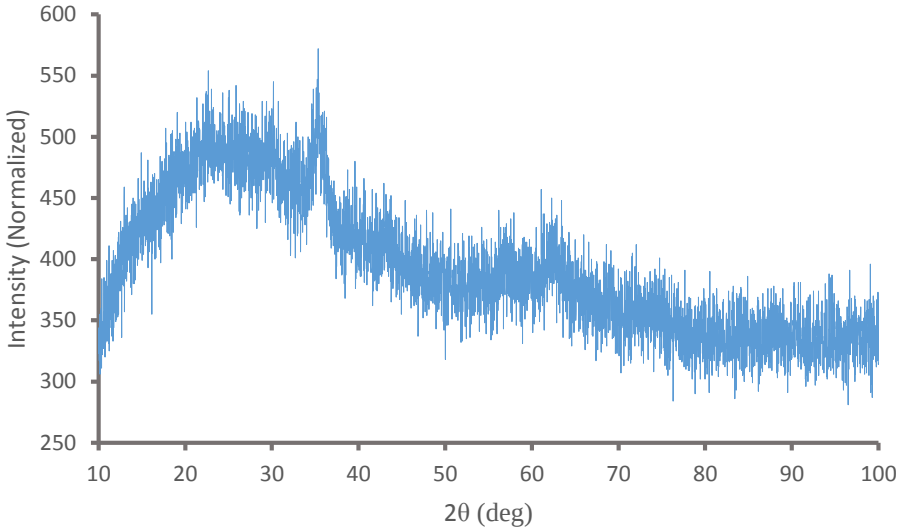

Figure 5.2 – XRD of magnetite nanoparticles

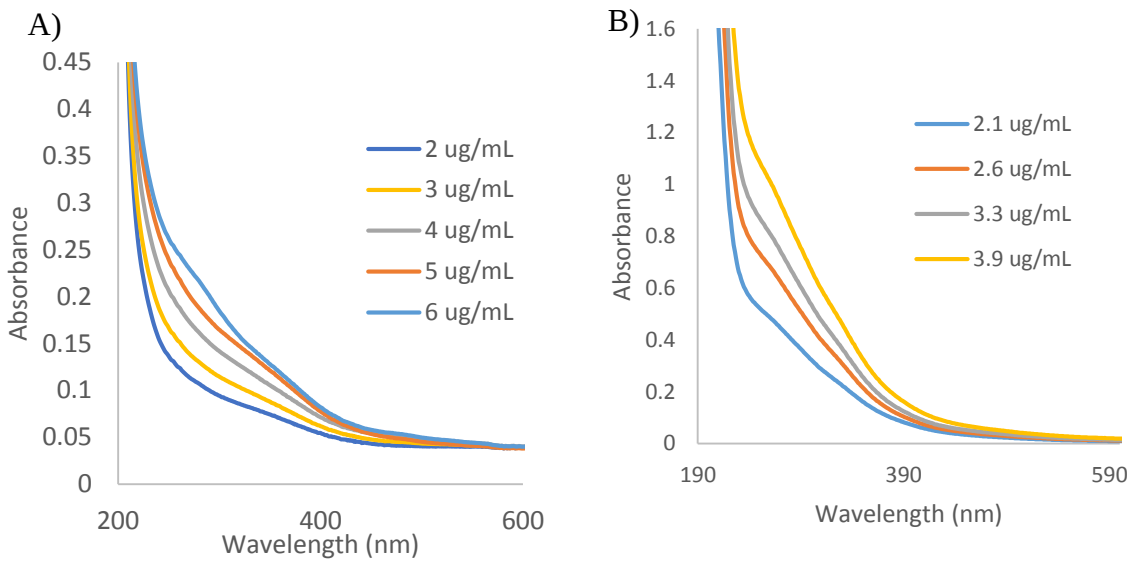

Figure 5.3 – UV/Vis spectrum of a) the concentration dependence of 6 µg/mL magnetite nanoparticles in hexanes solvent and b) the concentration dependence of a solution of 3.9 µg/mL Cit Fe_3O_4 in water.

Table 5.1 – Reported molar absorptivities for Fe_3O_4 and Cit Fe_3O_4 in terms of nanoparticles and iron concentration.

Sample Name	**λ (nm)**	**ε (cm^{-1} Fe M^{-1})**
Fe_3O_4	275	2220
Cit Fe_3O_4	270	21600

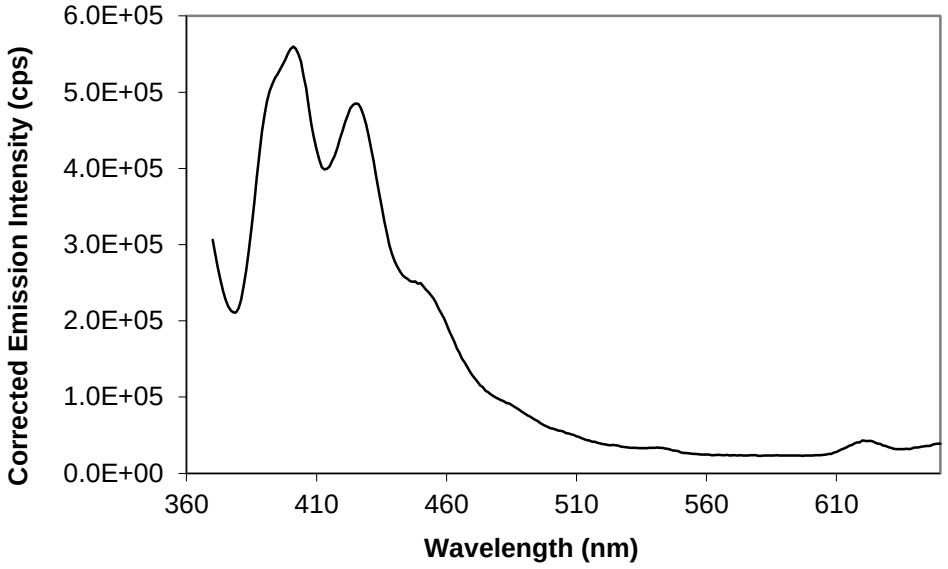

Figure 5.4 – Emission spectra of magnetite nanoparticles; excited at 350 nm. Concentration ca. 6 µg/mL

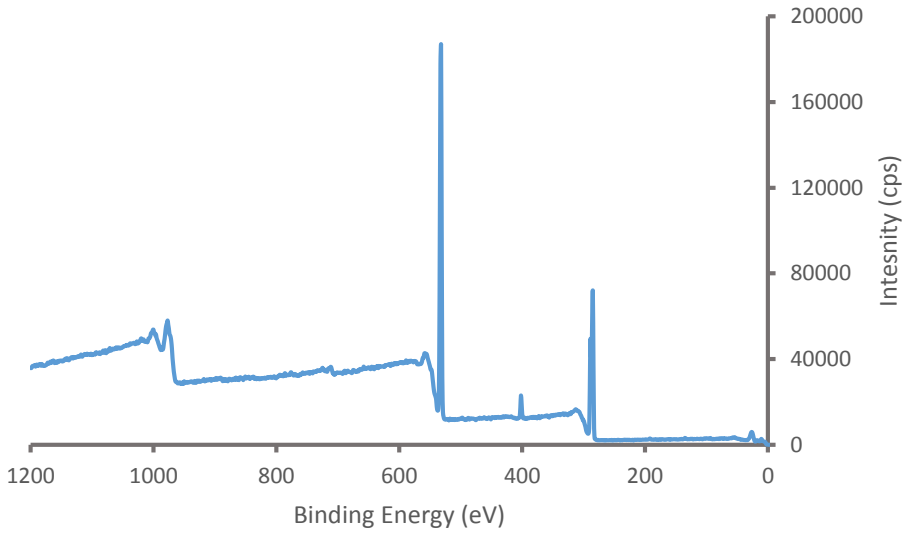

Figure 5.5 - XPS of as synthesized (surfactant capped) magnetite nanoparticles.

nanoparticles do not show the photoluminescence seen for the as-synthesized nanoparticles, whether this is traceable to the surfactant coating was not ascertained. The XPS spectrum (Fig. 5.7) now shows a less prominent C 1s peak (due to the thinning or removal of the surfactant layer) and a doublet of peaks corresponding to the Fe 2p electrons at 709 eV and 722 eV.

5.3.3 Electrochemistry of Solutions of Citrate-Capped Magnetite Nanoparticles.

Voltammetry of the Cit Fe_3O_4 nanoparticles was carried out in degassed pH 2.2 citric acid buffer with added 1 M $NaClO_4$ electrolyte. Both an oxidation and a reduction wave are seen (Fig 5.8). These waves should not be regarded as a single redox process with a large peak splitting, but are instead different reactions—an irreversible oxidation process with E_{PEAK} ca. 0.520 V and an irreversible reduction process with E_{PEAK} ca. 0.130 V. This is evidenced by noting that the open circuit solution rest potential (ca. 0.36 vs Ag/AgCl) lies between the two waves, consistent with the presence of both Fe(III) nanoparticle sites and Fe(II) nanoparticle sites in the solution, as expected for electrode reactions of Fe_3O_4 magnetite nanoparticles.

The oxidation wave is well defined on Pt electrodes while observation of the reduction wave at this pH is complicated by overlap with reduction of PtO_2 formed in the oxidation scan (Fig 5.9). (Experiments on Au electrodes (Fig 5.10) proved to be even less well defined.) Background subtraction was used to eliminate the PtO_2 overlap and simplify the investigation of the redox moiety. The pH appears to play a significant role in the electrochemistry of the Cit FeO nanoparticles (Fig 5.11). The nanoparticle oxidation current is sensitive to pH, decreasing significantly to background current levels at pH > 4.

The magnetite nanoparticle couple is very similar to that of Fe(III) citrate under the same conditions (Fig 5.12), though the OCP of Fe(III) citrate was higher (0.473 V) due to the dominance of the Fe(III) form.

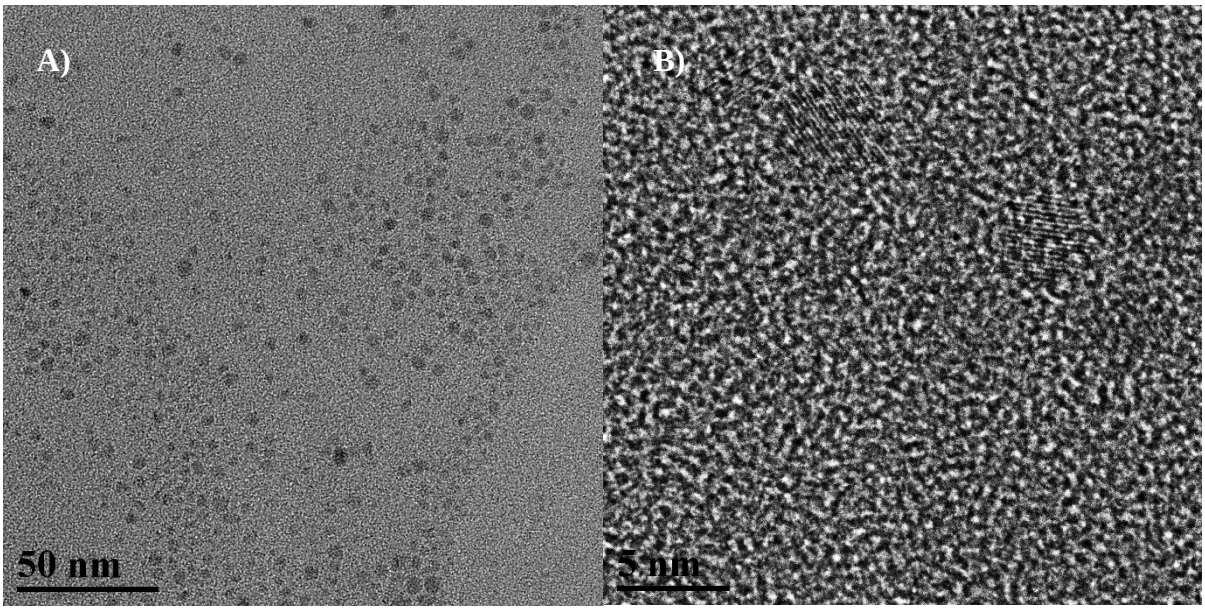

Figure 5.6 – TEM images of Cit Fe_3O_4 nanoparticles. Scale bar panel A) 50 nm. Panel B) 5 nm image shows lattice lines of an individual nanoparticle.

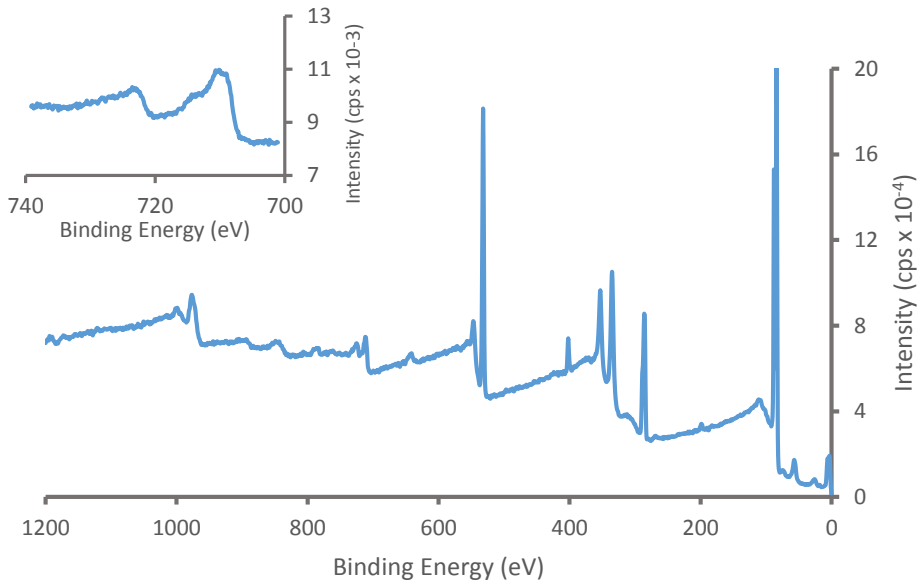

Figure 5.7 – XPS of citrate-capped magnetite nanoparticles. Inset depicts the Fe 2P region.

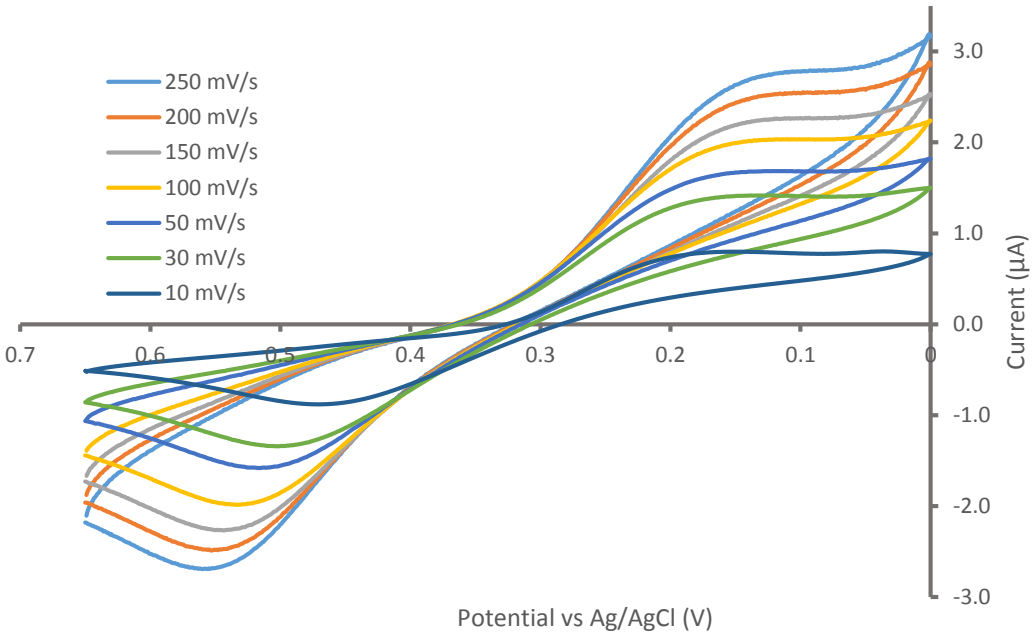

Figure 5.8 – Background-subtracted cyclic voltammetry of 12 mM citrate capped magnetite nanoparticle solution in pH 2.2 citrate buffer, with added 1 M $NaClO_4$ electrolyte, at varying potential scan rates

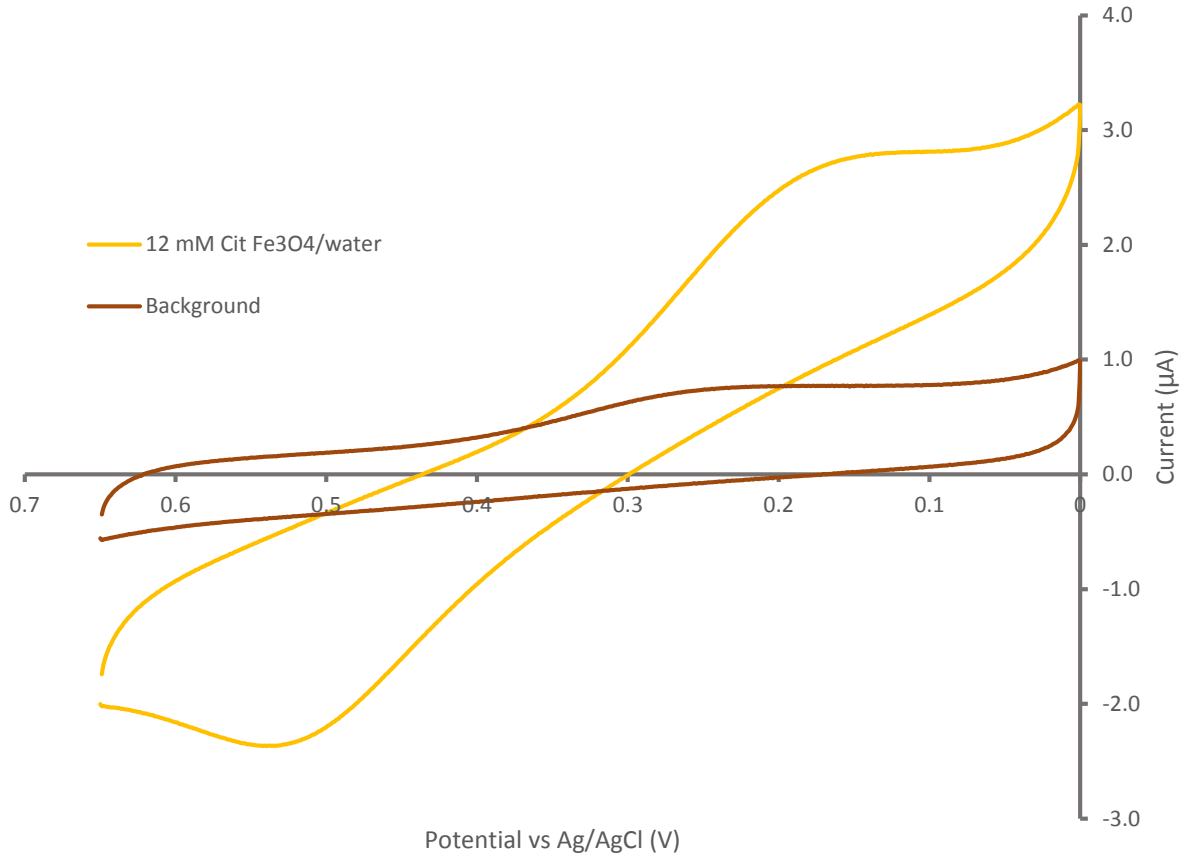

Figure 5.9 – Comparison between cyclic voltammetry of 12 mM citrate capped magnetite nanoparticles/water in pH 2.2 citrate buffer with added 1 M $NaClO_4$ electrolyte and the Pt disk background at 100 mV/s

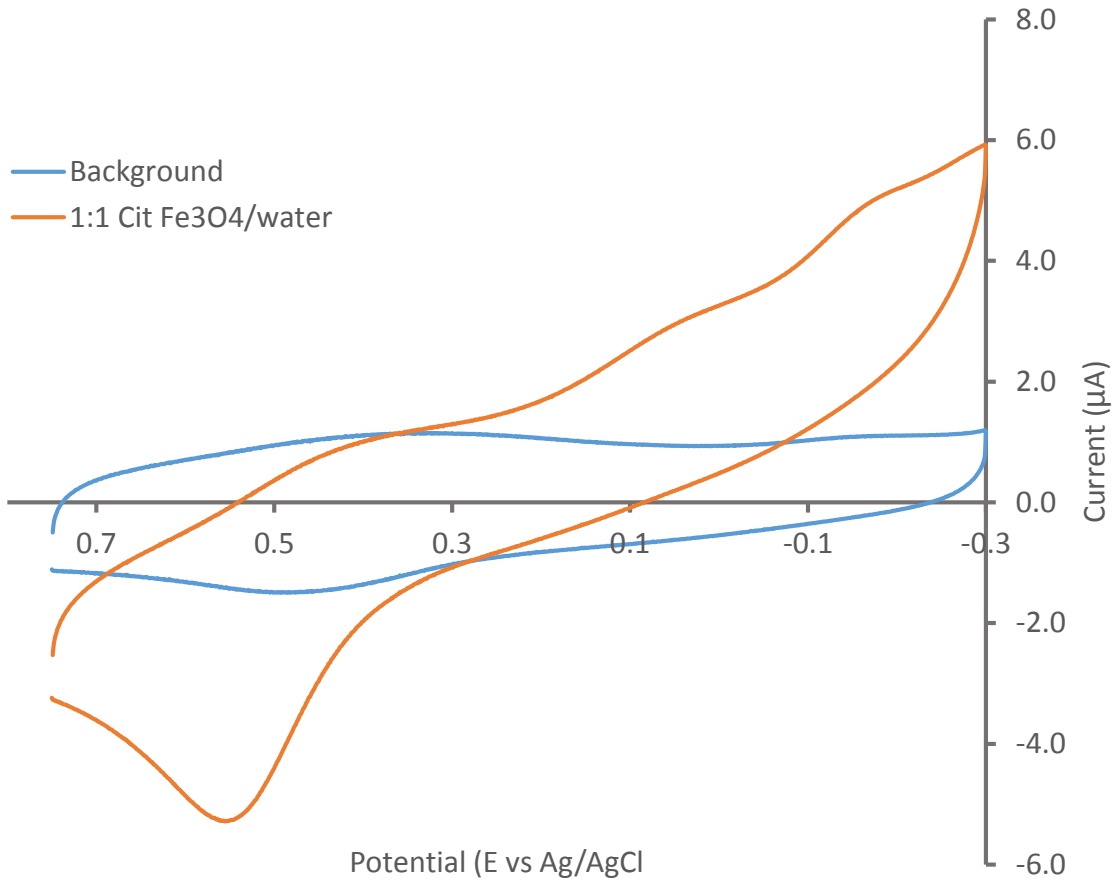

Figure 5.10 – Comparison between cyclic voltammetry of a 12 mM citrate capped magnetite nanoparticles/water in pH 2.2 citrate buffer with added 1 M $NaClO_4$ electrolyte and the Au disk background at 100 mV/s

Bulk electrolysis (BE) was also used to determine the concentration of Fe^{3+} in solutions of Cit Fe_3O_4 nanoparticles in pH 2.2 citrate buffer with 1 M $NaClO_4$ for later use in calculating diffusion coefficients. These experiments were very slow, taking ca. 1-2 hrs. for 99% electrolysis. A similar timeframe was observed for BE of Fe(III) citrate under similar conditions. This is likely due to poor electron transfer kinetics.

A plot of current vs. square root of potential scan rate (Fig 5.13) was used to examine the diffusional character of these nanoparticle electrochemical waves. The equation for linear sweep voltammetry[42] is

$$i_p = 2.99 * 10^5 \alpha^{1/2} n^{3/2} A D^{1/2} C v^{1/2} \quad (1)$$

where n is the number of electrons delivered (per iron site), A the area of the working electrode (cm^2), D (cm^2/s) the nanoparticle diffusion coefficient and C (mol/cm^3) is the overall concentration of active iron sites. The expected linear relation between the peak currents and the square root of potential scan rate ($v^{1/2}$) is observed (Fig. 5.13), showing that the currents being controlled by the rate of nanoparticle diffusion. (While Equation (1) is for an irreversible redox system, a $v^{1/2}$ scan rate dependency is also expected for quasi- and reversible reactions.) Strong adsorption is not involved in the electrode reactions—at least no residual redox peaks are observed after moving the electrode to a fresh electrolyte solution. Additional experiments, namely chronoamperometry and rotating disk electrochemistry, were used to examine the nanoparticle reaction.

The nanoparticle electrochemistry is examined by rotating disk voltammetry (RDE) in Figure 5.14, which was taken in a 1:4 solution of the Cit Fe_3O_4 nanoparticles/water in pH 2.20 citrate buffer with 1 M $NaClO_4$. Without background correction, the reduction wave does not

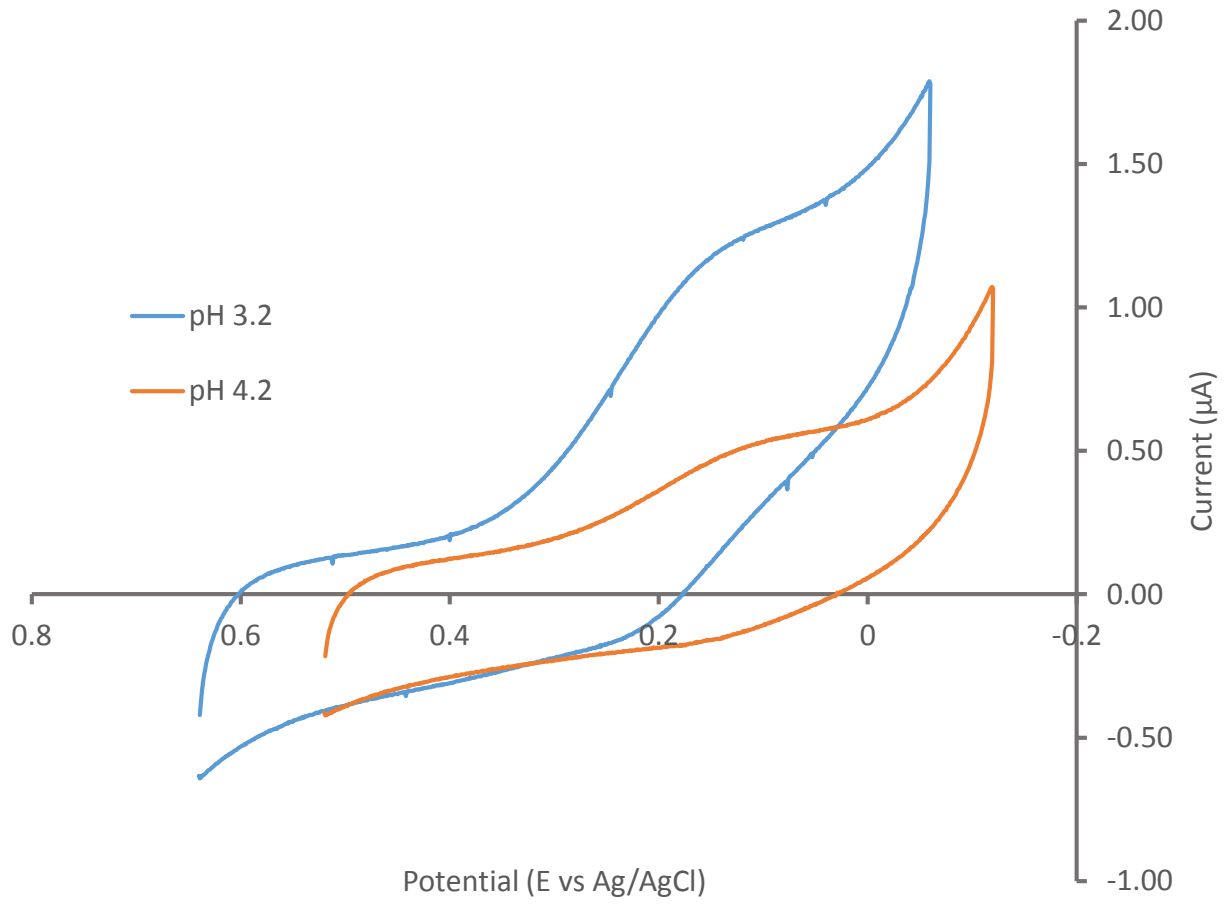

Figure 5.11 – Cyclic voltammetry of 215 µM citrate capped magnetite nanoparticles/water in citrate buffer with added 1 M $NaClO_4$ electrolyte, at varying pH values.

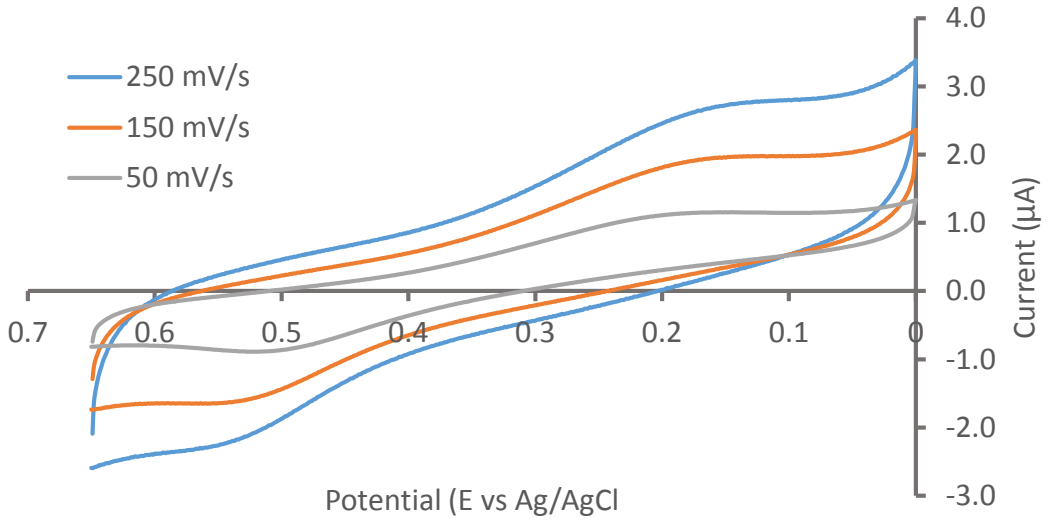

Figure 5.12 – Cyclic voltammetry of 1 mM Fe(III) citrate in pH 2.2 citrate buffer with added 1 M $NaClO_4$ electrolyte.

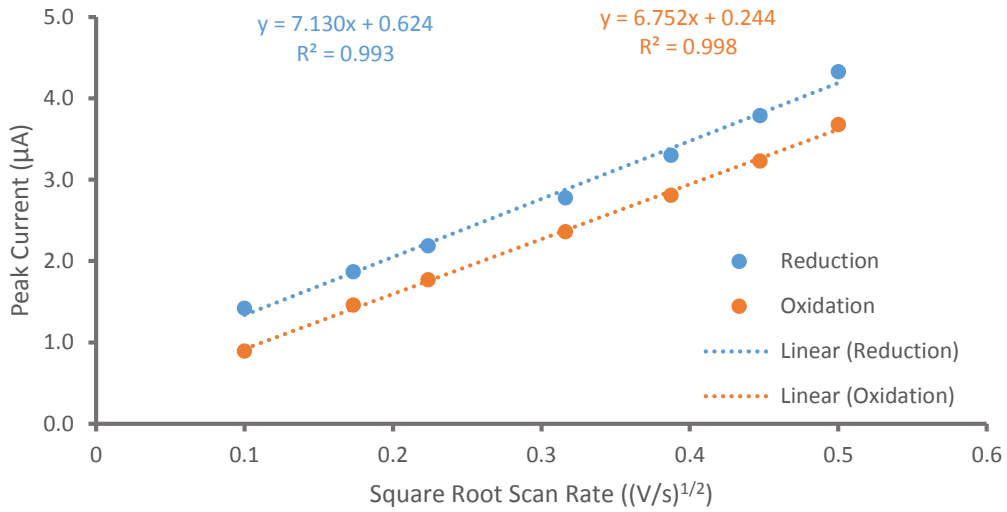

Figure 5.13 – Potential sweep rate dependence of (background currents subtracted) cyclic voltammetry of a 12 mM citrate capped magnetite nanoparticle/water solution in pH 2.2 citrate buffer with 1 M $NaClO_4$. Both waves are well fit by a [scan rate]$^{1/2}$ dependency

show a well-defined steady-state plateau, but after background subtraction the reduction steady state plateau becomes visible. Limiting currents taken from the reduction plateau at 0.36 V to the oxidation plateau at 0.6 V follow (Fig 5.15) the rotation rate square root relationship predicted by the Levich equation[42]

$$i_l = 0.62\, nFACD^{2/3}\omega^{1/2}v^{-1/6} \qquad (2)$$

where F is Faraday's constant, ω is angular rotation rate (radians/sec), and υ is the kinematic viscosity (cm^2/s). Concentration and diffusion coefficients from this experiment are listed in Table 5.2.

For potential step chronoamperometry (CA) with steps to the reduction plateau, currents are less affected by the poor electron transfer kinetics of the system and should follow a normal Cottrell relationship[42].

$$i(t) = nFAC\left(\frac{D}{\pi t}\right)^{1/2} \qquad (3)$$

Figure 5.16 shows a Cottrell plot where current is measured out to 12 s; its linearity supports a picture of diffusion-controlled reduction of the nanoparticles. A comparison of the diffusion coefficients determined by this technique are listed in Table 5.2. A Tafel plot[42] was constructed to evaluate the kinetics of the two irreversible reactions of Cit Fe_3O_4 (Fig 5.17). Important values can be found in Table 5.3. The overpotential,η, was taken to be Even though the reactions are being treated as two individual irreversible reactions, they both have very similar kinetic behavior. Transfer coefficients, α, are between 0.4 - 0.5 indicating relative symmetry between the oxidation and reduction energy barriers. The standard rate constants, k^0, differ by less than a factor of two even though the measured rate is slow (1×10^{-5} cm/s).

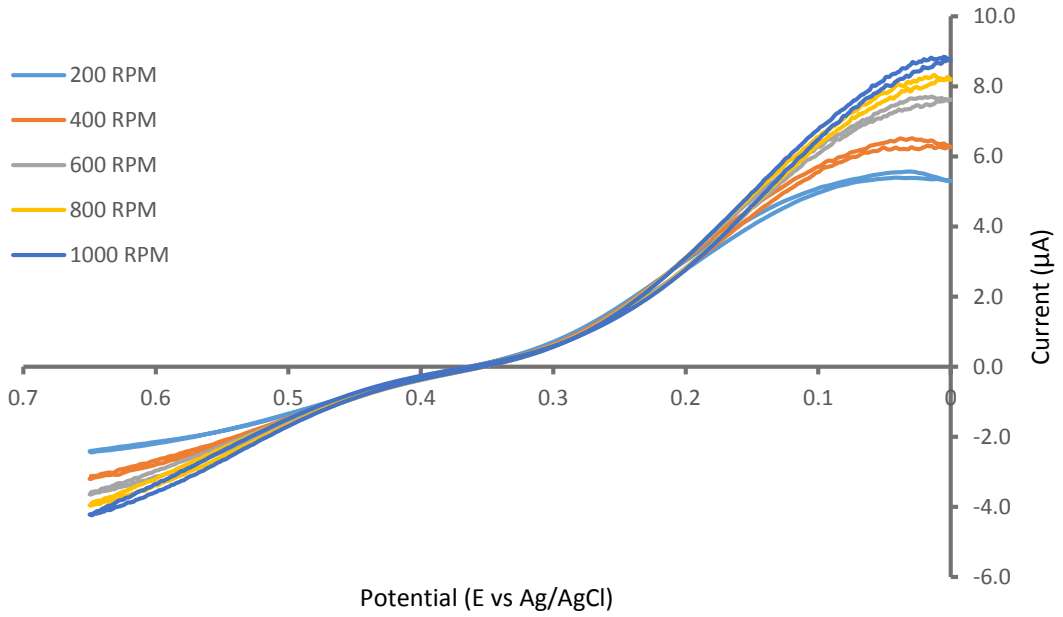

Figure 5.14 – Background-subtracted rotating disk electrode voltammetry (potential scan rate 10 mV/s), at different rotation rates, of a 5 mM solution of citrate capped magnetite nanoparticles in pH 2.2 citrate buffer with 1 M $NaClO_4$.

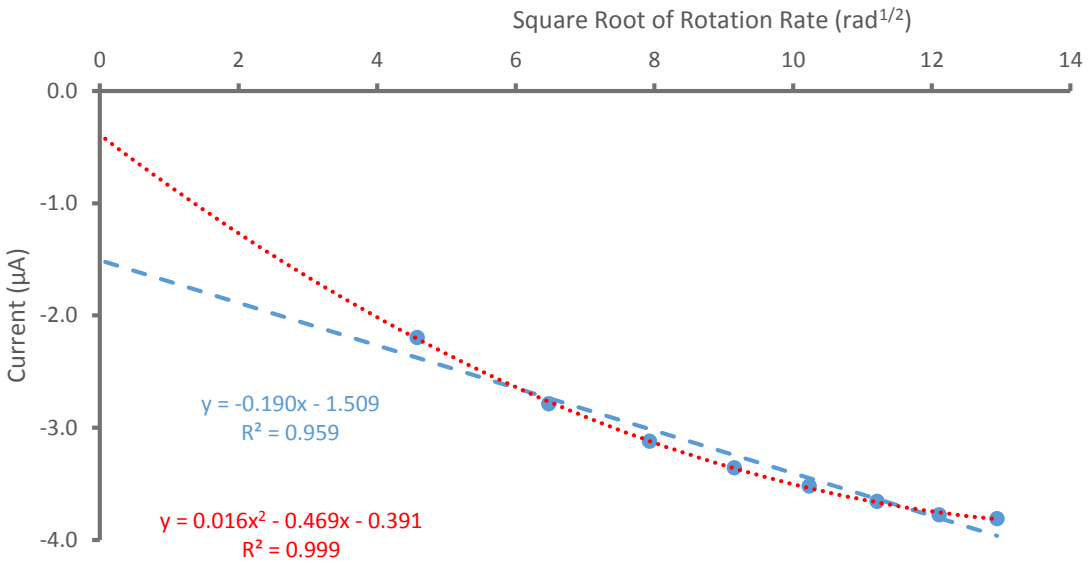

Figure 5.15 – Levich plot of background -subtracted RDE oxidation limiting currents (taken at 0.36 V and 0.6 V vs Ag/AgCl) for 5 mM solution of citrate capped magnetite nanoparticles/water, in pH 2.2 citrate buffer with 1 M $NaClO_4$. A clear curvature is observed that shows an strong x^2 correlation.

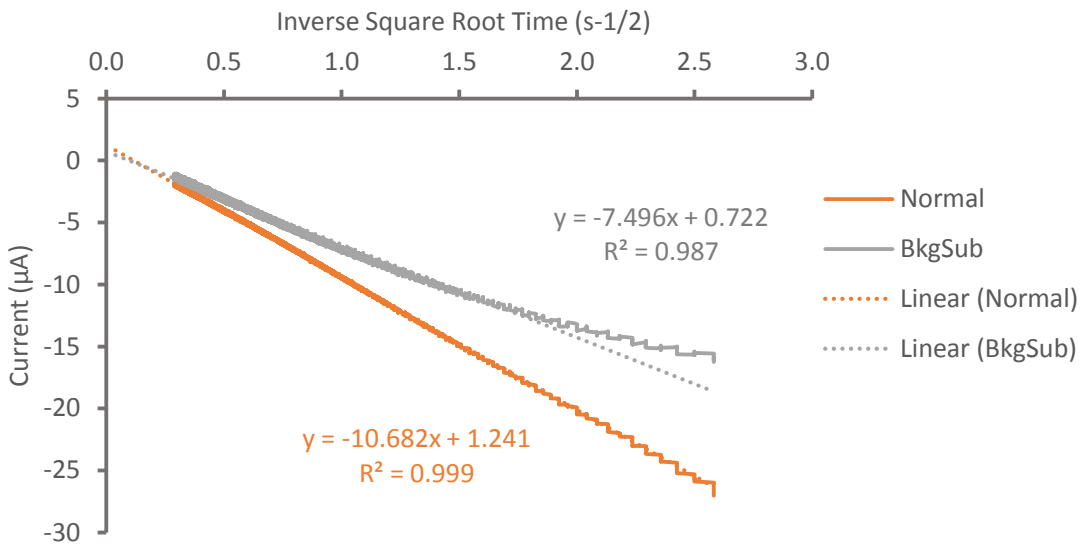

Figure 5.16 – Cottrell plot of chronoamperometric oxidation currents over a 12 second timescale for a potential step to from 0.347 V to 0.700 V vs. Ag/AgCl for the 5 mM solution of citrate capped magnetite nanoparticles in pH 2.20 citrate buffer with 1 M $NaClO_4$.

Table 5.2 – Concentration of varying solutions of Cit Fe_3O_4 nanoparticles in pH 2.2 citrate buffer with 1 M $NaClO_4$ samples based on bulk electrolysis and their associated diffusion coefficient values calculated based on technique. The letter represents sample batches while the number represents the dilution %.

Sample Name	**Technique**	**Concentration (µM)**	**Diffusion Coefficient (10^{-6} cm^2/s)**
Stokes-Einstein	-	-	1.1
Cit Fe_3O_4 – A50	CA	3650	1.8
Cit Fe_3O_4 – A20	CA	1300	1.3
	RDE		2.1
Cit Fe_3O_4 – A10	CA	650	3.7
Cit Fe_3O_4 – B50	CA	220	6.8
Cit Fe_3O_4 – B30	CA	130	7.9
Cit Fe_3O_4 – B10	CA	43	1.9
Average	-	-	3.6 ± 2.5

5.3.4 Effects of Magnetic Field on Magnetite Electrochemisty.

That the inherent magnetism of the magnetite nanoparticles is preserved for the described materials is shown by placing a Pt coated glass slide electrode at the bottom of a small cell (Fig 5.18). The cell was filled with a fresh pH 2.20 Cit FeO dispersion (prior to the 24 hr. aging step) with added 1 M $NaClO_4$ electrolyte. CV scans were taken of the nanoparticles without any magnetic field. Then, a magnetic field was placed under the working electrode to draw the magnetite nanoparticles to its surface. This showed no effect for several cyclical potential scans but after ~1 minute a significant accumulation of nanoparticles could be seen on the electrode surface. The change in current is most noticeable at slow potential scan rates (Fig 5.19). It is important to note that the fresh nanoparticle dispersion remains in solution for ca. 1 hr. without the external influence of a magnet.

5.4 Acknowledgments

This research was supported in part by the Office of Naval Research and the National Science Foundation. We gratefully acknowledge TEM, EDX, and XPS measurements performed by Carrie Donley and Amar Kumbhar of the Analytical and Nanofabrication Laboratory of the UNC Institute for Advanced Materials. We also acknowledge the UNC EFRC (Solar Fuels and Next Generation Photovoltaics, and Energy Frontiers Research Center funded by the U.S. Department of Energy, Office of Science, Office of Basic Energy Science under Award Number DE-SC0001011) and the UNC SERC ("Solar Energy Research Center Instrumentation Facility" funded by the Department of Energy – Office of Energy Efficiency & Renewable Energy under Award Number DE-EE0003188).

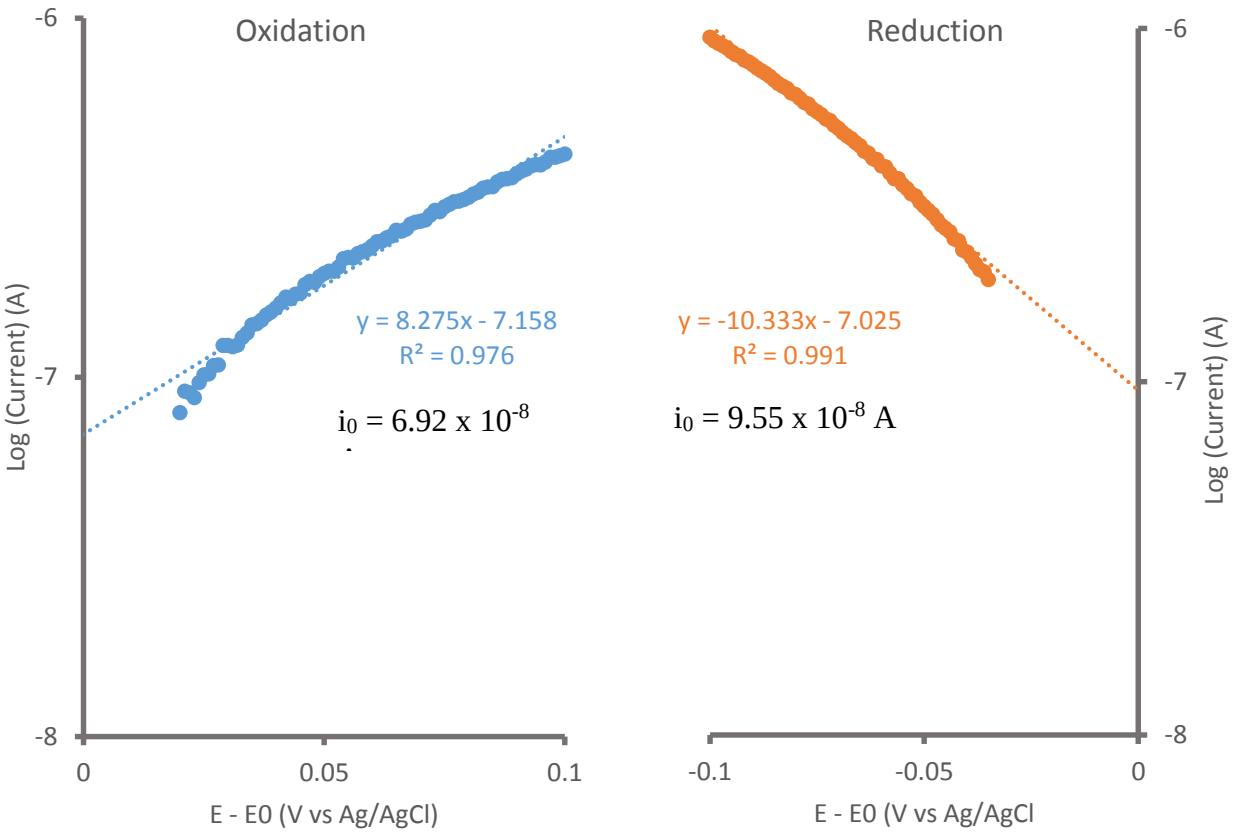

Figure 5.17 – Tafel plots depicting the irreversible oxidation of Fe^{3+} and the irreversible reduction of Fe^{2+}. The y-intercept is taken to be $\log(i_0)$, where i_0 is the exchange current.

Table 5.3 – Exchange current values and their comparative standard rate constants for both oxidative and reductive processes in Cit Fe_3O_4.

Cit Fe_3O_4 Process	**i_0 (A)**	**α (mol/V)**	**k^0 (cm/s)**
Oxidation	6.92×10^{-8}	0.481	1.1×10^{-5}
Reduction	9.55×10^{-8}	0.402	1.9×10^{-5}

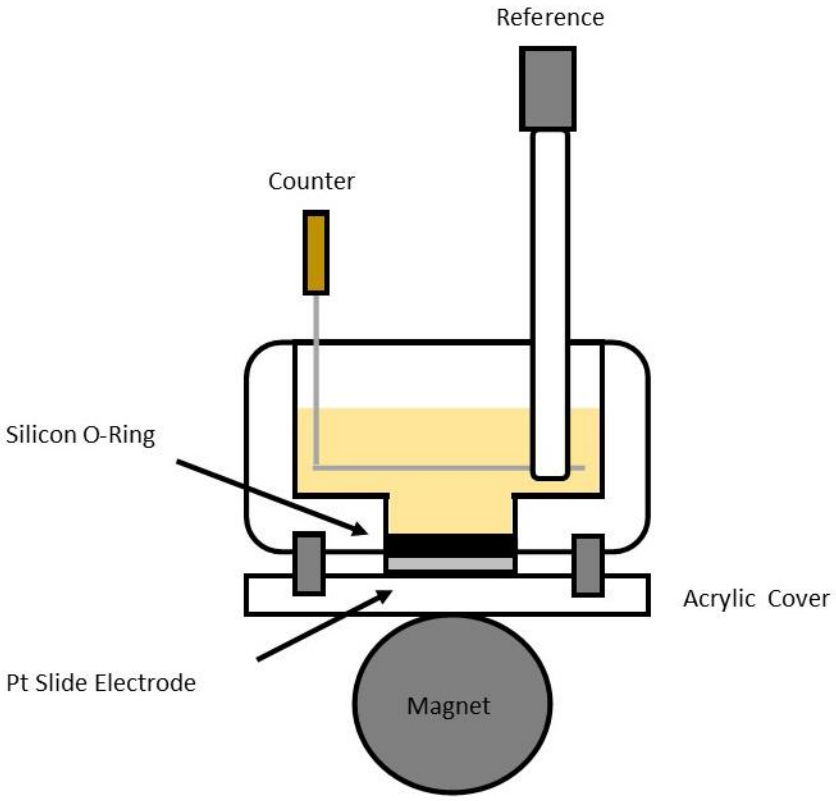

Figure 5.18 – Diagram of magnetic electrochemistry experiment setup. The inner diameter of the silicon O-ring is used as the working electrode area. The acrylic cover is attached tightly to form a seal between the WE and the O-ring.

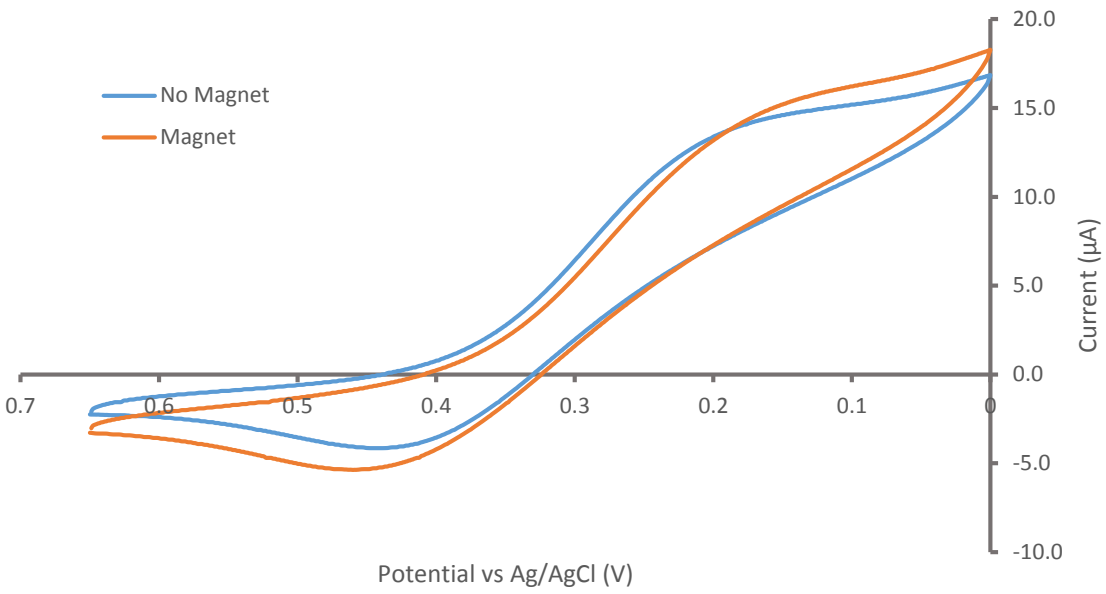

Figure 5.19 – Cyclic voltammetry of a 12 mM solution of citrate capped magnetite nanoparticles in pH 2.2 citrate buffer with 1 M $NaClO_4$ at 30 mV/s, with (orange curve) and without (blue curve) magnetic field.

5.5 References

1. Sharrock, M. P.; Bodnar, R. E., Magnetic materials for recording: An overview with special emphasis on particles (invited). *J. Appl. Phys.* **1985,** *57* (8), 3919.

2. Jung, J. H., Functionalized magnetic nanoparticles as chemosensors and adsorbents for toxic metal ions in environmental and biological fields. *Chem. Soc. Rev.* **2011,** *40* (9), 4464.

3. Schladt, T. D.; Schneider, K.; Schild, H.; Tremel, W., Synthesis and bio-functionalization of magnetic nanoparticles for medical diagnosis and treatment. *Dalton Transactions* **2011,** *40* (24), 6315-6343.

4. Yiu, H. H. P., Engineering the multifunctional surface on magnetic nanoparticles for targeted biomedical applications: a chemical approach. *Nanomedicine* **2011,** *6* (8), 1429-1446.

5. Mingwu, S.; Hongdong, C.; Xifu, W.; Xueyan, C.; Kangan, L.; Su He, W.; Rui, G.; Linfeng, Z.; Guixiang, Z.; Xiangyang, S., Facile one-pot preparation, surface functionalization, and toxicity assay of APTS-coated iron oxide nanoparticles. *Nanotechnology* **2012,** *23* (10), 105601.

6. Joris, F.; Manshian, B. B.; Peynshaert, K.; De Smedt, S. C.; Braeckmans, K.; Soenen, S. J., Assessing nanoparticle toxicity in cell-based assays: influence of cell culture parameters and optimized models for bridging the in vitro-in vivo gap. *Chem. Soc. Rev.* **2013,** *42* (21), 8339-8359.

7. Hayashi, K.; Ono, K.; Suzuki, H.; Sawada, M.; Moriya, M.; Sakamoto, W.; Yogo, T., One-Pot Biofunctionalization of Magnetic Nanoparticles via Thiol−Ene Click Reaction for Magnetic Hyperthermia and Magnetic Resonance Imaging. *Chem. Mater.* **2010,** *22* (12), 3768-3772.

8. Zhang, C.; Wängler, B.; Morgenstern, B.; Zentgraf, H.; Eisenhut, M.; Untenecker, H.; Krüger, R.; Huss, R.; Seliger, C.; Semmler, W.; Kiessling, F., Silica- and Alkoxysilane-Coated Ultrasmall Superparamagnetic Iron Oxide Particles: A Promising Tool To Label Cells for Magnetic Resonance Imaging. *Langmuir* **2006,** *23* (3), 1427-1434.

9. Xu, C.; Xu, K.; Gu, H.; Zheng, R.; Liu, H.; Zhang, X.; Guo, Z.; Xu, B., Dopamine as A Robust Anchor to Immobilize Functional Molecules on the Iron Oxide Shell of Magnetic Nanoparticles. *J. Am. Chem. Soc.* **2004,** *126* (32), 9938-9939.

10. Xie, J.; Chen, K.; Lee, H.-Y.; Xu, C.; Hsu, A. R.; Peng, S.; Chen, X.; Sun, S., Ultrasmall c(RGDyK)-Coated Fe3O4 Nanoparticles and Their Specific Targeting to Integrin αvβ3-Rich Tumor Cells. *J. Am. Chem. Soc.* **2008,** *130* (24), 7542-7543.

11. del Campo, A.; Sen, T.; Lellouche, J.-P.; Bruce, I. J., Multifunctional magnetite and silica–magnetite nanoparticles: Synthesis, surface activation and applications in life sciences. *J. Magn. Magn. Mater.* **2005,** *293* (1), 33-40.

12. Cornell, R. M.; Schwertmann, U., *The iron oxides: structure, properties, reactions, occurrences and uses*. John Wiley & Sons: 2003.

13. Sun, Y.-P., *Supercritical Fluid Technology in Materials Science and Engineering: Syntheses: Properties, and Applications*. CRC Press: 2002.

14. Teja, A. S.; Koh, P.-Y., Synthesis, properties, and applications of magnetic iron oxide nanoparticles. *Prog. Cryst. Growth Charact. Mater.* **2009,** *55* (1–2), 22-45.

15. Vargas, A.; Shnitko, I.; Teleki, A.; Weyeneth, S.; Pratsinis, S. E.; Baiker, A., Structural dependence of the efficiency of functionalization of silica-coated FeOx magnetic nanoparticles studied by ATR-IR. *Appl. Surf. Sci.* **2011,** *257* (7), 2861-2869.

16. Mikhaylova, M.; Kim, D. K.; Berry, C. C.; Zagorodni, A.; Toprak, M.; Curtis, A. S. G.; Muhammed, M., BSA Immobilization on Amine-Functionalized Superparamagnetic Iron Oxide Nanoparticles. *Chem. Mater.* **2004,** *16* (12), 2344-2354.

17. Yamaura, M.; Camilo, R. L.; Sampaio, L. C.; Macêdo, M. A.; Nakamura, M.; Toma, H. E., Preparation and characterization of (3-aminopropyl)triethoxysilane-coated magnetite nanoparticles. *J. Magn. Magn. Mater.* **2004,** *279* (2–3), 210-217.

18. Zhang, Z. J.; Chen, X. Y.; Wang, B. N.; Shi, C. W., Hydrothermal synthesis and self-assembly of magnetite (Fe3O4) nanoparticles with the magnetic and electrochemical properties. *J. Cryst. Growth* **2008,** *310* (24), 5453-5457.

19. Zhu, M.; Wang, Y.; Meng, D.; Qin, X.; Diao, G., Hydrothermal Synthesis of Hematite Nanoparticles and Their Electrochemical Properties. *The Journal of Physical Chemistry C* **2012,** *116* (30), 16276-16285.

20. Cabrera, L.; Gutierrez, S.; Menendez, N.; Morales, M. P.; Herrasti, P., Magnetite nanoparticles: Electrochemical synthesis and characterization. *Electrochim. Acta* **2008,** *53* (8), 3436-3441.

21. Fajaroh, F.; Setyawan, H.; Widiyastuti, W.; Winardi, S., Synthesis of magnetite nanoparticles by surfactant-free electrochemical method in an aqueous system. *Adv. Powder Technol.* **2012,** *23* (3), 328-333.

22. Zhen, G.; Muir, B. W.; Moffat, B. A.; Harbour, P.; Murray, K. S.; Moubaraki, B.; Suzuki, K.; Madsen, I.; Agron-Olshina, N.; Waddington, L.; Mulvaney, P.; Hartley, P. G., Comparative Study of the Magnetic Behavior of Spherical and Cubic Superparamagnetic Iron Oxide Nanoparticles. *The Journal of Physical Chemistry C* **2010,** *115* (2), 327-334.

23. Sun, S.; Zeng, H., Size-Controlled Synthesis of Magnetite Nanoparticles. *J. Am. Chem. Soc.* **2002,** *124* (28), 8204-8205.

24. Sun, S.; Zeng, H.; Robinson, D. B.; Raoux, S.; Rice, P. M.; Wang, S. X.; Li, G., Monodisperse MFe2O4 (M = Fe, Co, Mn) Nanoparticles. *J. Am. Chem. Soc.* **2003,** *126* (1), 273-279.

25. Barrera, C.; Herrera, A. P.; Rinaldi, C., Colloidal dispersions of monodisperse magnetite nanoparticles modified with poly(ethylene glycol). *J. Colloid Interface Sci.* **2009,** *329* (1), 107-113.

26. Bruce, I. J.; Sen, T., Surface Modification of Magnetic Nanoparticles with Alkoxysilanes and Their Application in Magnetic Bioseparations. *Langmuir* **2005,** *21* (15), 7029-7035.

27. Čampelj, S.; Makovec, D.; Drofenik, M., Functionalization of magnetic nanoparticles with 3-aminopropyl silane. *J. Magn. Magn. Mater.* **2009,** *321* (10), 1346-1350.

28. De Palma, R.; Peeters, S.; Van Bael, M. J.; Van den Rul, H.; Bonroy, K.; Laureyn, W.; Mullens, J.; Borghs, G.; Maes, G., Silane Ligand Exchange to Make Hydrophobic Superparamagnetic Nanoparticles Water-Dispersible. *Chem. Mater.* **2007,** *19* (7), 1821-1831.

29. Haensch, C.; Hoeppener, S.; Schubert, U. S., Chemical modification of self-assembled silane based monolayers by surface reactions. *Chem. Soc. Rev.* **2010,** *39* (6), 2323-2334.

30. Harris, L. A.; Goff, J. D.; Carmichael, A. Y.; Riffle, J. S.; Harburn, J. J.; St. Pierre, T. G.; Saunders, M., Magnetite Nanoparticle Dispersions Stabilized with Triblock Copolymers. *Chem. Mater.* **2003,** *15* (6), 1367-1377.

31. White, M. A.; Johnson, J. A.; Koberstein, J. T.; Turro, N. J., Toward the Syntheses of Universal Ligands for Metal Oxide Surfaces: Controlling Surface Functionality through Click Chemistry. *J. Am. Chem. Soc.* **2006,** *128* (35), 11356-11357.

32. Peng, R.; Zhang, W.; Ran, Q.; Liang, C.; Jing, L.; Ye, S.; Xian, Y., Magnetically Switchable Bioelectrocatalytic System Based on Ferrocene Grafted Iron Oxide Nanoparticles. *Langmuir* **2011,** *27* (6), 2910-2916.

33. Neouze, M.-A.; Schubert, U., Surface Modification and Functionalization of Metal and Metal Oxide Nanoparticles by Organic Ligands. *Monatshefte für Chemie / Chemical Monthly* **2008,** *139* (3), 183-195.

34. Beasley, C. A.; Murray, R. W., Voltammetry and Redox Charge Storage Capacity of Ferrocene-Functionalized Silica Nanoparticles. *Langmuir* **2009,** *25* (17), 10370-10375.

35. Roberts, J. J. P.; Vuong, K. T.; Murray, R. W., Synthesis and Electrochemistry of 6 nm Ferrocenated Indium–Tin Oxide Nanoparticles. *Langmuir* **2012,** *29* (1), 474-479.

36. Hayashi, K.; Moriya, M.; Sakamoto, W.; Yogo, T., Chemoselective Synthesis of Folic Acid−Functionalized Magnetite Nanoparticles via Click Chemistry for Magnetic Hyperthermia. *Chem. Mater.* **2009,** *21* (7), 1318-1325.

37. Polito, L.; Monti, D.; Caneva, E.; Delnevo, E.; Russo, G.; Prosperi, D., One-step bioengineering of magnetic nanoparticles via a surface diazo transfer/azide-alkyne click reaction sequence. *Chemical communications (Cambridge, England)* **2008,** (5), 621-623.

38. White, A. F.; Peterson, M. L.; Hochella Jr, M. F., Electrochemistry and dissolution kinetics of magnetite and ilmenite. *Geochim. Cosmochim. Acta* **1994,** *58* (8), 1859-1875.

39. Kijima, N.; Yoshinaga, M.; Awaka, J.; Akimoto, J., Microwave synthesis, characterization, and electrochemical properties of α-Fe2O3 nanoparticles. *Solid State Ionics* **2011,** *192* (1), 293-297.

40. J, M. K.; Frank, M., Direct electrochemistry of nanoparticulate Fe2O3 in aqueous solution and adsorbed onto tin-doped indium oxide. *Pure Appl. Chem.* **2001,** *73* (12), 1885-1894.

41. Campelj, S.; Makovec, D.; Drofenik, M., Preparation and properties of water-based magnetic fluids. *J. Phys.: Condens. Matter* **2008,** *20* (20), 204101.

42. Faulkner, A. J. B. a. L. R., *Electrochemical Methods: Fundamentals and Applications*. 2nd ed.; John Wiley & Sons, Inc.: Phoenix, Az, 2001.